LOCALIZED OPTICAL AND ELECTRICAL PROPERTIES OF III-V NITRIDE NANOSTRUCTURES

By
SANTANU KUMAR PARIDA

Enrolment No: PHYS 02 2014 04 006

Indira Gandhi Centre for Atomic Research, Kalpakkam

A thesis submitted to the

Board of Studies in Physical Sciences

In partial fulfillment of requirements
for the Degree of

DOCTOR OF PHILOSOPHY
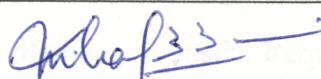
of

HOMI BHABHA NATIONAL INSTITUTE

May, 2019

Homi Bhabha National Institute
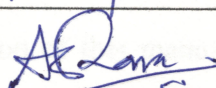
Recommendations of the Viva Voce Committee

As members of the Viva Voce Committee, we certify that we have read the dissertation prepared by **Santanu Kumar Parida** entitled **"Localized Optical and Electrical Properties Of III-V Nitride Nanostructures"** and recommend that it may be accepted as fulfilling the thesis requirement for the award of Degree of Doctor of Philosophy.

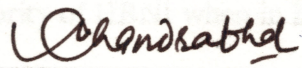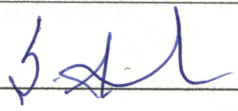|			
Chairman - Dr. M. Kamruddin			14/10/19
Guide - Dr. Sandip Kumar Dhara			14/10/2019
Examiner - Dr. Chandrabhas Narayana			14/10/2019
Member 1- Dr. T. R. Ravindran			14/10/2019
Member 2- Dr. S. Amirthapandian			14/10/19
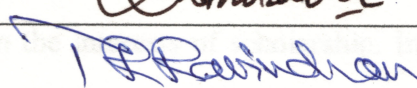
Final approval and acceptance of this thesis is contingent upon the candidate's submission of the final copies of the thesis to HBNI.

I hereby certify that I have read this thesis prepared under my direction and recommend that it may be accepted as fulfilling the thesis requirement.

Date: 14/10/2019

Place: Kalpakkam

Dr. Sandip Kumar Dhara

(Guide)

STATEMENT BY AUTHOR

This dissertation has been submitted in partial fulfillment of requirements for an advanced degree at Homi Bhabha National Institute (HBNI) and is deposited in the Library to be made available to borrowers under rules of the HBNI.

Brief quotations from this dissertation are allowable without special permission, provided that accurate acknowledgement of source is made. Requests for permission for extended quotation from or reproduction of this manuscript in whole or in part may be granted by the Competent Authority of HBNI when in his or her judgment the proposed use of the material is in the interests of scholarship. In all other instances, however, permission must be obtained from the author.

Santanu Kumar Parida
Santanu Kumar Parida

DECLARATION

I hereby declare that the investigation presented in the thesis has been carried out by me. The work is original and has not been submitted earlier as a whole or in part for a degree / diploma at this or any other Institution / University.

Santanu Kumar Parida

Santanu Kumar Parida

List of Publications arising from the thesis

Journal

1. Determining the polarity of droplet epitaxy grown AlGaN nanorods by piezoresponse force microscopy. **S. Parida**, G. Mangamma, C. Singha, A. Bhattacharyya, S. Dhara; *Nano-Structures & Nano-Objects*, **2019**, *20*, 100398.

2. Native defect assisted enhanced response to CH_4 near room temperature by $Al_{0.07}Ga_{0.93}N$ nanowires. **S. Parida**, A. Das, A. K. prasad, J. Ghatak S. Dhara; *Phys. Chem. Chem. Phys.*, **2018**, *20*, 18391.

3. Optical properties of AlGaN nanowires synthesized via ion beam techniques. **S. Parida**, P. Magudapathy, A. K. Sivadasan, R. Pandian, S. Dhara; *J. Appl. Phys.* **2017**, *121*, 205901.

4. Spectroscopic investigation of native defect induced electron-phonon coupling in GaN nanowires. **S. Parida**, A. Patsha, S. Bera, S. Dhara; *J. Phys. D: Appl. Phys.* **2017,** *50*, 275103.

Communicated / Under preparation

1. Role of surface density of states in understanding size dependent surface band bending in GaN nanowires. **S. Parida**, A. R. Sahoo, K. K. Madapu, S. Mathi Jaya, S. Dhara (*Communicated*).

2. Nanoscopic and spectroscopic study of single GaN nanowire in the sub-diffraction limit. **S. Parida**, A. Patsha, K. K. Madapu, S. Dhara (*Communicated*).

Conference Proceedings

1. Size dependent surface band bending in GaN nanowires. **S. Parida**, K. K. Madapu, S. Dhara; Bulletin of the American Physical Society **2019**.

2. Effect of Ar$^+$ implantation on the optical properties of Al/GaN nanowires. **S. Parida,** P. Magudapathy, A. K. Sivadasan, A. Patsha, S. Dhara; AIP Conference Proceedings **2017**.

Conference Presentation

1. Size dependent surface band bending in GaN nanowires. **S. Parida**, K. K. Madapu, S. Dhara; American Physical Society, March Meeting (APS-2019), Boston, USA (*Contributary talk*).

2. Surface band bending in GaN Nanowire using Kelvin probe force microscopy. **S. Parida**, K. K. Madapu, S. Dhara; Intl. Conf. on Microscope and XXXIX Annual Meeting of Electron Microscope Society of India (EMSI-2018) (*Contributary talk*).

3. Near room temperature methane sensing by ion beam synthesized Al$_{0.07}$Ga$_{0.93}$N nanowires. **S. Parida**, A. Das, A. K. Prasad, S. Dhara; Research Scholar Meet on Material Science and Engineering of Nuclear Materials (RSM-MSENM-2018).

4. Imaging the polarity of AlGaN nanostructure by piezoresponse force microscopy. **S. Parida**, G. Mangamma, A. Bhattacharyya, S. Dhara; International Conference on Nanoscience and Technology (ICONSAT-2018).

5. Effect of Ar$^+$ implantation on the optical properties of Al/GaN nanowires. **S. Parida**, P. Magudapathy, A. K. Sivadasan, A. Patsha, S. Dhara; 61st DAE Solid State Physics Symposium (DAE SSPS-2016).

6. Electron-phonon coupling and related optical properties of GaN nanowires with different III/V ratios. **S. Parida**, A. Patsha, S. Dhara; Emerging Trends in Advance Functional Material (ETAFM-2016).

Other Journal Publications (Not Included in the Thesis)

1. Size-dependent surface potential of Si-doped InN nanorods and the role of inhomogeneous free-electron distribution. K. K. Madapu, **S. Parida**, K. Jeganathan, M. Baral, S. Dhara; *J. Appl. Phys.*, **2019**, *125* 164308.

2. Spectroscopically forbidden infra-red emission in Au-vertical graphene hybrid nanostructures. A. K. Sivadasan, **S. Parida**, S. Ghosh, R. Pandian, S. Dhara; *Nanotechnology*, **2017**, *28*, 465703.

3. Charge transport studies on Si nanopillars for photodetectors fabricated using vapor phase metal-assisted chemical etching. P. Karadan, S. Parida, A. Kumar, A. Anappara, S. Dhara, H. Barshilia; *Appl. Phys. A*, **2017**, *123*, 681.

Santanu Kumar Parida

Dedicated to

My Parents

Acknowledgments

First of all, I would like to express my sincere gratitude to my research supervisor Prof. Sandip Kumar Dhara for his continuous support, motivation and encouragement in my Ph.D. work. Besides my advisor, my sincere thanks to the doctoral committee chairman Dr. M. Kamruddin, and members Dr. T. R. Ravindran and Dr. S. Amrithapandian for their constructive comments and suggestions. I convey my gratitude to Dr. G. Amarendra, Director, MSG and Dr. Arun Kumar Bhaduri, Director, IGCAR for the research facilities.

I convey my deep gratitude to my research collaborators Dr. G. Mangamma, Mr. P. Magudapathy, Dr. Ramanathaswamy Pandian, Dr. Arindam Das, Dr. Arun K. Prasad, Dr. Santanu Bera, Dr. S. Mathi Jaya, and Mr. Aloka R. Sahoo of IGCAR, Dr. Anirban Bhattacharyya and Mr. C. Singha of the University of Calcutta, and Dr. J. Ghatak of JNCASR for their help in many stages of the research.

I want to thank the reviewers of my thesis and manuscripts for their valuable comments and suggestions which helped in the improvement of the research articles. I deeply express my heart full thanks to my seniors Dr. Avinash Patsha, Dr. A. K. Sivadasan, Dr. Kishore K. Mudupu, for helping in the experimental works and constructive comments. I would also like to thank my friends Ms. Raktima Basu, Mr. Binaya Kumar Sahu, Mr. Gopinath Sahoo, Ms. Reshma P.R., and Mr. C. Abinash Bhuyan for their help at the laboratory and useful discussions.

It is my pleasure to remember my Parents and family members as well as my teachers and friends for their constant encouragements and supports.

CONTENTS

SUMMARY

The present Thesis work is focused on the synthesis of III-V nitride (GaN and AlGaN) nanowires (NWs) with the prime objective of exploring their localized optical and electrical properties at the nanoscale. In the course of the work, we have explored the following areas of research and the key findings are listed.

Charge carrier concentration is highly influenced in the presence of native defects in GaN. Thus, understanding the interactions of charge carriers with lattice vibrations is critical for manipulating the optical and electrical properties of atmospheric pressure chemical vapor deposited GaN NWs. Therefore, we aimed at shedding light on the various electron-phonon coupling characteristics in GaN NWs having different native defect density. The detailed analyses were performed by the help of Raman and photoluminescence (PL) spectroscopic studies.

We have also synthesized AlGaN NW by ion beam techniques for the first time. The synthesis was carried out by two processes, namely, i) Ion beam mixing (IBM) ii) Post irradiation diffusion (PID). The variation of Al incorporation percentage with Ar^+ fluence and annealing temperature was established from Raman spectroscopic analysis.

In the subsequent work, the gas sensing behavior of the IBM grown AlGaN NWs was studied since III-nitride based gas sensor functional at low operating temperature with high sensitivity was in demand owing to their high chemical and thermal stability. Methane (CH_4) gas sensing was realized, for the first time, using $Al_{0.07}Ga_{0.93}N$ NWs with an improved response at a low operating temperature of 50 °C. The sensing mechanism was explained from the extensive study of defects using PL spectroscopy.

Moreover, we have also explored the physical properties at the nanoscale. Piezoresponse force microscopy (PFM) was employed to study the piezoresponse and for determining the piezoelectric coefficient of $Al_{0.97}Ga_{0.03}N$ nanorods (NRs). The variation in piezoresponse was explained based on the spontaneous polarization in a unit cell of the hexagonal crystal owing to different crystal orientations. We could identify *c*-plane oriented NRs from *m*-plane one with the observation strong piezoresponse in the former.

In order to study the localized electrical properties, the contact potential difference (CPD) between the tip and individual GaN NWs was measured using Kelvin probe force microscopy (KPFM). The corresponding surface band bending (SBB) was calculated from the measured CPD value and was found to decrease with increase in the NW diameter. The observed size dependence of SBB in NW was correlated to the decreasing number of surface density of states with increasing NW diameter which was further corroborated with the *ab initio* density functional theory calculation.

As part of the optical study at the nanoscale, the nanoscopic and spectroscopic imaging were carried out with the help of surface probe microscopy (SPM) based techniques coupled with light. The nanoscopic imaging with a spatial resolution of 10s of nm was achieved with the help of a near-field scanning optical microscopy (NSOM) probe of aperture size 150 nm and excitation wavelength of 532 nm. Similarly, in the nano-spectroscopic study using the tip enhanced Raman spectroscopy (TERS) imaging of a single GaN NW of ~225 nm was demonstrated, for the first time, which was far below the diffraction limit of ~ 750 nm using an excitation source of 514.5 nm with an objective lens of 0.42 numerical aperture.

LIST OF FIGURES

LIST OF TABLES

CHAPTER 1

INTRODUCTION

1.1 III-V Nitrides

III-V nitrides and their ternary alloys find tremendous attention in the scientific community as well as the optoelectronic industry because of their applications in light emitting diodes (LEDs) and laser diodes.[1-3] The variation in the atomic percentage of the constituent elements in the ternary alloy allows one to tune the band gap of III-V nitrides from ~0.7 to 6.2 eV.[4-6] The foremost attractive material properties of these materials are high carrier mobility, elevated melting temperature, high thermal conductivity, enormous physical hardness, and extremely large hetero-junction offsets. Due to the extensive reduction of extended defects in 1D nanostructures, unidirectional carrier flow, and easy handling, III-V nitride based nanowires (NWs) have emerged as ideal candidates for building blocks of nanoscale electronic and optoelectronic devices.[7-9] However, there are some issues in the alloy formation of III-V nitrides and many of these physical properties are yet to be understood especially in case of the nanostructures. Therefore, the study of the optical and electrical properties of III-nitrides nanostructures are described in detail in this Thesis. Before going to address some of the issues and studying the properties at the nanoscale, the following sections briefly introduce crystal the structure and different physical properties of III-V nitrides.

1.2 Crystal Structure

III-V Nitrides exists in the three crystal structures of wurtzite, zinc blend and rock salt. Among them wurtzite structure is stable under ambient conditions.[10] The metastable zinc blende

structure has been stabilized by epitaxial growth of thin films on (011) crystal planes of cubic substrates,[10] such as Si, SiC, MgO, and GaAs. The cubic phase of GaN was also reported to be stable in the post-annealed samples of self-ion (Ga$^+$) beam implanted GaN NW where ion beam induced defect played a role for stabilizing the metastable phase.[11] However, the growth of rock salt structure is possible only under elevated pressure (~52.2 GPa) and, therefore, is a laboratory form of exercise.[10] The wurtzite structures involve two interpenetrated hexagonal unit cells (Fig. 1.1a) and thus two lattice constants, a and c.
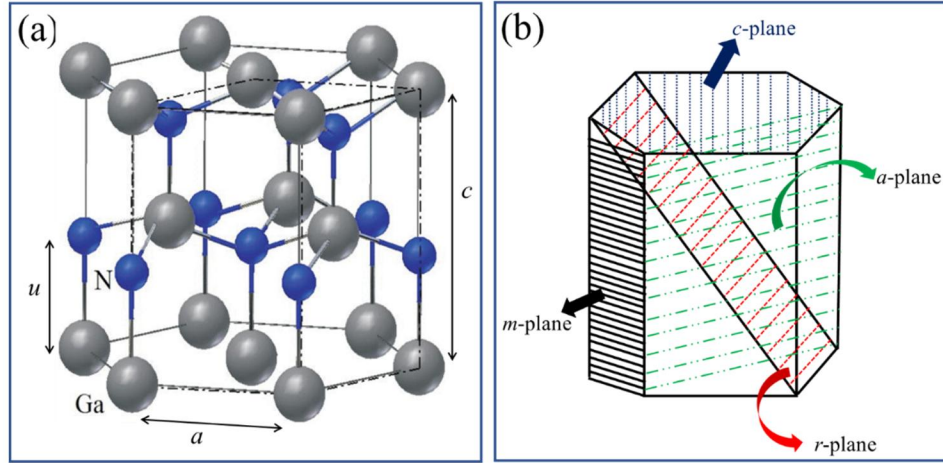
Figure 1.1. (a) Schematic representation of wurtzite crystal structure and (b) different crystallographic planes.

Each unit cell contains six atoms of each type and is displaced along the c-axis by $5c/8$. The space group symmetry of wurtzite structure is P6$_3$mc. The important crystal planes of the wurtzite structure are depicted in figure 1.1b. Along the c-axis, wurtzite structure possesses non-center of symmetry. Therefore, the basal plane or c-plane is terminated with the atoms of either group III element (0001) or N (000-1). As a result, the wurtzite crystal structure of nitrides provides the spontaneous polarization along the c-axis and hence the c-plane is called as polar plane. Among the other planes, a-plane (11-20) and m-plane (10-10) are the non-polar, whereas r-plane (1−102) is semi-polar in nature.[10]

1.3 Physical Properties of III-V Nitrides

The group III-nitride semiconductors are of direct band gap and intrinsically *n*-type in nature because of the non-stoichiometry created by the N vacancies (V_N).[12, 13] High chemical and thermal stability allow them to be an excellent candidate for device operation at high temperatures and in adverse environmental condition. The major physical properties of GaN, InN, and AlN are compared with each other and are tabulated (Table 1.1).[10,14,15] Moreover, the vibrational and luminescence properties are described in detail, as the major optical characterizations in the Thesis are performed using Raman and photoluminescence (PL) spectroscopy techniques.

Table 1.1. Comparison of basic physical properties of III-V nitrides.

Property		GaN	InN	AlN
Lattice parameter,	a (Å)	3.189	3.539	3.110
	c (Å)	5.186	5.708	4.980
Band gap (eV) (at 0K)		3.51	0.7	6.25
Exciton Bohr radius (nm)		2.4	8	1.4
Exciton binding energy (meV)		23	9	57
Electron mobility ($cm^2 \cdot V^{-1} \cdot s^{-1}$) (at 300K)		1400	4000	---
Breakdown field ($MV \cdot cm^{-1}$) (at 300K)		3	2	1.8
Thermal conductivity ($W \cdot cm^{-1} \cdot K^{-1}$) (at 300K)		2.3	0.8	2.9
Piezoelectric coefficient d_{33} (pm/V)		3.1	7.6	5.1
Relative dielectric constant		8.9	15	8.5
Refractive index		2.7 at 353 nm	2.56 at 1µm	2.58 at 220 nm

1.3.1 Vibrational properties

In the wurtzite structure, group theory predicts eight sets of normal phonon modes at the zone center. The irreducible representation of these normal modes is given as $\Gamma = 2A_1 + 2E_1 + 2E_2 + 2B_1$.[16,17] One set of A_1 and E_1 modes are acoustic phonon modes and while remaining, $A_1 + E_1 + 2E_2 + 2B_1$, are optical phonon modes. Among these, both the A_1 and E_1 phonon modes are IR and Raman active. Whereas, the E_2 phonon modes are exclusively Raman active. However, the B_1 phonon mode is neither Raman nor IR active and is named as a forbidden mode.
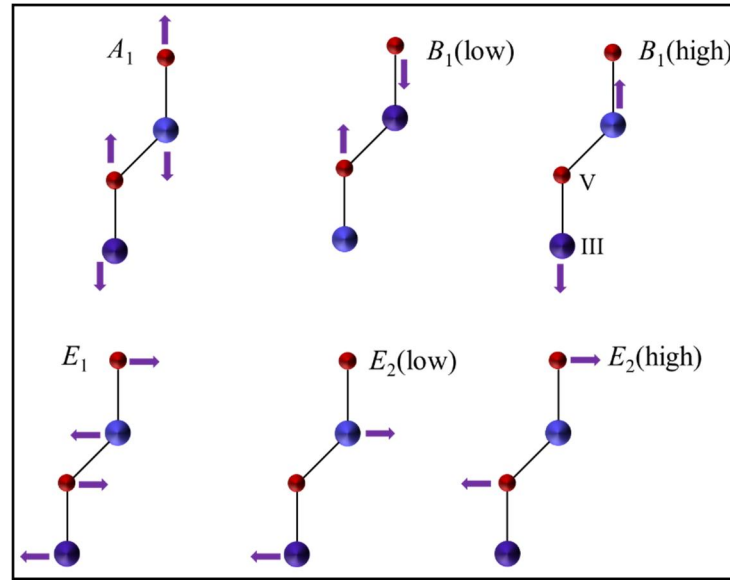
Figure 1.2. Schematic representation of optical phonon modes in the wurtzite structure.

The A_1 and E_1 phonon modes are polar, and these vibrations polarize the unit cell leading to further split into the longitudinal optical (A_1(LO) and E_1(LO)) and transverse optical (A_1(TO) and E_1(TO)) modes. Consequently, wurtzite crystal possesses six Raman active phonon modes namely, $2A_1$, $2E_1$, and $2E_2$ at the zone center. The basic vibrational motions of atoms corresponding to different phonon modes are schematically illustrated in figure 1.2. The typical energy values of different optical phonon modes are listed below (Table 1.2).[16-20]

Table 1.2. Wurtzite phase III-V nitride optical phonon modes and their frequencies.

Phonon modes	Frequency (cm^{-1})		
	GaN	InN	AlN
E_2(low)	144	87	248
A_1(TO)	533	447	612
E_1(TO)	560	472	672
E_2(high)	569	488	660
A_1(LO)	734	588	894
E_1(LO)	742	593	917
B_1(Low)	334	225	547
B_1(high)	690	579	719

1.3.2 Luminescence properties and role of impurities in III-V nitrides

Luminescence is the process of light emission from materials after the excitation with some source of energy.[21,22] In III-V nitrides, the emission wavelength can be tuned in a wide range of the electromagnetic spectrum by proper alloy formation. However, the presence of defects influences the optical emission in these III-nitride based devices. Generally, there are two types of optical transitions which give rise to emission, namely, (i) intrinsic, (ii) extrinsic. Intrinsic optical transitions include free-excitons (FX) and their phonon replicas. Whereas, extrinsic transitions are constituted of impurity-bound excitons (excitons bound to a neutral donor; D^{0}X and to a neutral acceptor; A^{0}X), free-to-bound (conduction band to acceptor; e-A) and bound-to-bound (donor-acceptor-pair; DAP) transitions.[23] Moreover, impurities create electronic states within the band gap of the semiconductor and affect the emission spectra. In III-V nitrides, commonly observed luminescence bands are ultraviolet (UVL), blue (BL), green

(GL), yellow (YL) and red luminescence (RL), depending on the impurity type (donor or acceptor) and positions of the electronic state (shallow or deep). A schematic band diagram describing the major optical transitions in GaN is shown in figure 1.3.[23, 24]
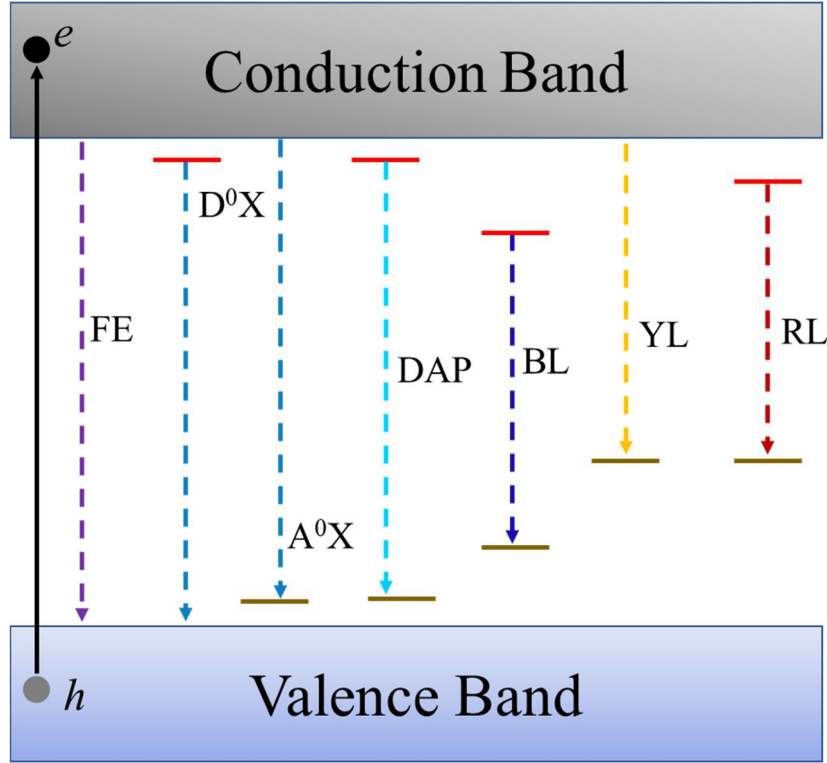
Figure 1.3. Schematic representation of optical transitions in GaN.

1.4 Native Defects and Their Effect on Electron-Phonon Coupling in GaN

The performance of highly efficient nanoscale electronic and optoelectronic semiconductor devices depends on the dopants and defects, which control the free carrier density, as well as the carrier mobility. There are commonly known native point defects, such as N vacancy (V_N), O dopant in lattice place of N (O_N) and Ga vacancy (V_{Ga}) in unintentionally doped GaN. Among them, O_N is an unavoidable impurity in group III-nitride. The concentration of unintentional O impurity in GaN films is found to be of the order of 10^{17}-$10^{21}\cdot$cm^{-3}, which results in the net carrier concentration of 10^{16}-10^{20} cm^{-3}.[25,26] The incorporation of native defects

in GaN NWs can be due to the growth process leading to efficiency in the supply of precursor materials (Ga/N ratio), and preferred crystallographic growth orientation. Several studies were carried out to realize the effect of the supply of the Ga/N ratio and O impurity incorporation on the stoichiometry, size, surface morphology, growth rate, optical and electrical properties of GaN NWs.[27-30] Therefore, it is important to measure the carrier concentration induced by the incorporation of native defects and their effect on electrical and optical properties of the GaN NW. Unlike in the case of thin films, it is difficult to perform secondary ion mass spectroscopy, Hall probe on single NWs to quantify the carrier concentration and their mobility, because of the geometrical constraint. Therefore, it is necessary to explore and understand the utilization of alternative spectroscopic techniques for the study of native defects in NWs.

The optical and electrical properties of semiconducting materials are well known to be influenced by the basic interactions of exciton or charge carriers with lattice vibrations (phonons). The reduction in carrier mobility, broadened near edge optical transitions, and cooling of hot carriers are among the direct consequences of electron-phonon interactions.[31] Different kinds of interactions are possible with different lattice vibrations in GaN. The nonpolar TO phonons, interact with electrons by means of deformation-potential (DP), while the polar LO phonons interact with electrons by means of Coulomb interactions, known as the Fröhlich interaction (FI).[31,32] The electron-phonon interactions in GaN films are well studied by means of Raman and PL spectroscopy analysis. The plasmon coupled LO phonon modes are studied by analyzing the Raman spectra of GaN, revealing the strong electron-phonon coupling in the system with a different carrier density.[33-35] Most of the studies have been carried out by varying the extrinsic doping concentration in GaN. Nevertheless, there are hardly any

reports on the effect of native defects (V_N, O_N, V_{Ga}) in unintentionally doped GaN and resultant free carriers on electron-phonon coupling in GaN NWs using optical spectroscopy. The same is also missing for the study of the strength of the interaction potential in analyzing the carrier concentration and mobility. Thus, an understanding of electron-phonon interactions is critical for manipulating the optical and electrical properties of GaN NWs. Therefore, the present Thesis aims to shed light on the various electron-phonon coupling characteristics in unintentionally doped GaN NWs, having different native defect densities. The defect induced free charge carriers are manipulated by growing GaN NWs using an atmospheric pressure chemical vapor deposition (APCVD) technique under variable precursor flow rates. Detailed Raman and PL spectroscopic studies are performed to explore the electron-phonon interactions induced by native defects and is presented in Chapter 2.

1.5 Issues in Growth of AlGaN in CVD and Synthesis by Ion Beam Techniques

AlGaN based LEDs serve as tunable sources in the region of ultra-violet (UV) to deep UV (3.4-6.2 eV) by varying the Al percentage.[3,5,36,37] Generally, the internal quantum efficiency (IQE) of the optoelectronic devices is very low due to high leakage current in InGaN/GaN based blue LEDs. The IQE can be increased to a significant extent by using AlGaN as an electron blocking layer in the multi quantum well (MQW) LEDs.[38] Moreover, AlGaN plays a vital role in hetero-structure high electron mobility transistors (HEMT) by employing a two-dimensional electron gas induced at the hetero-interface as a highly conducting channel.[39] However, the synthesis of AlGaN with the desired percentage of Al, is difficult due to the following reasons. During the growth process, highly reactive atomic N reacts instantly with Al adatoms and limits the further diffusion of the adatoms to form AlGaN with a higher atomic percentage of Al.[10] Furthermore, incorporation of oxygen is promoted due to the high chemical

affinity of Al towards oxygen, and hence, it suppresses the growth of AlGaN.[40] Specifically, in the commercially viable technique of chemical vapour deposition (CVD), it is very difficult to achieve high quality AlGaN with a higher percentage (>10%) of Al because of the miscibility limit and the requirement of very high temperature (>1100 °C) for the formation of Ga and Al eutectic alloys in the catalyst assisted vapor-liquid-solid (VLS) process.[41] In this context, we would like to mention that, achieving Al content >3 at. % in the AlGaN nanostructure using thermodynamic processes is very difficult pertaining to the high value of defect formation energy in nanostructures while incorporating Al into the lattice of GaN nanostructures.[41,42] The above mentioned difficulties can be tackled up to a certain extent by adopting the well-known ion beam mixing (IBM) techniques, useful for alloy formation above the miscibility limit, and can be employed to thermodynamically immiscible systems, as well.[43] In comparison to the direct implantation, IBM results in a very uniform composition throughout the depth of penetration of the irradiation ion. Defect creation and simultaneous diffusion of elemental species are anticipated to form alloys with a higher incorporation percentage than the conventional process. Furthermore, IBM is a versatile technique for multilayer formation in metallic and semiconductor systems. In the present Thesis, the IBM technique is used for the synthesis of AlGaN NWs. A new approach was also adopted for the synthesis of AlGaN by the process of post-irradiation diffusion (PID),[44] with a motivation for the enhancement of the Al diffusion into GaN due to the production of native defects by the irradiation of high energy ions. The detailed study of optical properties using Raman and PL spectroscopy of the samples grown in the ion beam techniques are described in Chapter 3.

1.6 Gas Sensing Properties: Utilization of Native Defects

Along with controlling the optoelectronic properties, native defects also influence gas sensing by controlling the conduction process, especially for nanostructures.[45] Moreover, III-V nitrides are chemically and thermally stable and also biocompatible.[10] Therefore, it is a better choice for the gas sensing device in regard to their stability unlike that of the metal oxides.[46,47] It is well known that metal oxides show variation in stoichiometry with time in ambient conditions and hence lose the stability resulting in the fluctuation of response. However, the sensitivity of the device, which is reported to be very high for metal oxide nanostructure,[46-48] can be compromised at the cost of the stability of the nitride-based semiconductor for long term applications. There are only a few reports of gas sensors based on the III-nitride semiconductors. The gas sensing behavior of the III-V nitrides is demonstrated mostly through functionalization or decorating by metal nanoparticles like Pd and Pt, where the sensitivity can be tuned by controlling the catalyst particle size and distribution.[49-52] The possibility of degradation of the device performance due to the poor thermal stability of Pd like metal nanoparticles is reported.[53] Moreover, gas sensing behavior is also realized with the formation of heterostructures using the nitride semiconductors. Generally, two types of heterostructures are proven to be a good candidate for gas sensor application, (i) the metal-semiconductor junction (Schottky diode),[54,55] and (ii) semiconductor-semiconductor junction for the formation of HEMT structure,[56,57] especially in the III-V nitrides. In the case of Schottky diode, the sensing behavior is explained with the help of variation in the barrier height by exposing the analyte gas. On the other hand, the formation of two-dimensional (2D) electron gas at the interface of $Al_xGa_{1-x}N$ based heterostructures provides high mobility leading to the fast response and recovery of the device in the HEMT like structure. Nevertheless, the making

of heterostructures and the sharp interface between the two semiconductors are challenging and need sophisticated epitaxial growth techniques. The above-discussed techniques and structures are mostly utilized for the sensing of H_2 gas. Leaving metal oxide-based sensors,[46,47,58] there are very few reports on the sensing of methane (CH_4) using the nitride-based semiconductor.[45] CH_4 is the second highest contributor to global warming with a global warming potential of 23 as compared to CO_2 of value 1. The detection of CH_4 at temperatures lower than 350 °C is difficult owing to its thermodynamic stability as compared to other hydrocarbons.[59] Thus, much attention is paid to the research community for the sensing of CH_4 gas at lower temperatures, particularly near room temperature. The low temperature sensing of CH_4 is realized in the metal oxide based semiconductor nanostructure because a sufficient amount of activation energy can be provided by the nanostructures for triggering the chemisorption in the gas sensing process.[47,58] Whereas, there is hardly any report for the low-temperature CH_4 sensing behavior using III-V nitrides. Further, obtaining high sensitivity and low operating temperature for the nitride-based gas sensors are challenging and need to be explored further. In the present study, the CH_4 gas sensing behavior of the $Al_xGa_{1-x}N$ NWs is demonstrated with a primary focus of investigating the underlying mechanism.

1.7 Localized Studies on III-V Nitrides

Materials at nanoscale change their properties from their bulk counterpart. Therefore, the localized measurement of the physical properties is very important for the utilization of III-V nitride nanostructures as electronic and optoelectronic devices. In the following part of the Chapter, the localized measurement of III-V nitride nanostructures using the scanning probe force microscopy (SPM) based techniques are discussed. The electrical properties are explored using piezoresponse force microscopy (PFM) and Kelvin probe force microscopy (KPFM).

The optical properties are studied by coupling of light with the SPM in the techniques of tip enhanced Raman spectroscopy (TERS) and near field scanning optical microscopy (NSOM).

1.7.1 Piezoelectricity and piezoresponse force microscopic studies on AlGaN nanorods

Piezoelectricity is the phenomenon of production of electrical potential in a crystal with the application of an external mechanical stress. Along with the semiconducting behavior, III-nitrides exhibit piezoelectric character because of the non-centrosymmetry in the wurtzite crystal structure.[10] Therefore, the electronic behavior of the materials can be tuned with the application of mechanical strain of the materials having both semiconducting and piezoelectric character. Moreover, the III-V nitrides show the difference in the piezoelectric coefficient in accordance with the ionicity of the group III element resulting in the difference in internal parameter (u) and c/a ratio in the hexagonal crystal structure.[10,60] For example, AlN shows the d_{33} (major component of piezoelectric coefficient) value of 5.1 pm/V whereas; GaN is reported to have a d_{33} value of 3.1 pm/V.[60-62] Therefore, the value of the piezoelectric coefficient can also be tuned with the proper alloy formation in III-V nitrides.[42] As a result, the coupling of piezoelectric character with the optoelectronic properties in III-V nitride semiconductors provides a unique degree of freedom in designing high-performance nanoelectronics devices with mechanical tunability. Therefore, the measurement of the piezoelectric properties with the high spatial resolution is of importance for the performance of nitride-based nanostructured piezotronics devices. Piezoresponse force microscopy, the versatile and efficient member of SPM family, is the best choice for the identification and imaging of ferroelectric domains in the nanostructure with resolution down to tens of picometer. Hence, the piezoelectric coefficient can be calculated at the nanoscale. Moreover, the piezoelectric contribution from different crystallographic planes in nanostructure can be imaged because of the high-resolution

measurement with the simultaneous measurement of topography. The piezoresponse signal constitutes both magnitude and phase part. The magnitude of piezoresponse gives the strength of the piezoelectricity. Whereas, the phase image provides information about the direction of polarization in each crystallographic plane of the crystal.[63-65]

In the present Thesis, the PFM imaging of the plasma-assisted molecular beam epitaxy (PA-MBE) $Al_{0.97}Ga_{0.03}N$ NRs oriented in different crystallographic directions is demonstrated in Chapter 4.

1.7.2 Surface band bending in GaN nanowires: Insight from Kelvin probe force microscopy

The electronic property of semiconductor materials is governed by dopant and defect atoms incorporation.[10,66] Moreover, the surface states also play a crucial role in governing the electronic property.[66,67] On a semiconductor surface, surface states exist because of the termination of lattice periodicity. The unpaired electrons in the dangling bonds of surface atoms interact with each other forming an electronic state with a very narrow energy band at the semiconductor band gap. In the case of the n-type semiconductor, bulk Fermi level E_F (bulk) is closer to the conduction band, which is higher than the surface Fermi level (E_F (surf)) under disequilibrium.[67,68] In thermal equilibrium, there will be a transfer of charge carriers in between these states. In the n-type semiconductor, the electrons are transferred from the bulk to the surface. As a result, E_F (bulk) drops and E_F (surf) rises until an equilibrium is achieved. At equilibrium, the energy bands bend upward as one move toward the surface.[68] Similarly, in the case of the p-type semiconductor E_F (bulk) is closer to the valance band and lies below the surface Fermi level (E_F (surf)) under disequilibrium. Holes are transferred from the bulk to the

surface, and E_F (bulk) gets lifted, and E_F (surf) falls until equilibrium is achieved. At equilibrium, the energy bands bend downward as one move toward the surface. In the nanostructures, the surface states affect the band structure of the semiconductor drastically because of the presence of a higher number of atoms at the surface as compared to the bulk.[69] Therefore, the electronic properties of the nanostructure semiconductors are influenced by the surface density of states. The complete understanding and characterization of the surface states are important in the optoelectronic devices. Unfortunately, the direct experimental admittance to characterize these surface states is very difficult. Moreover, the surface states are prone to change with the surrounding condition and instrumental artifacts.[69,70]

In recent years, however, scanning tunneling microscopy (STM) has proven to be an ideal tool for the investigation of individual bulk defects and dopant atoms in semiconductors.[71,72] Nevertheless, STM measurements are limited to conducting,[73] and heavily doped semiconductors and suffer from tip-induced band bending phenomena.[74] The SPM based KPFM technique has already been demonstrated as a powerful tool for measuring electrostatic forces and electric potential distribution with nanometer resolution.[75] Due to its promise of high spatial resolution surface potential measurements, the KPFM has found miscellaneous applications in just a few years. Therefore, the present study intends to investigate the effect of surface states on the band bending of the unintentionally doped n-GaN NW using Kelvin probe force microscopy with high spatial resolution and is detailed in Chapter 4.

1.7.3 Optical microscopic and spectroscopic study at nanoscale: Overcoming the diffraction limit

It is well known that spatial resolution of optical microscopy and spectroscopy is limited by Abbe's diffraction limit of light. At best one can achieve a spatial resolution of $0.61\lambda/(NA)$; λ being the incident wavelength of photon and NA the numerical aperture of the objective lens which are used for focusing of the probing light. For microscope objectives with a large NA (~1.0), a spatial resolution of $\sim\lambda/2$ can be achieved experimentally, e.g., a spatial resolution of ~250 nm can be achieved with the visible light of 500 nm. For practical application, such a spatial resolution is adequate to investigate some physical properties of materials in bulk or thin films. However, in the case of objects at the nanoscale, the optical spatial resolution limit shields the precise characterization of objects smaller than the diffraction limit. Nevertheless, by coupling the plasmonic character of metal and high spatial resolution of AFM, one can overcome the diffraction limit of light. In the present Thesis work, the nanoscopic and nano-spectroscopic imaging are carried out with the help of NSOM and TERS, respectively. The results are detailed in Chapter 5.

The SPM based plasmonic assisted NSOM is a unique tool to understand the light-matter interaction in the sub-diffraction limit. [87-90] The light passing through the metal coated tip of the NSOM probe overcomes the diffraction limit. In the near-field regime, evanescent field components emanate from the NSOM probe with higher momenta *i.e.*, lower wavelength. Therefore, it facilitates the nanoscopic imaging of objects with nanometric spatial resolution. Similarly, in the context of spectroscopic study at the nanoscale, TERS is proven to be a significant characterization technique. TERS employs a noble metal tip scanning in the near-field of the probed object, leading to a high spatial resolution. Moreover, the Raman scattering

cross-section is very low, which further prevents to get enough scattering photon intensity from nanostructure. With the implementation of the TERS tip, the electric field in the sub-nanometer regime get enhanced and therefore can probe the properties of the nanostructure. Moreover, one can get the topographic as well as spectroscopic information simultaneously by performing the TERS mapping in the near-field. In the present Thesis, the spectroscopic imaging of single GaN NWs is achieved for the first time.

1.8 Objective and Overview of the Thesis

The prime objective of the Thesis is to study the localized optical and electrical properties of III-V nitride nanostructures since the materials at nanoscale change their properties from their bulk counterpart. Presence of native defects in GaN NW and their effect on electron-phonon couplings are investigated. Subsequently, the difficulties in synthesizing AlGaN NWs in CVD and exploring the alternative way of synthesis in ion beam techniques are also addressed. Moreover, the sensing behavior is explored, since the native defects influence the electronic property by controlling the charge transfer process. In addition to that, the localized properties are studied with the help of SPM based techniques along with the coupling of light with the SPM.

Chapter 1 introduces the III-V nitrides and their basic physical properties and their importance. The detail description on the effect of native defects on the optical and electrical properties are also discussed. Moreover, the difficulties of synthesis of AlGaN NWs by CVD technique and methodologies of overcoming with the utilization of ion beam synthesis process are presented. In the later part of the Chapter, the importance and utilization of SPM based techniques as localized probe for studying the properties at the nanoscale are described.

Chapter 2 presents the growth of GaN NWs with different Ga/N ratio by varying the precursor gas flow rate. The effect of the native defect on electron-phonon coupling in these NWs is discussed in detail. Moreover, the effect of DP and FI on the vibrational modes are studied with the help of Raman spectroscopic analysis. The effect of native defects on the luminescence property and their correlation with the electron-phonon coupling are also discussed.

Chapter 3 describes the synthesis of AlGaN NWs with ion beam techniques. IBM and PID processes are carried out for synthesizing the AlGaN NWs from APCVD grown GaN NW. The Al incorporation percentage, as estimated from vibrational analysis using Raman spectroscopy, and its dependence with the variation of ion irradiation fluence and annealing temperature are also discussed. Subsequently, the CH_4 gas sensing behavior of the ion beam synthesized AlGaN NWs is studied close to room temperature, for the first time, as a comparison with the as-grown GaN. The effect of native defects on the sensing behavior and the underlying mechanism is described with the help of detailed PL analysis.

In Chapter 4, the localized electrical properties are studied with the help of SPM based techniques of PFM and KPFM. Spatial distribution of piezoresponse of $Al_{0.97}Ga_{0.03}N$ nanorods is mapped using PFM. Point spectroscopy is carried out for determining the polarity of the planes and d_{33} value of $Al_{0.97}Ga_{0.03}N$ nanorod is calculated with the help of PFM analysis for the first time. The surface band bending (SBB) in GaN is studied with the help of KPFM measurements. The role of surface states in determining the variation of SBB with the NW diameter is expanded, for the first time, with the help of *ab initio* density functional theory (DFT) calculation.

In Chapter 5, the optical properties are studied at the nanoscale by coupling the light with SPM. The NSOM and TERS studies are utilized for the nanoscopic and nano-spectroscopic imaging in the diffraction limit of light, respectively. A spatial resolution of 10s of nm is achieved with the help of NSOM probe of aperture size 150 nm and excitation wavelength of 532 nm. For the first time, TERS imaging of a single GaN NW of ~225 nm is demonstrated which is far below the diffraction limit using an excitation source of 514.5 nm with an objective lens of 0.42 NA. A Nominally increased enhancement factor for the E_1(TO) modes was attributed to the fact that the direction of the phonon mode vibration was oriented along the tip induced electric field distribution, as supported by finite-difference time-domain (FDTD) calculation.

Chapter 6 summarizes major findings of the Thesis and scope for the future work in this direction.

1.9 References

[1]   S. Nakamura, T. Mukai, and M. Senoh, Applied Physics Letters **64,** 1687 (1994).

[2]   F. Qian, Y. Li, S. Gradečak, H.-G. Park, Y. Dong, Y. Ding, Z. L. Wang, and C. M. Lieber, Nature Materials **7,** 701 (2008).

[3]   A. Khan, K. Balakrishnan, and T. Katona, Nature Photonics **2,** 77 (2008).

[4]   J. Wu and W. Walukiewicz, Superlattices and Microstructures **34,** 63 (2003).

[5]   T. Inazu, S. Fukahori, C. Pernot, M. H. Kim, T. Fujita, Y. Nagasawa, A. Hirano, M. Ippommatsu, M. Iwaya, and T. Takeuchi, Japanese Journal of Applied Physics **50,** 122101 (2011).

[6]   T. Kuykendall, P. Ulrich, S. Aloni, and P. Yang, Nature Materials **6,** 951 (2007).

[7]   P. J. Pauzauskie and P. Yang, Materials Today **9,** 36 (2006).

[8]   S. Zhao, H. P. Nguyen, M. G. Kibria, and Z. Mi, Progress in Quantum Electronics **44,** 14 (2015).

9 A. Patsha, S. Dhara, S. Chattopadhyay, K.-H. Chen, and L.-C. Chen, Journal of Materials NanoScience **5,** 1 (2018).

10 H. Morkoç, *Handbook of Nitride Semiconductors and Devices, Materials Properties, Physics and Growth*, Vol. 1 (John Wiley & Sons, 2009).

11 S. Dhara, A. Datta, C. Wu, Z. Lan, K. Chen, Y. Wang, C. Hsu, C. Shen, L. Chen, and C. C. Chen, Applied Physics Letters **84,** 5473 (2004).

12 M. Ganchenkova and R. M. Nieminen, Physical Review Letters **96,** 196402 (2006).

13 J. Neugebauer and C. G. Van de Walle, Physical Review B **50,** 8067 (1994).

14 H. Morkoç, *Handbook of Nitride Semiconductors and Devices Vol. 3 GaN-based Optical and Electronic Devices* (Wiley Online Library, 2008).

15 B. Gil, *Physics of Wurtzite Nitrides and Oxides: Passport to Devices* (Springer Series in Materials Science, 2014)

16 H. Harima, Journal of Physics: Condensed Matter **14,** R967 (2002).

17 V. Y. Davydov, Y. E. Kitaev, I. Goncharuk, A. Smirnov, J. Graul, O. Semchinova, D. Uffmann, M. Smirnov, A. Mirgorodsky, and R. Evarestov, Physical Review B **58,** 12899 (1998).

18 H. Harima, Journal of Physics: Condensed Matter **16,** S5653 (2004).

19 V. Y. Davydov, I. Goncharuk, A. Smirnov, A. Nikolaev, W. Lundin, A. Usikov, A. Klochikhin, J. Aderhold, J. Graul, and O. Semchinova, Physical Review B **65,** 125203 (2002).

20 V. Y. Davydov, V. Emtsev, I. Goncharuk, A. Smirnov, V. Petrikov, V. Mamutin, V. Vekshin, S. Ivanov, M. Smirnov, and T. Inushima, Applied Physics Letters **75,** 3297 (1999).

21 M. Fox, *Optical Properties of Solids* (Oxford University Press, 1970).

22 P. Y. Yu and M. Cardona, *Fundamentals of Semiconductors: Physics and Materials Properties* (Springer, 2010).

23 M. A. Reshchikov and H. Morkoc, Journal of Applied Physics **97,** 061301 (2005).

24 M. Julkarnain, N. Kamata, T. Fukuda, and Y. Arakawa, Optical Materials **60**, 481 (2016)

25 S. Sintonen, P. Kivisaari, S. Pimputkar, S. Suihkonen, T. Schulz, J. S. Speck, and S. Nakamura, Journal of Crystal Growth **456,** 43 (2016).

26 G. A. Slack, L. J. Schowalter, D. Morelli, and J. A. Freitas Jr, Journal of Crystal Growth **246,** 287 (2002).

27 P. Sahoo, S. Dhara, S. Amirthapandian, M. Kamruddin, S. Dash, B. Panigrahi, and A. Tyagi, Crystal Growth & Design **12,** 2375 (2012).

28 S. Yadav, C. Rodríguez-Fernández, M. M. de Lima Jr, A. Cantarero, and S. Dhar, Journal of Applied Physics **118,** 225703 (2015).

29 Q. Gao, V. G. Dubrovskii, P. Caroff, J. Wong-Leung, L. Li, Y. Guo, L. Fu, H. H. Tan, and C. Jagadish, Nano Letters **16,** 4361 (2016).

30 A. Patsha, S. Amirthapandian, R. Pandian, and S. Dhara, Journal of Materials Chemistry C **1,** 8086 (2013).

31 X. Zhang, T. Taliercio, S. Kolliakos, and P. Lefebvre, Journal of Physics: Condensed Matter **13,** 7053 (2001).

32 S. Dhara, S. Chandra, G. Mangamma, S. Kalavathi, P. Shankar, K. G. M. Nair, A. K. Tyagi, C. W. Hsu, C. C. Kuo, L. C. Chen, K. H. Chen, and K. K. Sriram, Applied Physics Letters **90,** 213104 (2007).

33 T. Kozawa, T. Kachi, H. Kano, Y. Taga, M. Hashimoto, N. Koide, and K. Manabe, Journal of Applied Physics **75,** 1098 (1994).

34 K. Jeganathan, R. Debnath, R. Meijers, T. Stoica, R. Calarco, D. Grützmacher, and H. Lüth, Journal of Applied Physics **105,** 123707 (2009).

35 L. H. Robins, E. Horneber, N. A. Sanford, K. A. Bertness, M. Brubaker, and J. Schlager, Journal of Applied Physics **120,** 124313 (2016).

36 P. Sun, X. Bao, S. Liu, C. Ye, Z. Yuan, Y. Wu, S. Li, and J. Kang, Superlattices and Microstructures **85,** 59 (2015).

37 Y. Sato, N. Takahashi, and S. Sato, Japanese Journal of Applied Physics **37,** L129 (1998).

38 Z. G. Ju, W. Liu, Z.-H. Zhang, S. T. Tan, Y. Ji, Z. Kyaw, X. L. Zhang, S. P. Lu, Y. P. Zhang, and B. B. Zhu, ACS Photonics **1,** 377 (2014).

39 Y. Li, J. Xiang, F. Qian, S. Gradecak, Y. Wu, H. Yan, D. A. Blom, and C. M. Lieber, Nano Letters **6,** 1468 (2006).

40 S. Jain, M. Willander, J. Narayan, and R. V. Overstraeten, Journal of Applied Physics **87,** 965 (2000).

41 A. K. Sivadasan, A. Patsha, S. Polaki, S. Amirthapandian, S. Dhara, A. Bhattacharya, B. Panigrahi, and A. Tyagi, Crystal Growth & Design **15,** 1311 (2015).

42 A. K. Sivadasan, G. Mangamma, S. Bera, M. Kamruddin, and S. Dhara, Journal of Applied Physics **119,** 174304 (2016).

43 S. Dhara, Critical Reviews in Solid State and Materials Sciences **32,** 1 (2007).

44 S. Parida, P. Magudapathy, A. Sivadasan, R. Pandian, and S. Dhara, Journal of Applied Physics **121,** 205901 (2017).

45 A. Patsha, P. Sahoo, S. Amirthapandian, A. K. Prasad, A. Das, A. Tyagi, M. A. Cotta, and S. Dhara, The Journal of Physical Chemistry C **119,** 21251 (2015).

46 V. Bonu, A. Das, A. K. Prasad, N. G. Krishna, S. Dhara, and A. Tyagi, Applied Physics Letters **105,** 243102 (2014).

47 A. Prasad, S. Amirthapandian, S. Dhara, S. Dash, N. Murali, and A. Tyagi, Sensors and Actuators B: Chemical **191,** 252 (2014).

48 V. L. Patil, S. A. Vanalakar, P. S. Patil, and J. H. Kim, Sensors and Actuators B: Chemical **239,** 1185 (2017).

49 P. Sahoo, S. Dhara, S. Dash, S. Amirthapandian, A. K. Prasad, and A. Tyagi, International Journal of Hydrogen Energy **38,** 3513 (2013).

50 A. K. Prasad, P. K. Sahoo, S. Dhara, S. Dash, and A. K. Tyagi, Materials Chemistry and Physics **211,** 355 (2018).

51 J. S. Wright, W. Lim, B. P. Gila, S. J. Pearton, J. L. Johnson, A. Ural, and F. Ren, Sensors and Actuators B: Chemical **140,** 196 (2009).

52 H.-I. Chen, Y.-C. Cheng, C.-H. Chang, W.-C. Chen, I.-P. Liu, K.-W. Lin, and W.-C. Liu, Sensors and Actuators B: Chemical **247,** 514 (2017).

53 J. Song, W. Lu, J. S. Flynn, and G. R. Brandes, Solid-State Electronics **49,** 1330 (2005).

54 F. Yam and Z. Hassan, Applied Surface Science **253,** 9525 (2007).

55 B. Kang, F. Ren, B. Gila, C. Abernathy, and S. Pearton, Applied Physics Letters **84,** 1123 (2004).

56 J. Schalwig, G. Müller, U. Karrer, M. Eickhoff, O. Ambacher, M. Stutzmann, L. Görgens, and G. Dollinger, Applied Physics Letters **80,** 1222 (2002).

57 J. Schalwig, G. Müller, M. Eickhoff, O. Ambacher, and M. Stutzmann, Sensors and Actuators B: Chemical **87,** 425 (2002).

58   A. Das, V. Bonu, A. K. Prasad, D. Panda, S. Dhara, and A. K. Tyagi, Journal of Materials Chemistry C **2,** 164 (2014).

59   K. Schierbaum, U. Weimar, and W. Göpel, Sensors and Actuators B: Chemical **7,** 709 (1992).

60   F. Bernardini and V. Fiorentini, Applied Physics Letters **80,** 4145 (2002).

61   C. Lueng, H. L. Chan, C. Surya, and C. Choy, Journal of Applied Physics **88,** 5360 (2000).

62   K. Tonisch, V. Cimalla, C. Foerster, H. Romanus, O. Ambacher, and D. Dontsov, Sensors and Actuators A: Physical **132,** 658 (2006).

63   E. Soergel, Journal of Physics D: Applied Physics **44,** 464003 (2011).

64   S. V. Kalinin and D. A. Bonnell, Physical Review B **65,** 125408 (2002).

65   H. D. Espinosa, R. A. Bernal, and M. Minary-Jolandan, Advanced Materials **24,** 4656 (2012).

66   C. Kittel, P. McEuen, and P. McEuen, *Introduction to Solid State physics*, Vol. 8 (Wiley New York, 1976).

67   S. M. Sze and K. K. Ng, *Physics of Semiconductor Devices* (John wiley & sons, 2006).

68   Z. Zhang and J. T. Yates Jr, Chemical Reviews **112,** 5520 (2012).

69   C. P. Poole Jr and F. J. Owens, *Introduction to Nanotechnology* (John Wiley & Sons, 2003).

70   W. Melitz, J. Shen, A. C. Kummel, and S. Lee, Surface Science Reports. **66,** 1 (2011).

71   Y. Rosenwaks, R. Shikler, T. Glatzel, and S. Sadewasser, Physical Review B **70,** 085320 (2004).

72   H. Ebert, Materials Today **6,** 36 (2003).

73   G. Binnig, H. Rohrer, C. Gerber, and E. Weibel, Physical Review Letters **49,** 57 (1982).

74   M. Weimer, J. Kramar, and J. D. Baldeschwieler, Physical Review B **39,** 5572 (1989).

75   W. Melitz, J. Shen, A. C. Kummel, and S. Lee, Surface Science Reports **66,** 1 (2011).

CHAPTER 2

GROWTH OF GaN NANOWIRES WITH DIFFERENT III/V RATIO AND STUDY OF ELECTRON-PHONON COUPLING

2.1 Introduction

Group III nitrides attract remarkable attention because of their tunable electronic and optical properties by appropriate alloy formation. Due to the extensive reduction of extended defects in 1D nanostructures, III-nitride based nanowires (NWs) have emerged as ideal candidates for building blocks of nanoscale electronic and optoelectronic devices such as LEDs, laser diodes, photodetectors ranging from infrared to ultraviolet regime.[1-3] The III-nitride NW heterojunctions also find application for high electron mobility transistor and high efficiency solar cells.[4,5] The performance of such highly efficient nanoscale electronic and optoelectronic semiconductor devices depends on the dopants and defects, which control the carrier density as well as carrier mobility. Among the commonly known native point defects such as N vacancy (V_N), O in the lattice site of N (O_N) and Ga vacancy (V_{Ga}) in unintentionally doped GaN, O_N is a ubiquitous inevitable impurity in group III nitride. In the literature, the concentration of unintentional O impurity in GaN films is reported to be order of 10^{17}-10^{21} cm^{-3}, which results in tuning the net carrier concentration of 10^{16}-10^{20} per cubic cm.[6,7] The free charge carriers can interact with the basic interactions of exciton or lattice vibrations, which in turn influence the optical and electrical properties in the semiconductor. The electron-phonon interactions in GaN films are well studied by varying the extrinsic doping concentration.[8] Different kinds of interactions are possible with different lattice vibrations in GaN. The nonpolar transverse optical (TO) phonons, interact with electrons by means of deformation-potential (DP), while the polar longitudinal optical (LO) phonons interact with electrons by

means of Coulomb interactions known as Fröhlich interaction (FI).[8,9] The plasmon coupled LO phonon modes are studied by analyzing Raman spectra of GaN, revealing the strong electron-phonon coupling in the system with different carrier density.[10-13] Nevertheless, there is hardly any study on the effect of native defects (V_N, O_N, V_{Ga}) in unintentionally doped GaN and resultant free carriers on electron-phonon coupling in GaN NWs using optical spectroscopy.

The present chapter is devoted to the growth of GaN NWs with different native defect density and study of the electron-phonon coupling in these NWs. GaN NWs were grown using atmospheric pressure chemical vapor deposition (APCVD) technique under variable precursor flow rates to manipulate the defect induced free charge carrier concentration. Detailed Raman and photoluminescence (PL) spectroscopic studies were performed to explore the electron-phonon interactions induced by native defects.

2.2 Atmospheric Pressure Chemical Vapor Deposition

CVD is the technique in which the deposition of solid materials occurs at high temperature by means of chemical reactions. Usually, the material synthesized via CVD technique is crystalline as the growth occurs in the thermodynamically equilibrium condition. The CVD method can be classified based on different parameters. The main parameters are pressure, wall and substrate temperature, nature of precursor, and gas flow state and mode of activation. CVD is a promising method for its cost-effectiveness and large-scale growth of NWs.[14,15] In the CVD technique, NW growth is normally performed by following the well-established vapour-liquid-solid (VLS) growth mechanism. We have chosen CVD process as commercially viable growth of GaN NWs where the large area of deposition can be facilitated.

The following are the major steps involved in the CVD process,[14]

✓ Convective and diffusive transport of reactant species to the reaction zone,

✓ Transport of the reactant products from the chemical to the substrate surface,

✓ Chemical reactions of these species at the substrate surface by means of adsorption, diffusion, and desorption processes leading to nucleation,

✓ Further rational attachment of reactant species leading to the growth of nuclei,

✓ Transport of volatile substances and the byproducts of reaction away from the reaction zone.

The experimental setup for CVD varies depending upon the requirements. If the chamber is maintained at atmospheric pressure during the deposition time, the method is called atmospheric pressure chemical vapor deposition (APCVD). The experimental setup used for the growth of GaN NWs in the VLS mechanism,[14,16] is shown in figure 2.1.
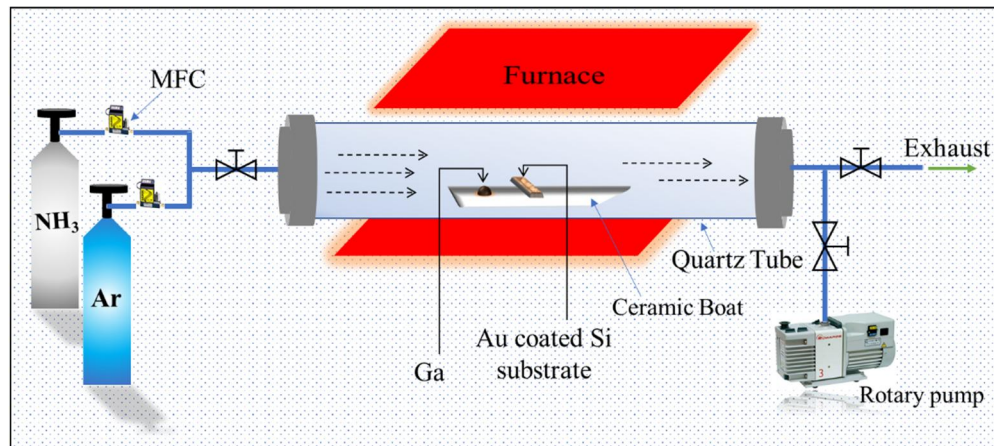
Figure 2.1. Schematic of APCVD system used for the growth of GaN NWs.

The major components of the APCVD system are listed below with the specific functionalities.

(i) Horizontal tube furnace: A horizontal tubular furnace was used as an energy source to carry out the chemical reaction. The important parameters of the furnace are listed below.

Maximum temperature: 1200 ℃

Temperature control: Proportional-integral-derivative (PID)

Temperature accuracy: ±1 ℃

Heating element: SiC

Thermocouple: S-type

(ii) Reaction chamber: The quartz tube of length ~110 cm and diameter of 2.5 cm was used as the reaction chamber. The solid precursors were kept inside the tube using the ceramic boat and the gaseous precursors could pass through the gas delivery system.

(iii) Vacuum system: The reaction chamber was connected to a mechanical rotary pump for the pre-evacuation. The chamber was capable to be evacuated up to a pressure of 1E-3 mbar. The chamber pressure was measured using the Pirani gauge and mechanical gauge for the low and high-pressure regimes, respectively.

(iv) Gas delivery and control system: The delivery system included the transport of precursor gas along with the carrier gas. In the present study, reactive NH_3 (99.999%) was used as precursor gas along with carrier gas Ar. The gas flow was controlled using the mass flow controller (MFC). Both the gases could flow through different MFC and mixed together before entering to the reaction chamber.

2.3 Vapor-Liquid-Solid Mechanism: Growth of Nanowires

In the VLS mechanism, the metal catalyst forms liquid alloy droplets at a high temperature by adsorbing vapor components. Due to the fluctuation of temperature or vapor pressure, the alloy is further supersaturated; *i.e.* it becomes a solution in which the actual concentration of the components is higher than the equilibrium concentration. It then drives the precipitation of the component at the liquid-solid interface to achieve minimum free energy of the alloy system. Accordingly, 1D crystal growth begins and it continues as long as the vapor components are supplied. As vapor (carrying solid components), liquid (catalyst alloy), and solid (precipitated one-dimensional structures) phases are involved in the growth process (schematic in Fig. 2.2), it is known as the VLS mechanism.
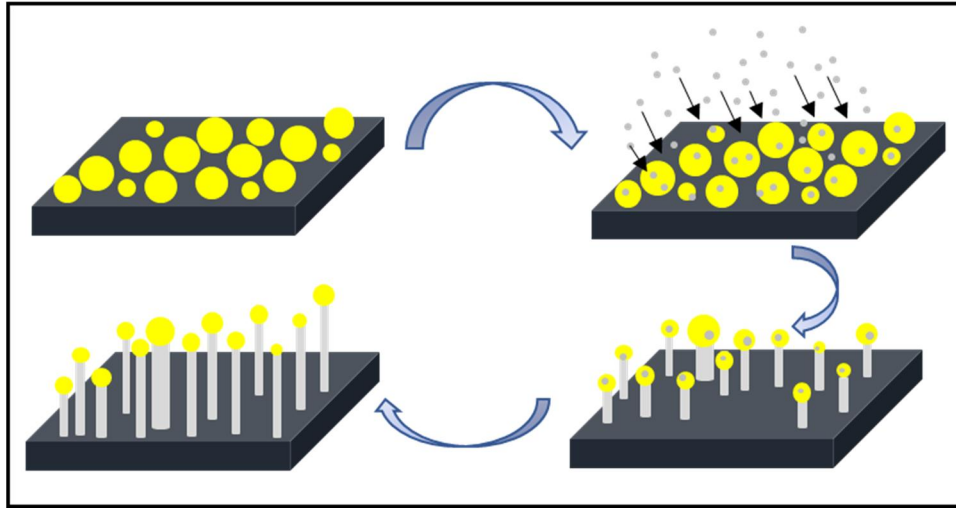
Figure 2.2. Schematic of different steps involved in the VLS mechanism.

2.4 Synthesis of GaN Nanowires

GaN NWs were synthesized by APCVD technique using VLS process. Au catalyst was deposited on Si substrates using thermal evaporation technique (12A4D, HINDHIVAC, India). These substrates were annealed for making the Au nanoparticles (NPs) at a temperature of 900 °C for 10 min. Ga metal (99.999%, Alfa Aesar) as precursor, NH_3 (5 N pure) as reactant

and Ar (5 N pure) as carrier gases were used for the growth process. The Si substrate with Au NPs was kept upstream of a Ga droplet (~200 mg) in a high pure alumina boat (99.95%), placed inside a quartz tube. The temperature of the quartz tube was raised to a growth temperature of 900 ºC with a ramp rate of 15 ºC per minute. Growth was carried out for 180 minutes with different flow rates of NH_3 and by keeping a constant amount of Ga (200 mg) in the reaction chamber. Sample S1 was grown under N rich condition by flowing 50 sccm of NH_3 without any carrier gas. On the other hand, samples S2 and S3 were grown under N reduced environment by NH_3 flow rate of 10 sccm and diluted with the carrier Ar gas of 10 and 20 sccm, respectively.

2.5 Morphological Analysis

The typical field emission scanning electron microscopy (FESEM) images of as-grown GaN NWs from sample S1-S3 are shown in figure 2.3a-c respectively. The Au NPs at the tip show that the NWs are grown in the VLS process. The FESEM micrograph of sample grown under N rich condition (S1) shows very rough and non-uniform surface morphology for the as-grown NWs having a size distribution of ~80-120 nm with a less growth rate of ~ 0.5 μm/hr (Fig. 2.3a). On the other hand, the NWs grown under N reduced conditions (S2 and S3) show a quite smooth and uniform surface morphology with a growth rate ~2 μm/hr and size distribution of ~60-120 nm (Fig. 2.3b) and ~60-150 nm (Fig. 2.3c) for S2 and S3, respectively. The reduction in the growth rate for sample S1 can be attributed to the self-nitridation of Ga source in case of N rich condition. In other words, the growth rate is impeded with the formation of a thin nitride layer on the top surface of the Ga source and the observation is consistent with the earlier report.[17]
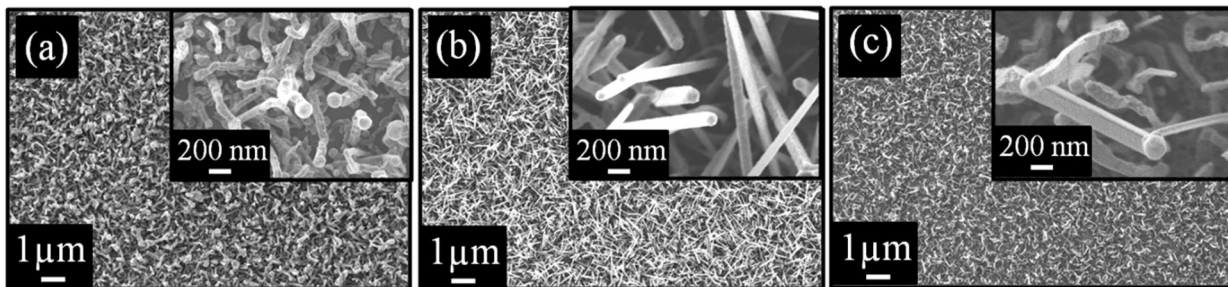
Figure 2.3. Typical FESEM images of GaN NWs of samples (a) S1 (b) S2, and (c) S3. Insets showing the high magnification images of as-grown NWs.

2.6 Compositional Analysis

The X-ray photo electron spectroscopy (XPS) study was carried out to estimate the Ga/N ratio in NWs for all the samples. Typical XPS spectra for the samples are shown in figure 2.4 for different elements. The peak centered at ~19.4 eV corresponds to the binding energy of the electron in 3*d* electronic state of Ga. Similarly, N 1*s* level is observed at ~397 eV from the de-convolution of a broad peak, which is considered as a combination of N 1*s* and Ga *LMM* Auger transitions. Along with the peaks corresponding to Ga and N, a peak at ~531 eV was also observed and was attributed to O 1*s*.[18,19] The presence of O peak in the XPS study shows that the unintentional incorporation of O in GaN may have occurred during the APCVD growth process, as the base vacuum of the chamber and purging of precursor gases are inadequate to reduce the presence of O. Other sources like substrate and quartz tube can also contribute to the O contamination. However, the relative variation of atomic percentages (at.%) of O from sample S1 to S3 represents its contribution from the GaN lattice. The at.% of Ga, N and O are calculated from the area under the curves and are tabulated in table 2.1.[20]

Table 2.1. Atomic percentage of the elements calculated from XPS spectra.

Sample	Ga (at. %)	N (at. %)	O (at. %)	Ga/N ratio
S1	29.9	41.8	28.3	0.715
S2	27.9	40.1	32.0	0.696
S3	26.7	39.9	33.4	0.670

XPS analysis shows a decrease in both Ga and N at.% and an increase in O at.% from sample S1 to S3. Surprisingly, less amount of Ga at.% was observed in the sample S3, which was grown under N reduced, (*i.e.* Ga rich) condition. However, the observed increase in O at.% from sample S1 to S3 could be due to the reduction in the N concentration during their growth.
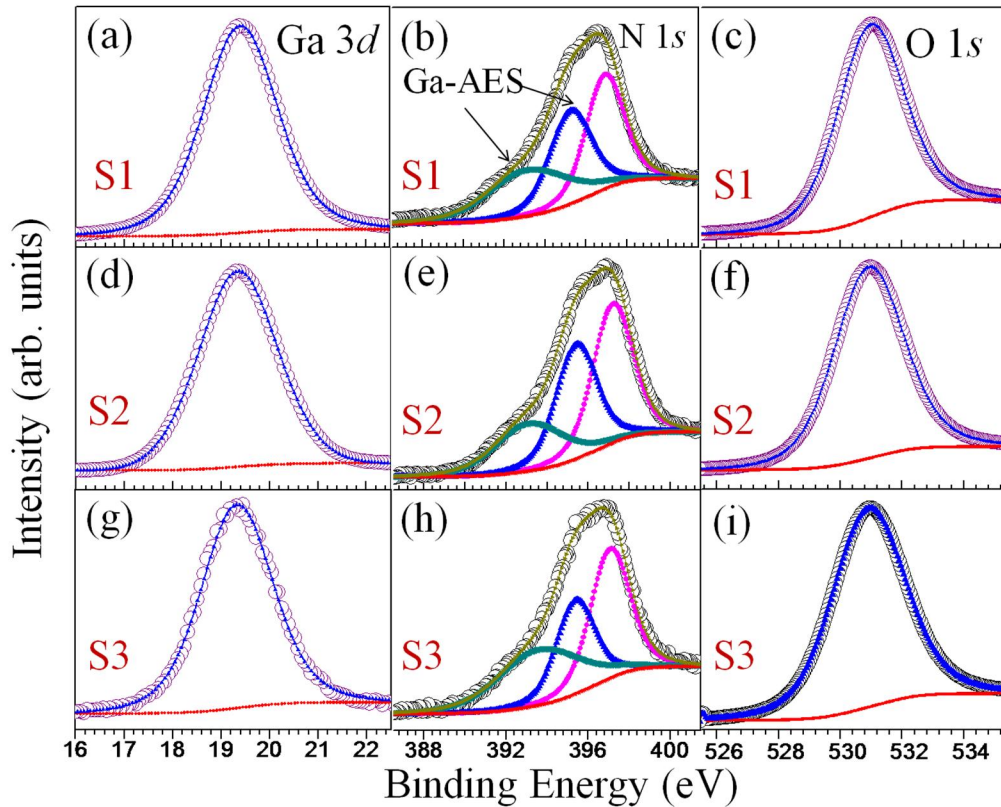
Figure 2.4. Typical XPS spectra of different elements and its characteristic electronic transitions for samples (a)-(c) S1, (d)-(f) S2 and (g)-(i) S3 deconvoluted with a Shirley type background (red line) correction.

Hence, it may be emphasized that since S3 is grown under less concentration of NH_3, the amount of O involved in the growth process is expected to be high by forming O_N point defects and $2O_N$ defect complex in GaN.[21] Furthermore, the excess O_N defects enhance the V_{Ga} density by forming V_{Ga}-$3O_N$ defect complex,[21] and hence a reduction in Ga at.% is observed in the XPS analysis. Moreover, we calculated Ga to N ratio (Ga/N) in all the samples and the ratio for sample S1 (~0.715) is found to be close to the stoichiometric value of unity.

2.7 Characteristics of Electron-Phonon Coupling in Raman Spectra

The typical Raman spectra are shown (Fig. 2.5) for the NW samples grown under different N concentration. In case of a wurtzite hexagonal structure, group theory predicts eight sets of phonon normal modes at the Γ-point, namely, $2A_1 + 2E_1 + 2B_1 + 2E_2$. Among them, one set of A_1 and E_1 symmetry modes are acoustic, while the remaining six modes ($A_1 + E_1 + 2B_1 + 2E_2$) are optical. Each one of A_1 and E_1 optical modes split into LO and TO modes due to their polar nature of vibration.[13,22]

The Raman spectra of NWs from all the samples were fitted with Lorentzian line shape and were analyzed for the corresponding phonon modes. As grown NWs of sample S1 (Fig. 2.5a) show the peaks centered at ~567, ~537, and 721 cm^{-1} corresponding to Raman active E_2(high) phonon mode, TO and LO phonon modes of A_1 symmetry (A_1(TO)) and A_1(LO)), respectively. The observation confirms the presence of wurtzite GaN phase of the grown NWs.[13,22] Along with the Raman active modes, two broad peaks centered at ~628 and ~680 cm^{-1} are assigned to the surface optical (SO) phonon modes of GaN corresponding to A_1 and E_1 symmetries, respectively.[23] An intense peak centered at ~521 cm^{-1} corresponds to the Si substrate on which GaN NWs are grown (Fig. 2.5a). The Raman spectra of GaN NWs of

sample S2 (Fig. 2.5b) also show similar characteristics as that of S1, along with a new peak centered at ~420 cm^{-1} which corresponds to the zone boundary (ZB) phonon mode of GaN arising due to the finite size of the crystal in the NW sample.[23] However, the A_1(LO) symmetry phonon mode is blue shifted by ~3 cm^{-1}. Whereas in case of sample S3 (Fig. 2.5c), along with an intense peak of E_2(high) phonon mode, a peak corresponding to the TO mode of E_1 symmetry (E_1(TO)) at ~551 cm^{-1} is also observed. Moreover, the A_1(LO) mode is further blue shifted by 6 cm^{-1} as compared to that for the sample S1.
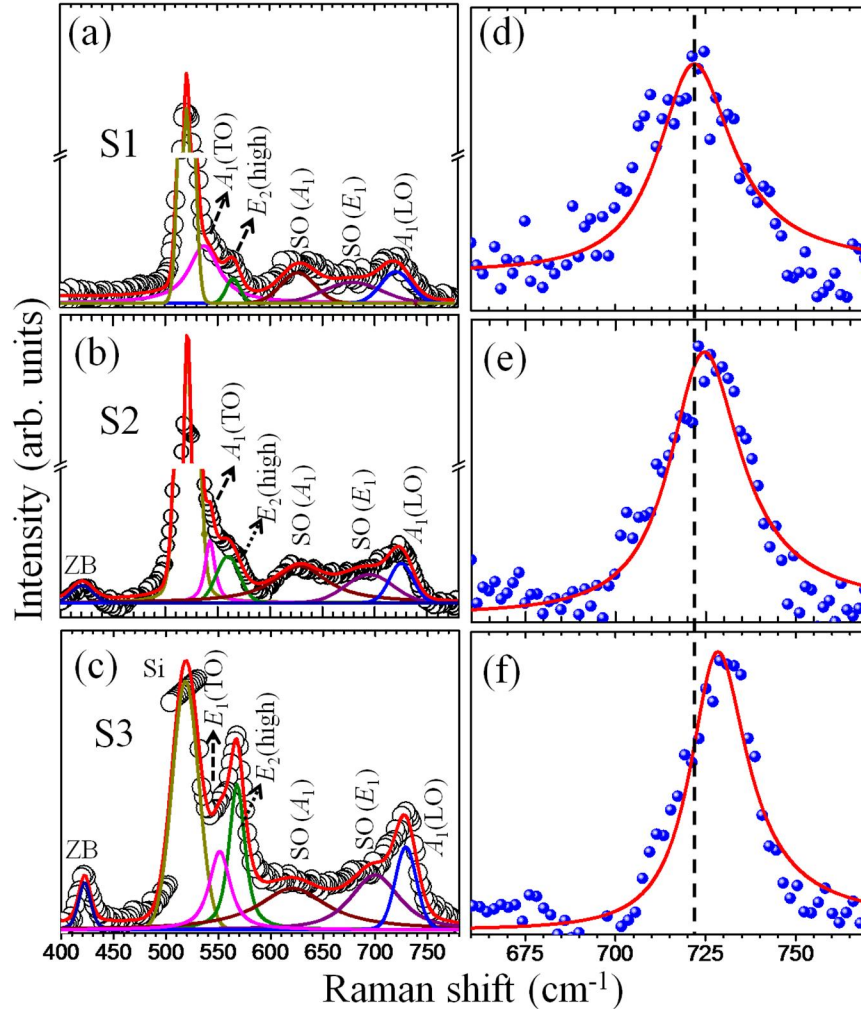
Figure 2.5. Typical Raman spectra of GaN NWs acquired using 514.5 nm excitation from samples (a) S1, (b) S2 and (c) S3 with Lorentzian line shape fitted. (d)-(f) Corresponding A_1(LO) mode fitted with line shape analysis. The vertical dashed line is a guide to eye for the observed blue shift of A_1(LO) mode.

2.8 Fröhlich Interaction and Deformation-Potential Involved Electron-Phonon Coupling

As discussed in Chapter 1, the electron-phonon coupling can occur either by FI and/or by DP interactions. The non-polar phonons, such as E_2, TO modes are mostly involved in interacting with DP, whereas polar LO phonons are involved in both FI and DP interactions.[8] In the ionic crystals like GaN, the FI is dominant depending on the excitation energy. The relative strength of both FI and DP interactions by different phonon modes can be revealed by considering the ratio of Raman intensities of corresponding phonon modes.[24] Since the matrix element $\langle k|H_{ep}|j\rangle$ of electron-phonon interaction (H_{ep}) in Raman intensity is different for different phonon modes, the ratio of Raman intensities of particular phonon modes is equivalent to the ratio of magnitudes of the corresponding matrix elements as given by equation (2.1), and hence the relative strength of the interactions.[24]

$$I_{E_2,TO}/I_{(LO)} \approx |\langle k|H_{ep}(E_{2,TO})|j\rangle|^2 \, / \, |\langle k|H_{ep}(LO)|j\rangle|^2 \approx |\langle k|\,DP|j\rangle|^2 \, / \, |\langle k|(DP+FI)|j\rangle|^2 \ldots\ldots\ldots(2.1)$$

Variations are often observed in relative Raman intensities of E_2(high), E_1(TO), A_1(TO) and A_1(LO) phonon modes in GaN, with respect to the crystal orientation, collection geometry for scattered photons, excitation energy, and presence of dopants.[10-13,25] In the present study, although the scattered photons from GaN NWs are collected in unpolarized condition and the NWs are aligned randomly on the substrate, the relative Raman intensities of E_2(high) and A_1(LO) phonon modes are found to vary among the three NWs samples (Figs. 2.5a-c). Such variations in the Raman intensity could be due to the relative strength of the electron-phonon interactions. In order to understand the strength of these interactions, the ratio of intensities of E_2(high) and LO phonon modes ($I_{E_2}/I_{A_1(LO)}$), and the ratio of intensities of TO and LO phonons (I_{TO}/I_{LO}) are estimated and compared among the three samples. The ratios

$(I_{E_2}/I_{A_1(\mathrm{LO})})$ for S1, S2, and S3 are found to be 0.3, 1.0, and 1.76, respectively. Whereas, the ratios $(I_{A_1(\mathrm{TO})}/I_{A_1(\mathrm{LO})})$ for S1 and S2 are 1.80 and 1.57, respectively. For the sample S3, the ratio $(I_{E_2}/I_{A_1(\mathrm{LO})})$ is estimated to be 0.94. The values suggest that DP interactions with E_2(high) phonons is stronger in case of sample S3 than that of the sample S1. While in case of non-polar TO phonons in III-nitrides,[8] the contribution of DP interaction is significantly reduced as compared to E_2(high) mode leading to an overall decrease in the ratio $I_{\mathrm{TO}}/I_{\mathrm{LO}}$. In this context, it may be noted that an approximately six-fold increase is observed for the ratio $I_{E_2}/I_{A_1(\mathrm{LO})}$ indicating a significant role of DP in sample S3.[20]
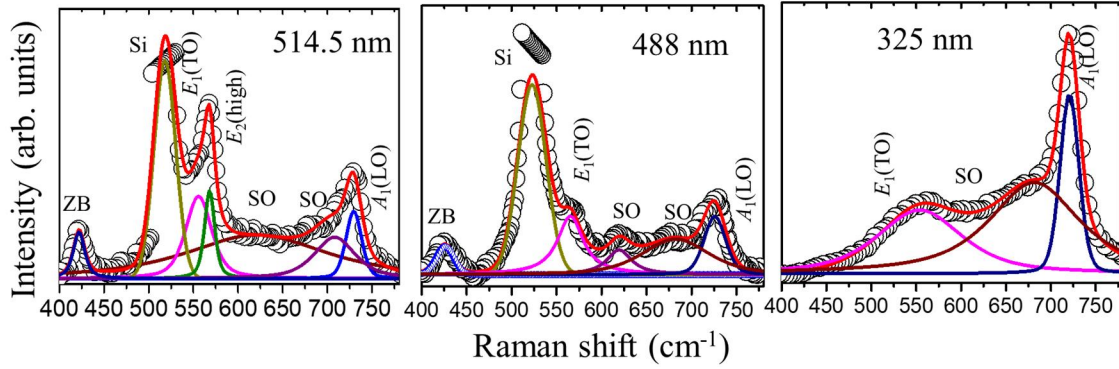
Figure 2.6. Comparison of typical excitation (514.5, 488, and 325 nm) dependent Raman spectra of NWs of sample S3.

Further, the excitation energy dependence of electron-phonon interactions in the GaN NWs of sample S3 was studied by collecting the Raman spectra of NWs using three excitation wavelengths of 514.5, 488, and 325 nm for understanding the presence of FI in these samples. A comparison of the typical Raman spectra of sample S3, excited by three wavelengths is shown (Fig. 2.6). The relative intensity ratios of $(I_{E_1(\mathrm{TO})}/I_{A_1(\mathrm{LO})})$ are estimated to be 1.21, 1.00, and 0.35, respectively for the three wavelengths. The values clearly show that the LO phonons

are strongly interacted by the combination of FI and DP interactions when the excitation source is close to the resonance condition of GaN.

2.9 Defect Induced Free Carrier Plasmon-Phonon Coupling

The observed shift in A_1(LO) phonon mode of NWs from samples S1 to S3 (Figs. 2.5d-f) may be due to the interactions among LO phonons and free charge carriers in the samples, as such shift is not possible in A_1(LO) phonons alone if it is associated with strain, or as an effect of temperature.[13] Further, considering the similar experimental conditions for all the samples in the present study, with identical lattice mismatch due to Si substrate and a constant low power laser excitation of <1 mW, the shift cannot be attributed to the strain effect to a particular phonon mode or temperature effect. However, for semiconductors, especially in ionic solids the polar LO phonons strongly interact with the free charge carriers such as electrons present in the system by means of Fröhlich interaction. As revealed from the XPS studies, the GaN NWs are expected to possess different doping concentration leading to a variation in the carrier concentration as a function of native defects present in the system.[7,17] The defect induced free charge carriers thus can strongly interact with LO phonons, resulting in the blue shift of A_1(LO) phonon modes from samples S1 to S3. By analyzing the line shape of the coupled plasmon-phonon modes, it has been shown that the free carrier density can be calculated, considering the DP and FI in Raman scattering cross-section.[13,26]

The Raman scattering intensity ($I(\omega)$) as a function of phonon (ω) and plasmon (ω_p) frequency is described by

$$I(\omega) \propto A(\omega) \times \text{Im}\left[\frac{-1}{\varepsilon(\omega)}\right] \dots\dots\dots\dots\dots\dots\dots\dots\dots\dots\dots\dots\dots\dots (2.2)$$

where $A(\omega)$ is the correction factor by DP and FI in terms of Faust-Henry coefficient (C), TO phonon (ω_{TO}) and LO phonon (ω_{LO}) frequencies, plasmon damping constant (γ), and phonon damping constant (Γ), and $\varepsilon(\omega)$, being the dielectric function, is described as

$$\varepsilon(\omega) = \varepsilon_\infty \times \left\{ 1 + \frac{\omega_{LO}^2 - \omega_{TO}^2}{\omega_{TO}^2 - \omega - i\Gamma\omega} - \frac{\omega_p^2}{\omega^2 + i\gamma\omega} \right\} \quad \dots\dots\dots\dots\dots\dots\dots\dots\dots (2.3)$$

The line shape of A_1(LO) phonon modes of the three NWs samples (Figs. 2.5d-f) were fitted using the equation (2.2), by adjusting the fitting parameters ω_p, γ, Γ, and C. From the fitted values of ω_p, γ and using the effective mass of the electron (m^*) in GaN, the carrier concentration $n_e = (\omega_p^2 \varepsilon_\infty m^*)/4\pi e^2$ and mobility $\mu_e = e/m^*\gamma$ of the NWs were estimated and tabulated (Table 2.2).

Table 2.2. Carrier concentration and mobility of the samples calculated from line shape analysis of the coupled LO phonon mode.

Sample	Ga/N ratio	n_e (cm^{-3})	μ_e (cm^2.V^{-1}.s^{-1})
S1	0.715	4.4×10^{16}	443
S2	0.696	1.6×10^{17}	234
S3	0.670	6.8×10^{17}	57

The estimated n_e and μ_e values of the three samples show the increase in n_e from 4.4×10^{16} cm^{-3} for sample S1 to 6.8×10^{17} cm^{-3} for S3, whereas μ_e is found to decrease from 443 cm^2.V^{-1}.s^{-1} for S1 to 57 cm^2.V^{-1}.s^{-1} for S3. Although, the NWs are not extrinsically doped with any dopants such as Si (n-type dopant), the increase in the values of n_e further confirms the presence of native donor defects such as V_N and O_N. In GaN, the native defects like V_{Ga}, V_N, O_N and the defect complexes $2O_N$, V_{Ga}-O_N, and V_{Ga}-$3O_N$ are known to form acceptor, donor or double donor states, respectively.[27,28] The increase in the density of donor states over acceptors are

thus responsible for increase in the free carrier concentration for the NWs of S3 as compared to that of S1. Similarly, the reduction in mobility of GaN NWs from S1 to S3 can also be attributed to the increase in the defect density in S3 as compared to that of the S1. Furthermore, the variations of n_e and μ_e with respect to Ga/N ratios in NWs are analyzed (Fig. 2.7) to understand the role of native defects in electron-phonon coupling with respect to growth parameters of NWs. The increase in carrier concentration and the decrease in mobility with decreasing Ga/N ratio were observed in the GaN NWs. The NWs having Ga/N ratio close to the stoichiometric values (0.715) are found to have the lowest carrier concentration (4.4×10^{16} cm^{-3}) and highest mobility (443 cm^2.V^{-1}.s^{-1}). On the other hand, the NWs having lowest Ga/N ratio (0.670) are found to possess the large carrier concentration (6.8×10^{17}cm^{-3}) with very low mobility (57 cm^2.V^{-1}.s^{-1}). The off-stoichiometry of Ga/N ratio in NWs enhanced the presence
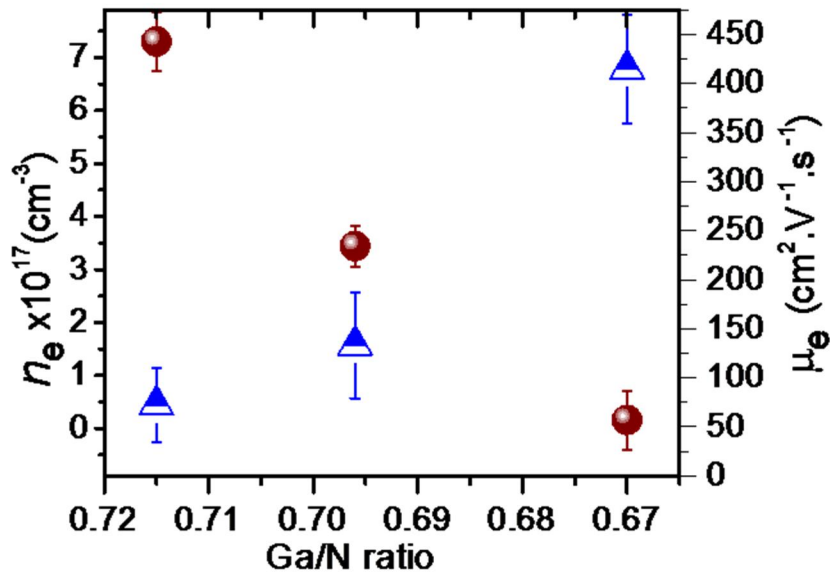
Figure 2.7. Variation of free carrier density and carrier mobility with respect to Ga/N ratio in GaN NWs.

of native defects V$_N$, V$_{Ga}$ which contributed to the resultant free charge carrier concentration in the NWs. In addition, the increase in O impurities with off-stoichiometry further enhanced the carrier density due to the formation of O$_N$ donors, resulting in the large net charge carrier

concentration in NWs of sample S3. Due to enhanced scattering among large carrier density and scatting between free carriers and native defects in NWs, the charge mobility is lowest in the NWs having off-stoichiometry.[29,30] The XPS results of Ga/N ratio and O impurities in GaN NWs, and the Raman spectroscopic analysis of variations in n_e and μ_e, strongly emphasizes the role of native defects in electron-phonon coupling which can vary with growth parameters, even without the extrinsic doping in NWs.

2.10 Native Defects Originated Optical Transitions and Corresponding Electron-Phonon Coupling Characteristics

The presence of native defects and their role in electron-phonon coupling during the radiative transitions in GaN NWs were investigated using PL spectroscopy. An ultra violet (UV) laser of 325 nm wavelength was used to excite the NWs and the emission spectra were recorded at room temperature (300K) and at 80K. The PL spectra of samples S1, S2, and S3 collected at 300K (Figs. 2.8a-c), and 80K (Figs. 2.8d-f) are shown. The luminescence from the NWs of sample S1 at 300K, shows a broad band between 3.0-3.6 eV (Fig. 2.8a). A clear splitting of the broad band is observed on cooling the sample to 80K (Fig. 2.8d). The peak around 3.51 eV corresponds to the emission due to the recombination of electron-hole pairs from a free exciton (FE). Along with the FE emission, the emission peaks around 3.47, and 3.27 eV are also observed in the PL spectra. The peak at ~3.47 eV corresponds to the emission due to radiative recombination of electron-hole pairs from excitons, bound to the sallow donor (DBE) states created by V_N and O_N.[31] The peak around 3.27 eV is attributed to recombination of the donor-acceptor pair (DAP), due to a transition of electrons from a shallow donor state (V_N, O_N) to a deep acceptor state of V_{Ga}. A broad peak situated between 2.7-3.0 eV, in the low temperature PL spectra (Fig. 2.8d) corresponds to the blue luminescence (BL), which is often

observed in undoped GaN and is assigned to the defect transitions involved by shallow acceptors (V_{Ga}) and deep donors (V_N).[21,31]
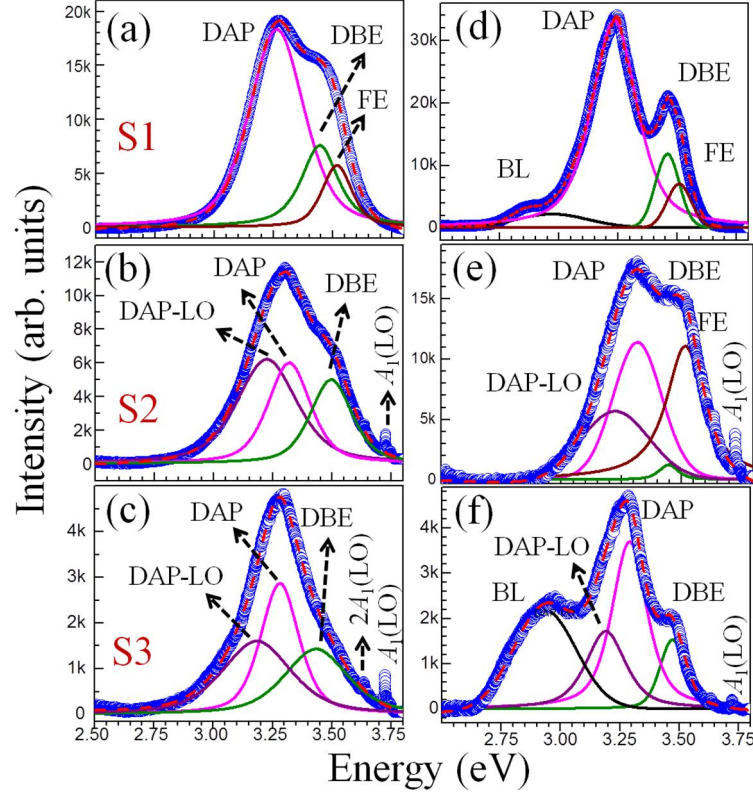
Figure 2.8. Typical PL spectra of GaN NWs of samples (a) S1, (b) S2 and (c) S3, collected at room temperature and their corresponding (d)-(f) low temperature (80K) spectra, respectively.

The PL spectra of sample S2 show a FE emission at ~3.51 eV along with DAP (~3.31) peak which is blue shifted by 40 meV as compared to that of the sample S1 at 80K (Fig. 2.8e). The new emission peak observed around 3.22 eV, which is ~ 90 meV less in energy as compared to the DAP peak, is attributed to the LO phonon replica of DAP (DAP-LO).[21,31] In addition to the LO-phonon replica of DAP, a sharp resonance Raman line of A_1(LO) phonons in PL spectra further confirmed the presence of electron-phonon coupling, as observed in Raman spectroscopic investigations of the samples. The sample S3 emitted the luminescence due to DBE (3.47 eV), and a DAP transition along with its LO phonon replica (DAP-LO)

around 3.19 eV (Figs. 2.8c and 2.8f). However, the luminescence due to FE emission is not observed even at 80 K. The spectra also showed a strong BL peak around 2.9 eV at low temperature. The quenching in luminescence originating due to FE emission is observed with decrease in Ga/N ratio of NWs sample S1 to S3.

The PL study provides clear evidence of the presence of native defects (V_N, O_N, and V_{Ga}) in GaN NWs having different Ga/N ratios, as supported by XPS analysis. Since, the carrier concentration is expected to be higher in the samples grown under N reduced condition (S2 and S3), which favors the formation of native defects, the electron-phonon interaction is strengthened in these samples and consequently a phonon replica (DAP-LO) was observed in the PL spectra collected at both room temperature (Figs. 2.8b and 2.8c) and low temperature (Figs. 2.8e and 2.8f). In general, FE and DBE cannot be observed for semiconductors at room temperature. However, we can observe these luminescent peaks in case of GaN, as the exciton bound to the donor (arising due to N vacancy (V_N)) is having energy ~64 ($\pm$10) meV,[32] which is far above the room temperature thermal energy of 25 meV. The PL spectra collected from samples S2 and S3 also show Raman mode corresponding to A_1(LO) phonon along with its second order mode both at room temperature (Figs. 2.8b and 2.8c) and low temperature (Figs. 2.8e and 2.8f) as well. However, there is no signature of LO phonon modes in the PL spectra of sample S1. The observation of optical phonon modes in PL spectra of samples S2 and S3, further confirms the strong electron-phonon coupling induced by Fröhlich interaction near resonance condition, in the presence of a large number of carriers originating from native defects in these NWs.

2.11 Conclusion

GaN NWs having different Ga/N ratio were grown by changing the flow rate of NH_3 in APCVD technique. Compositional analysis by X-ray photoelectron spectroscopy revealed the presence of different Ga/N ratios in the samples, with sample grown under N rich condition showing composition close to the stoichiometric ratio. Raman spectroscopic analysis revealed different strength of interaction of phonon modes with the lattice deformation potential and Coulomb type Fröhlich interaction for the samples with different Ga/N ratio. The influence of native defect induced carriers on Raman spectra were confirmed from the observed blue shift of A_1(LO) mode with decreasing Ga/N ratio. The carrier concentration and mobility of the GaN NWs were calculated from the line shape analysis of the plasmon coupled phonon modes. The sample with least value of Ga/N ratio showed the highest carrier concentration and the lowest carrier mobility as compared to that the sample close to the stoichiometry, caused by the presence of higher native defect density in the former. PL study exhibited the phonon replica, as well as both the first and the second order optical A_1(LO) phonon modes, which further confirm the presence of strong electron-phonon coupling for the samples grown under N reduced conditions.

2.12 References

[1]   S. Nakamura, T. Mukai, and M. Senoh, Applied Physics Letters **64,** 1687 (1994).

[2]   F. Qian, Y. Li, S. Gradecak, H. G. Park, Y. Dong, Y. Ding, Z. L. Wang, and C. M. Lieber, Nature Material **7,** 701 (2008).

[3]   A. Patsha, S. Dhara, S. Chattopadhyay, K.-H. Chen, and L.-C. Chen, Journal of Materials NanoScience **5,** 1 (2018).

[4]   Y. Li, J. Xiang, F. Qian, S. Gradecak, Y. Wu, H. Yan, D. A. Blom, and C. M. Lieber, Nano Letters **6,** 1468 (2006).

[5] Y. B. Tang, Z. H. Chen, H. S. Song, C. S. Lee, H. T. Cong, H. M. Cheng, W. J. Zhang, I. Bello, and S. T. Lee, Nano Letters **8,** 4191 (2008).

[6] S. Sintonen, P. Kivisaari, S. Pimputkar, S. Suihkonen, T. Schulz, J. S. Speck, and S. Nakamura, Journal of Crystal Growth **456,** 43 (2016).

[7] G. A. Slack, L. J. Schowalter, D. Morelli, and J. A. Freitas Jr, Journal of Crystal Growth **246,** 287 (2002).

[8] X. Zhang, T. Taliercio, S. Kolliakos, and P. Lefebvre, Journal of Physics: Condensed Matter **13,** 7053 (2001).

[9] S. Dhara, S. Chandra, G. Mangamma, S. Kalavathi, P. Shankar, K. G. M. Nair, A. K. Tyagi, C. W. Hsu, C. C. Kuo, L. C. Chen, K. H. Chen, and K. K. Sriram, Applied Physics Letters **90,** 213104 (2007).

[10] T. Kozawa, T. Kachi, H. Kano, Y. Taga, M. Hashimoto, N. Koide, and K. Manabe, Journal of Applied Physics **75,** 1098 (1994).

[11] K. Jeganathan, R. Debnath, R. Meijers, T. Stoica, R. Calarco, D. Grützmacher, and H. Lüth, Journal of Applied Physics **105,** 123707 (2009).

[12] L. H. Robins, E. Horneber, N. A. Sanford, K. A. Bertness, M. Brubaker, and J. Schlager, Journal of Applied Physics **120,** 124313 (2016).

[13] H. Harima, Journal of Physics: Condensed Matter **14,** R967 (2002).

[14] C.-C. Chen, C.-C. Yeh, C.-H. Chen, M.-Y. Yu, H.-L. Liu, J.-J. Wu, K.-H. Chen, L.-C. Chen, J.-Y. Peng, and Y.-F. Chen, Journal of the American Chemical Society **123,** 2791 (2001).

[15] P. Sahoo, J. Basu, S. Dhara, H. C. Fang, C.-P. Liu, T. Ravindran, S. Dash, and A. K. Tyagi, Journal of Materials Science **47,** 3447 (2012).

[16] H.-J. Choi, *Semiconductor Nanostructures for Optoelectronic Devices* (Springer, 2012)

[17] S. Yadav, C. Rodríguez-Fernández, M. M. de Lima Jr, A. Cantarero, and S. Dhar, Journal of Applied Physics **118,** 225703 (2015).

[18] V. Thakur and S. Shivaprasad, Applied Surface Science **327,** 389 (2015).

[19] A. K. Sivadasan, G. Mangamma, S. Bera, M. Kamruddin, and S. Dhara, Journal of Applied Physics **119,** 174304 (2016).

[20] S. Parida, A. Patsha, S. Bera, and S. Dhara, Journal of Physics D: Applied Physics **50,** 275103 (2017).

21 A. Patsha, S. Amirthapandian, R. Pandian, and S. Dhara, Journal of Materials Chemistry C **1,** 8086 (2013).

22 V. Y. Davydov, I. Goncharuk, A. Smirnov, A. Nikolaev, W. Lundin, A. Usikov, A. Klochikhin, J. Aderhold, J. Graul, and O. Semchinova, Physical Review B **65,** 125203 (2002).

23 P. Sahoo, S. Dhara, S. Dash, A. K. Tyagi, B. Raj, C. R. Das, P. Chandramohan, and M. P. Srinivasan, International Journal of Nanotechnology **7,** 823 (2010).

24 S. Sahoo, V. Sivasubramanian, S. Dhara, and A. Arora, Solid State Communications **147,** 271 (2008).

25 A. Patsha, P. Sahoo, S. Dhara, S. Amirthapandian, and A. Tyagi, Journal of Raman Spectroscopy **44,** 651 (2013).

26 G. Irmer, V. Toporov, B. Bairamov, and J. Monecke, Physica Status Solidi (b) **119,** 595 (1983).

27 A. Patsha, P. Sahoo, S. Amirthapandian, A. K. Prasad, A. Das, A. Tyagi, M. A. Cotta, and S. Dhara, The Journal of Physical Chemistry C **119,** 21251 (2015).

28 A. Uedono, S. Chichibu, Z. Chen, M. Sumiya, R. Suzuki, T. Ohdaira, T. Mikado, T. Mukai, and S. Nakamura, Journal of Applied Physics **90,** 181 (2001).

29 H. Morkoç, *Handbook of Nitride Semiconductors and Devices, Materials Properties, Physics and Growth*, Vol. 1 (John Wiley & Sons, 2009).

30 S. M. Sze and K. K. Ng, *Physics of Semiconductor Devices* (John wiley & sons, 2006).

31 M. A. Reshchikov and H. Morkoc, Journal of Applied Physics **97,** 061301 (2005).

32 D. C. Look, D. Reynolds, J. W. Hemsky, J. Sizelove, R. Jones, and R. J. Molnar, Physical Review Letters **79,** 2273 (1997).

CHAPTER 3

ION BEAM ASSISTED GROWTH OF Al$_X$Ga$_{1-X}$N NANOWIRES AND GAS SENSING APPLICATION

3.1 Introduction

AlGaN plays a vital role in hetero-structured high electron mobility transistor by employing a two-dimensional electron gas induced at the hetero-interface as a highly conducting channel.[1,2] There are several difficulties in the synthesis of AlGaN NWs. During the growth process, highly reactive atomic N reacts instantly with Al adatoms and limits further diffusion of the adatoms to form AlGaN with a higher atomic percentage of Al.[3] Furthermore, incorporation of oxygen is promoted due to the high chemical affinity of Al towards oxygen and hence it suppresses the growth of AlGaN.[4] Especially, in the commercially viable technique of chemical vapour deposition (CVD), it is very difficult to synthesize AlGaN with a higher percentage of Al, because of the miscibility limit and the requirement of very high temperature (>1100 $^{\circ}$C) for the formation of Ga and Al eutectic alloy in the catalyst assisted vapor-liquid-solid (VLS) process.[5] However, the above mentioned difficulties can be tackled up to a certain extent by adopting the well known ion beam mixing (IBM) techniques, which are useful for alloy formation above the miscibility limit and can be employed to thermodynamically immiscible systems, as well.[6] Moreover, in comparison to the direct implantation, IBM results in a uniform composition throughout the depth of penetration of the irradiation ion.[7,8] Defect creation and simultaneous diffusion of elemental species are anticipated to form alloy with higher incorporation percentage than the conventional process.[6,8] Therefore, the first part of the present chapter is devoted to the synthesis of AlGaN nanowires using ion beam techniques. Along with the IBM technique, a new approach of post irradiation diffusion (PID) process was

adopted for the synthesis of AlGaN nanowires. The motivation to carry out the PID process is to enhance the Al diffusion into GaN in which defects are generated by means of high energy ion irradiation.

After the successful synthesis of AlGaN nanowires, the NWs were utilized for the gas sensing application owing to the chemical and thermal stability of III-V nitrides.[3] It is well known that metal oxides show variation in stoichiometry with time in ambient conditions and hence, the stability is lost resulting in the fluctuation of response. However, the sensitivity of metal oxide based semiconductor devices is very high.[9,10] Nevertheless, the sensitivity of the device can be compromised at the cost of the stability of the nitride-based semiconductor for long term applications. The second part of the present chapter describes the methane (CH_4) gas sensing behavior of the $Al_xGa_{1-x}N$ NWs synthesized in the IBM process. The primary focus is to investigate the CH_4 response of $Al_xGa_{1-x}N$ NWs and establish the underlying mechanism.

3.2 Synthesis of AlGaN Nanowires

AlGaN NWs were synthesized by two processes, namely IBM and PID techniques using GaN NWs grown by atmospheric pressure CVD (APCVD) technique in the catalyst assisted vapor-liquid-solid (VLS) process. The detailed growth process of GaN NW is described in the Chapter 2.[11] In IBM process, Ar^+ ion was chosen because of its inert nature and to maximize the nuclear energy loss in Al layer with their atomic masses are close to each other. The required thickness of Al layer was calculated as ~25 nm with the help of stopping and range of ions in matter (SRIM) analysis for the Ar^+ irradiation with the energy of 25 keV. Al layer (~25 nm) was coated on as-grown GaN NWs using the thermal evaporation technique. Al/GaN was irradiated with Ar^+ (25 keV) at fluences of 1E16 and 5E16 ions·cm^{-2}. The *in-situ* monitoring of fluence for the ion beam was carried out with the help of a Faraday cup. Two

separate irradiated samples were selected for the annealing process at 900 and 1000 $^{\circ}$C in N_2 (5N pure) atmosphere for 5 min. On the other hand, for the PID process, prior to the coating of Al (~25 nm thick), the GaN NWs were irradiated with Ar^+ ion keeping the energy and fluences of the Ar^+ same as in case of IBM process. Similarly, the samples were also annealed with the above mentioned conditions as a final step.

3.3 Morphological Analysis

The typical FESEM image of as-grown GaN NWs (Fig. 3.1) used for the IBM and PID processes show smooth and uniform NWs with an average diameter of ~100 nm and length varying from 1-4 µm.
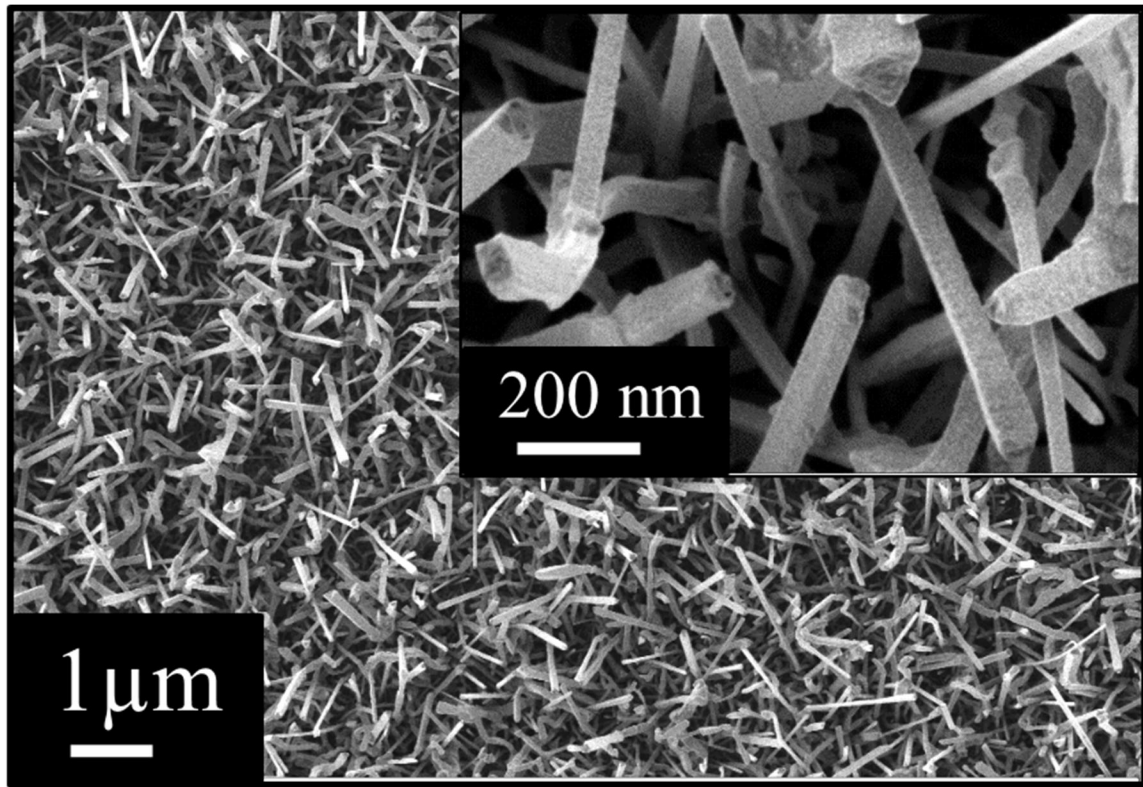
Figure 3.1. Typical FESEM micrograph of as-grown GaN. Inset shows the high magnification image.

Morphologies of NWs, synthesized in the IBM and the PID processes at two different fluences of 1E16 and 5E16 ions·cm^{-2}, after annealing at 900 °C are shown in figures 3.2a(i), 3.1a(ii) and 3.1b(i), 3.1b(ii), respectively.
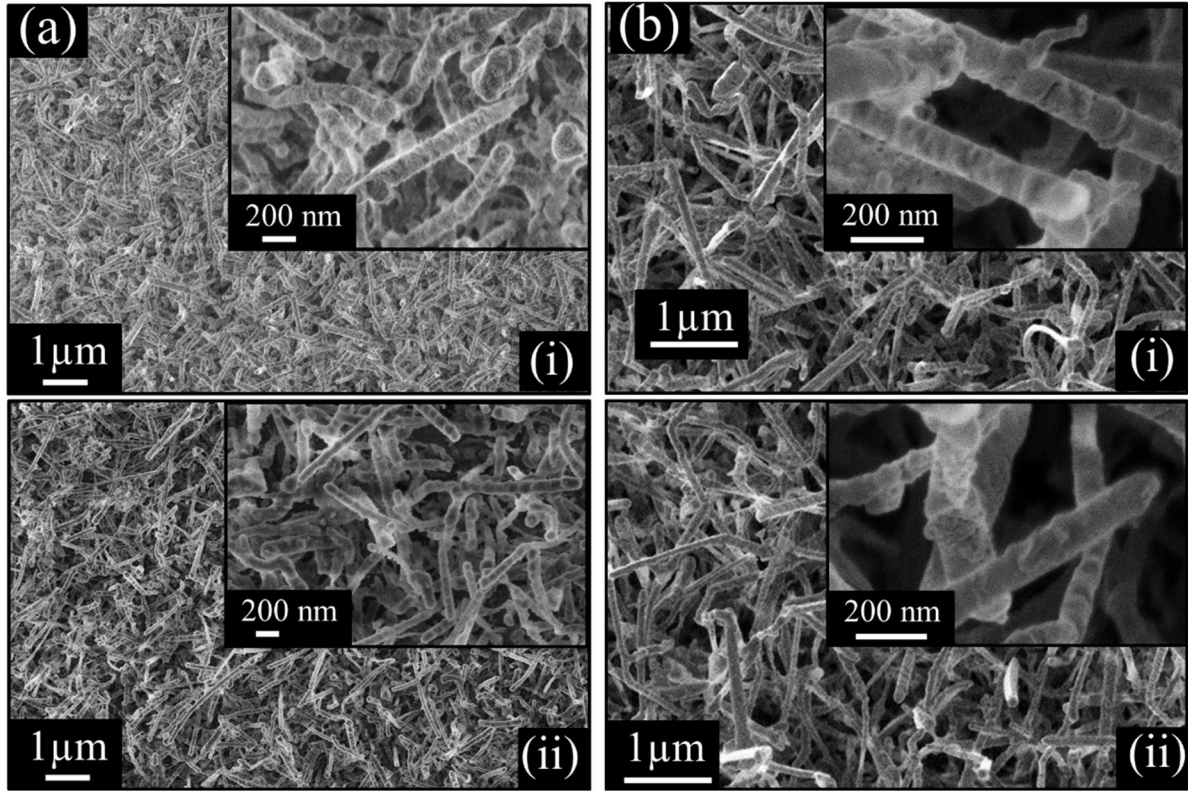
Figure 3.2. Typical FESEM images for the samples synthesized using IBM and the PID techniques for an Ar^{+} fluence of (a) 1E16 and (b) 5E16 ions·cm^{-2}. Al/GaN with post irradiation annealing at 900 °C in the (i) IBM and (ii) PID processes. Insets are showing the high magnification images of the respective samples.

The NWs in the samples synthesized *via* IBM and PID techniques preserve its size, shape and topographic nature after the irradiation with high energy ions with a fluence of 1E16 ions·cm^{-2} (Fig. 3.2a), and 5E16 ions·cm^{-2} (Fig. 3.2b) and subsequent annealing at 900 °C as compared to those for as-grown GaN NWs (Fig. 3.1). Similar observations are also made in the case of post irradiation annealing at 1000 °C (Fig. 3.3) in both the processes.
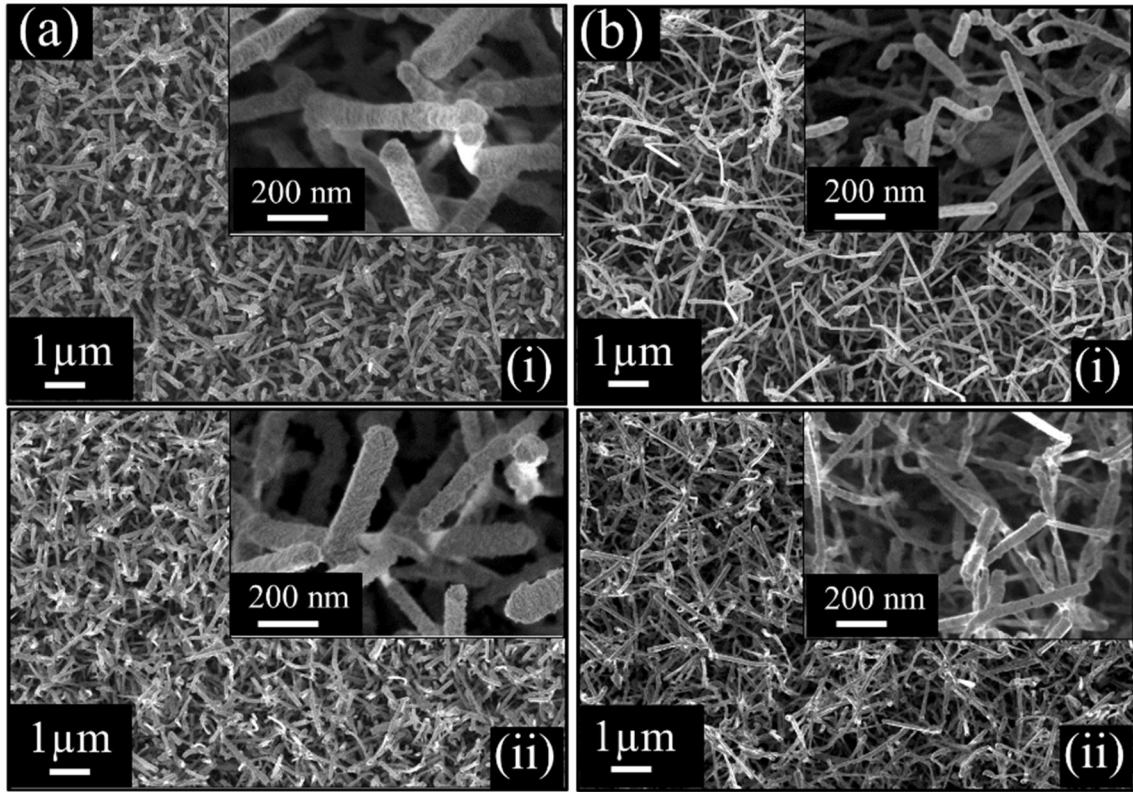
Figure 3.3. Typical FESEM images for the samples synthesized using IBM and the PID techniques for an Ar⁺ fluence of (a) 1E16 and (b) 5E16 ions·cm⁻². Al/GaN with post irradiation annealing at 1000 °C in the (i) IBM and (ii) PID processes. Insets are showing the high magnification images of the respective samples.

3.4 Vibrational Analysis

The typical Raman spectra of as-grown GaN NWs and spectra collected after different steps are shown in figure 3.4 for samples irradiated with a fluence of 1E16 ions·cm⁻² both in the IBM and the PID processes and annealed at different steps. In the vibrational spectrum of as-grown GaN NWs, the peaks centered ~567 and ~725 cm⁻¹ correspond to the symmetry allowed E_2(high) and A_1(LO) modes, respectively, for wurtzite GaN.[12,13] Another peak centered at ~420 cm⁻¹ may correspond to zone boundary phonon modes arising due to the finite crystal size of GaN NWs.[14,15] The peak centered ~520 cm⁻¹ is originated from the crystalline Si substrate. In the case of IBM process, after the thin layer deposition of Al, all the Raman

49

modes are found to be quenched (Fig. 3.4a) due to the screening of excitation laser by Al metal layer. As a first step in the PID process, however, all the modes are also found to disappear (Fig. 3.4b) after the irradiation with Ar^+ because of the production of a large number of point defects leading to the distortion of the lattice structure. After the annealing at 900 °C in N_2 atmosphere, the Raman modes are found to reappear (Figs. 3.4a and 3.4b) due to possible partial removal of defects in the annealing process. In the case of 1000 °C annealed samples, the peaks could revive to their original line shapes with significant peak intensity (Figs. 3.4) as compared to those of the 900 °C annealed samples. However, it could not revive them completely as compared to that of the as-grown sample. The reason may be because of the fact that annealing temperature is not sufficient enough to remove all the point defects created at the time of irradiation. Generally, two third of the melting point temperature (MPT) of the material is required to remove almost all the point defects created in the irradiation process which is ~1650 °C for GaN (MPT ~ 2500 °C).[16] However, high temperature annealing can also create surface defects, which are significant in nanostructures.[8,16] Therefore, further annealing at higher temperatures were not carried out in order to avoid the creation of surface defects. In the case of post irradiation annealing (900 and 1000 °C) of the sample synthesized in the IBM process, the E_2(high) mode exactly reappeared at the same position (~567 cm^{-1}), like that of the as-grown sample (Fig. 3.4a). Similar observations were also found in the case of the sample prepared in the PID process (Fig. 3.4b). The Raman spectral analysis of the samples synthesized *via* IBM and PID process with a fluence of 5E16 ions·cm^{-2} also showed similar characteristics (Figs. 3.4c and 3.4d).[17]
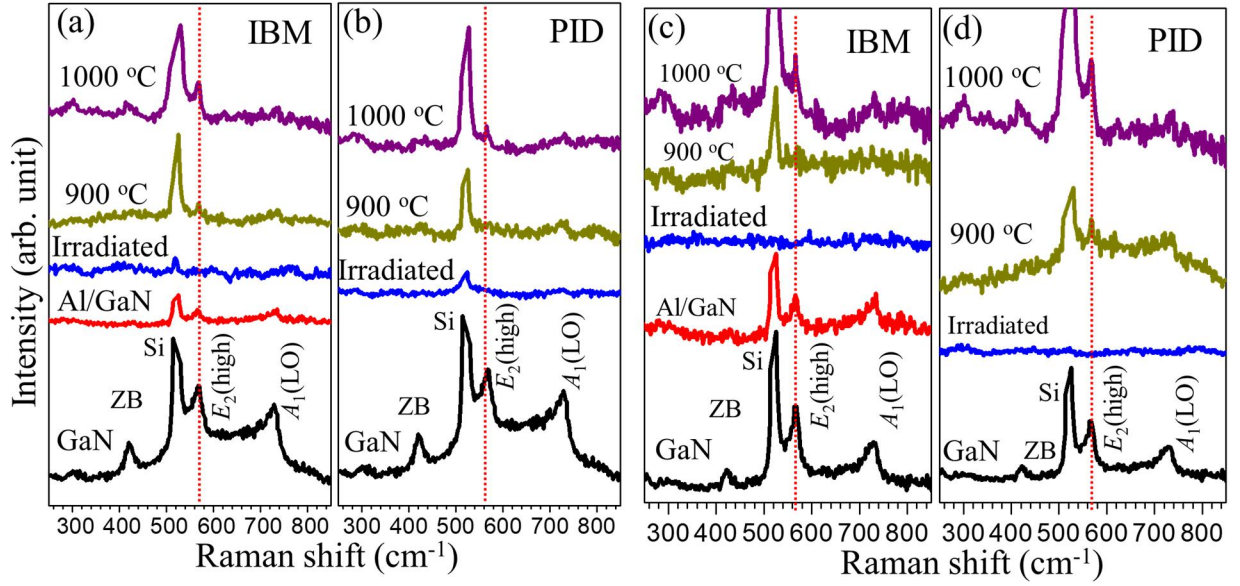
Figure 3.4. Typical Raman spectra of as-grown GaN and Al/GaN NWs in different steps of the (a) IBM and (b) PID process with irradiation fluence of 1E16 ions·cm^{-2}. (c) IBM and (d) PID processes with irradiation fluence of 5E16 ions·cm^{-2}. Vertical dashed lines are guide to eye for the peak position of E_2(high) mode.

Since the random alloy formation is expected for the AlGaN;[13] hence E_2(high) mode corresponding to AlN is also likely to be observed along with the E_2(high) mode of GaN. The absence of E_2(high) mode corresponding to AlN may be because of the nominal incorporation of Al percentage in GaN, which is not sufficient enough to be probed in the Raman spectroscopy having very low scattering cross section, and as change in the polarizibility is also very minimum in the AlN phase.[12] Whereas, the A_1(LO) mode could not retrieve back the sufficient peak intensity in the Raman spectra even after annealing at 1000 °C. In order to understand the complete behavior of the A_1(LO) mode, resonance Raman spectroscopy (RRS) was carried out with the help of 325 nm (3.815 eV) excitation laser sources with energy higher than the band gap of GaN (3.47 eV at room temperature)[18] invoking Frölich interaction in the presence of strong electron-phonon coupling.[19,20] The typical RRS spectra of the samples irradiated with a fluence of 1E16 ions·cm^{-2} and 5E16 ions·cm^{-2} in both IBM and the PID process are shown in figure 3.5.
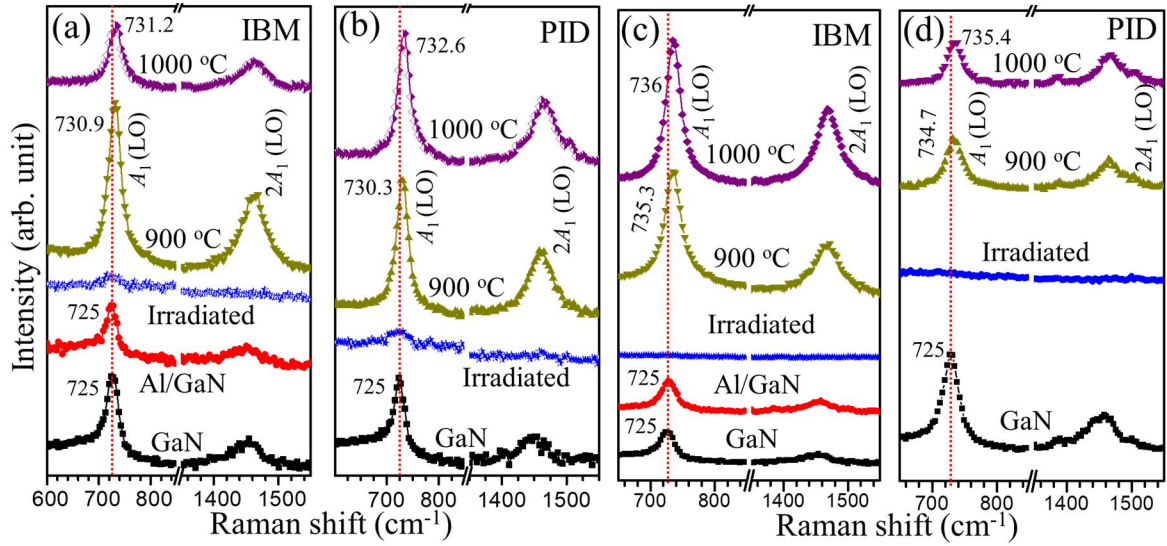
Figure 3.5. Typical resonance Raman spectra of as-grown GaN and Al/GaN NWs in different steps of the (a) IBM and (b) PID process with irradiation fluence of 1E16 ions·cm^{-2}. (c) IBM and (d) PID processes with irradiation fluence of 5E16 ions·cm^{-2}. Vertical dashed lines are guide to eye for the peak position of E_2(high) mode.

Along with the 1st order A_1(LO) mode, the 2nd order $2A_1$(LO) mode was also observed in the as-grown sample. After the irradiation process, all the A_1(LO) modes are found to be diminished in both IBM and PID processes (Fig. 3.5). In the IBM process, once the sample is annealed at 900 °C, the modes are found to reappear with a significant blue shift of A_1(LO) mode ~5.9 cm^{-1} (Fig. 3.5a) as compared to that of the as-grown GaN NWs. The observed blue shift can be attributed to the one mode behavior of A_1(LO) mode in the random alloy model invoked because of the Al incorporation in the GaN.[13] Since the incorporation of a dopant or elements for alloy formation mainly depends on ion energy and irradiation fluence in the IBM process;[3,8] the sample annealed at 1000 °C also show similar blue shift (Fig. 3.5a). In the PID process, the modes are also found to reappear in the 900 °C annealed sample, with a significant blue shift of A_1(LO) mode ~5.3 cm^{-1} (Fig. 3.5b) as compared to that of the as-grown GaN NWs similar to the observation made for the IBM process. Whereas, in the case of the PID process,

the incorporation of Al in GaN depends on ion energy, irradiation fluence, and annealing temperature, as well. In contrast to the IBM process, the driving force involved in the PID process for the migration and incorporation of Al in GaN originate from the thermal energy provided by the annealing process. Thus, there is a significant increase in blue shift (~2.3 cm^{-1}) observed for A_1(LO) mode in the case of 1000 ℃ annealed sample as compared to that for the 900 ℃ annealed sample (Fig. 3.5b). In the case of PID process, the A_1(LO) mode shows a higher blue shift as compared to that of the IBM process, indicating possible higher percentage of Al incorporation in 1000 ℃ annealed sample. A similar analysis was also carried out for the samples synthesized with a fluence of 5E16 ions·cm^{-2} (Fig. 3.5c and 3.5d).
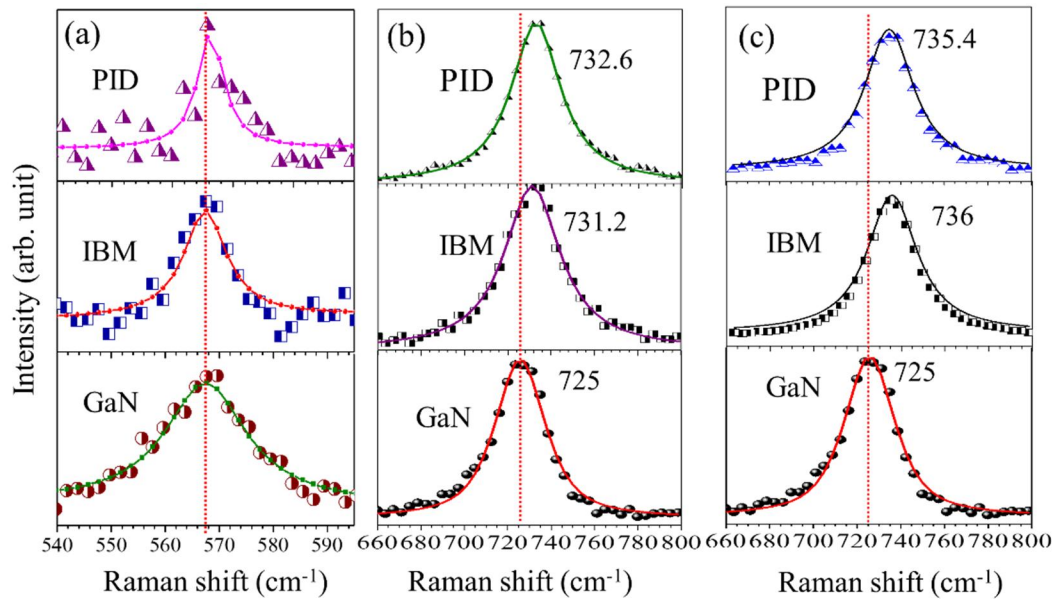
Figure 3.6. Lorentzian line shape fitted (a) E_2(high) phonon mode. A_1(LO) phonon mode of as-grown and 1000 ℃ annealed samples irradiated with a fluence of (b) 1E16 ions·cm^{-2} and (c) 5E16 ions·cm^{-2} in the IBM and the PID processes. Vertical dashed lines are guide to eye for the significant blue shift of A_1(LO) mode.

Figure 3.6 shows the Lorentzian curve fitted E_2(high) mode observed in the Raman spectra (514.5 nm excitation, Fig. 3.6a) and A_1(LO) mode observed in RRS (325 nm excitation,

Fig. 3.6b and 3.6c) for as-grown and 1000 °C annealed samples irradiated with a fluence of 1E16 ions·cm^{-2} (Fig. 3.6b) and 5E16 ions·cm^{-2} (Fig. 3.6c) in the IBM and the PID process.

According to band bowing formalism of random alloy model the percentage of Al incorporation is given by the following equation, which is analogous to the Vegard's law.[15]

$$A_1(LO)_{AlGaN}=A_1(LO)_{GaN}+[A_1(LO)_{AlN}-A_1(LO)_{GaN}]x-bx(1-x)\ldots\ldots\ldots\ldots (3.1)$$

where, 'x' is the Al atomic percentage in AlGaN, and 'b' is the bowing parameter. For lower percentage of Al, the bowing parameter 'b' can be neglected. Thus, the atomic percentage of Al in the AlGaN random alloy was found to ~3.7 % and ~4.6 % in case of the IBM and the PID processes, respectively for the samples irradiated with a fluence of 1E16 ions·cm^{-2}. Similarly, the Al percentage was also estimated as ~6.7 and ~6.3 at% for the samples irradiated with a fluence of 5E16 ions·cm^{-2} in the IBM as well as the PID processes. The incorporation of Al percentage with different fluencies and processes are tabulated (Table 3.1).

Table 3.1. Al atomic percentage in AlGaN with different fluences and annealing temperatures for the IBM and the PID processes.

Ar$^+$ fluence	Al at% in IBM		Al at% in PID	
	900 °C	1000 °C	900 °C	1000 °C
1E16 ions·cm^{-2}	3.6	3.7	3.1	4.6
5E16 ions·cm^{-2}	6.2	6.7	5.9	6.3

The Al incorporation percentage increases with ion fluence in both the processes. In the IBM process, the Al atomic percentage in AlGaN increases ~3 % with increasing the fluence from 1E16 to 5E16 ions·cm^{-2}. Whereas, in the case of PID process, increase in atomic percentage of

Al with the ion fluence is limited to ~1.7 %. Therefore, it may be concluded that IBM is more suitable for the random alloy formation as compared to that of the PID process.

3.5 Luminescence Properties

In order to investigate the optical properties, photoluminescence (PL) spectra for samples irradiated with fluences 1E16 and 5E16 ions·cm^{-2} in both the IBM and the PID processes were also recorded. The typical PL spectra of as-grown and the sample at different conditions are shown in figure 3.7.
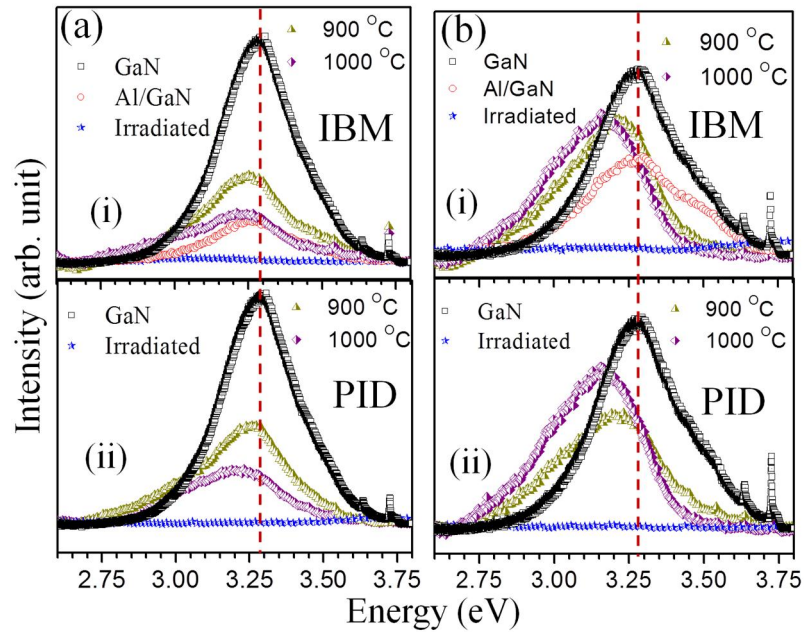
Figure 3.7. Typical PL spectra of as-grown GaN and Al/GaN NWs for different Ar$^+$ fluences of (a) 1E16 and (b) 5E16 ions·cm^{-2} synthesized with different processes of (i) IBM (ii) PID. Vertical dashed lines are guide to eye for the red shift of DAP peak position.

The as-grown GaN NWs show a peak centered at ~3.28 eV, which is attributed to the recombination of the neutral donor-acceptor pair (DAP), originating due to a transition of electrons from the possible presence of a shallow donor state of nitrogen vacancy (V_N) to a deep acceptor state of Ga vacancy (V_{Ga}).[21,22] The quenching of PL emission in the irradiated

sample (Fig. 3.7) is attributed to the trapping of radiative charge carriers by a large number of point defects produced by the high energy ion irradiation. The DAP emission peak is found to evolve with post irradiation annealing at 900 and 1000 °C in both IBM and PID processes. However, for sample irradiated with a fluence of 1E16 ions·cm^{-2} in the case of the IBM process, the evolved DAP emission shows (Fig. 3.7a(i)) a red shift of ~30, and 50 meV for 900 and 1000 °C annealed samples, respectively. Similarly, the DAP emission for sample irradiated with a fluence of 1E16 ions·cm^{-2} in case of the sample synthesized in PID process (Fig. 3.7a(ii)) also shows a red shift of ~30, and 60 meV for 900 and 1000 °C annealing, respectively. The increase in defect density at the time of irradiation leads to the creation of a large number of V_N with a possible generation of a band of defect related energy levels possessing a lower energy state than that of the as-grown GaN. Therefore, the red shift observed for the DAP emission may be attributed to the transition from deep defect levels corresponding to the donor band instead of shallow donor levels.[23] Similar observations were found in the PL studies performed on the as-grown sample and the sample irradiated with higher fluence of 5E16 ions·cm^{-2} (Figs. 3.7b(i) and 3.5b(ii)). Moreover, both the 900 and 1000 °C annealed sample show a higher red shift of the DAP emission peak observed for the sample irradiated with a fluence of 5E16 ions·cm^{-2} as compared to that for the samples synthesized at a fluence of 1E16 ions·cm^{-2}. While ion irradiation can create new defects in some materials, it simultaneously anneals out pre-existing defects in some others (dynamic annealing) with respect to ion energy and fluence.[24] Therefore an additional red shift of DAP emission in the samples irradiated with a higher fluence of 5E16 ions·cm^{-2} can be attributed to the creation of deep donor states by annealing out the existing shallow donor states of GaN. Furthermore, the relative intensity of DAP emission of AlGaN synthesized in both IBM and PID processes with an irradiance

fluence of 5E16 ions·cm^{-2} is greater than that of the samples synthesized with a fluence of 1E16 ions·cm^{-2}. This can be attributed to the dynamic annealing of the defects at the higher fluence of 5E16 ions·cm^{-2}.[25]

3.6 Gas Sensing Measurement

The gas sensing experiments were carried out using a custom-made gas exposure facility system in a dynamic condition under continuous pumping using an oil-free scroll pump (Edward XDS10). The sensing chamber consists of a double-walled stainless-steel chamber of volume 30 liters containing a proportional-integral-derivative (PID) controlled heater. The photograph of the gas sensing setup is shown in figure 3.8. The details of the sensing chamber and the measurement are described elsewhere.[11] In brief, as a first step, the sample with Au contact pad was mounted inside the sensing chamber on the PID controlled heater, which can go up to a maximum temperature of 500 ($\pm$1) $^{\circ}$C. The pressure contacts to the sample were established (Fig. 3.8). Then the system was pre-evacuated to ~1x10^{-2} mbar and was subsequently purged with UHP N$_2$ to avoid the presence of other gases. The cycle was repeated for few times. Two metallic probes in pressure contact with the sample could measure the resistance of the sample with the help of a micro-Ohm meter (Agilent 34401). Finally, the controlled gas mixture (UHP N$_2$ and CH$_4$) was allowed into the sensing chamber through mass flow controllers. All the gases were passed through a moisture trap and hence the chamber was at fixed humidity and on the drier side. The resistance of the sample, as measured in the micro-Ohm meter, was continuously monitored with the help of LabVIEW programming. The response of the sample was recorded upon the gas exposure based on the mechanism of change in resistance.
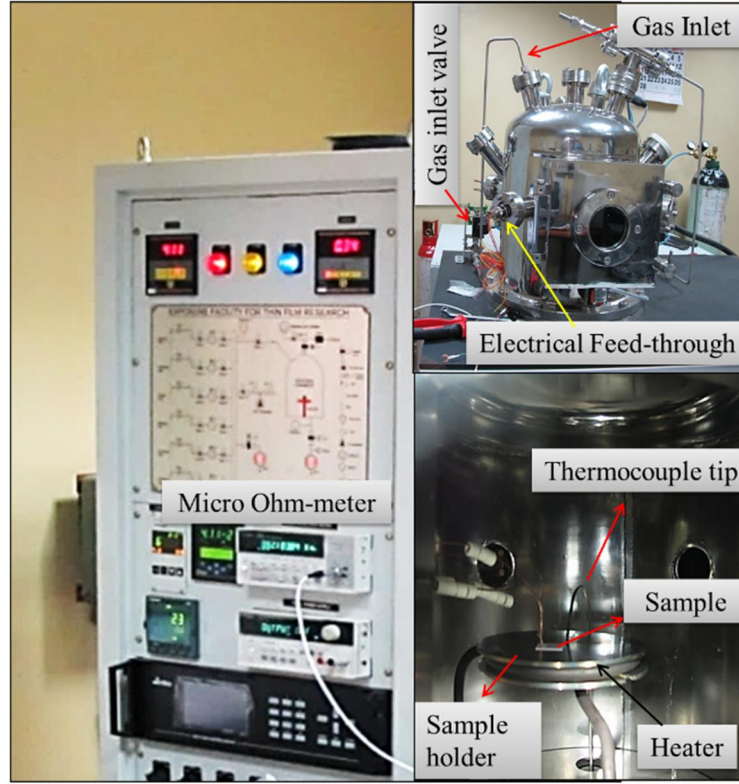
Figure 3.8. The photograph of the gas sensing setup with important components labeled.

3.7 Methane Gas Sensing Performance

The gas sensing of as-grown GaN and $Al_{0.07}Ga_{0.93}N$ was carried out with exposing the sample to CH_4. The change in resistance of the samples was measured as a function of time for different concentrations of the analyte at different operating temperatures. The response curves of the GaN NWs with the exposure of CH_4 gas at temperatures of 150 °C (Fig. 3.9a) and 200 °C (Fig. 3.9b) are shown with a variation of concentration ranging from 100 to 500 ppm. Response (S) of the sensor is calculated as, $S = \dfrac{R_0 - R_G}{R_0}$, where R_0 and R_G are the resistance of the sample in the absence and presence of analyte gas, respectively.
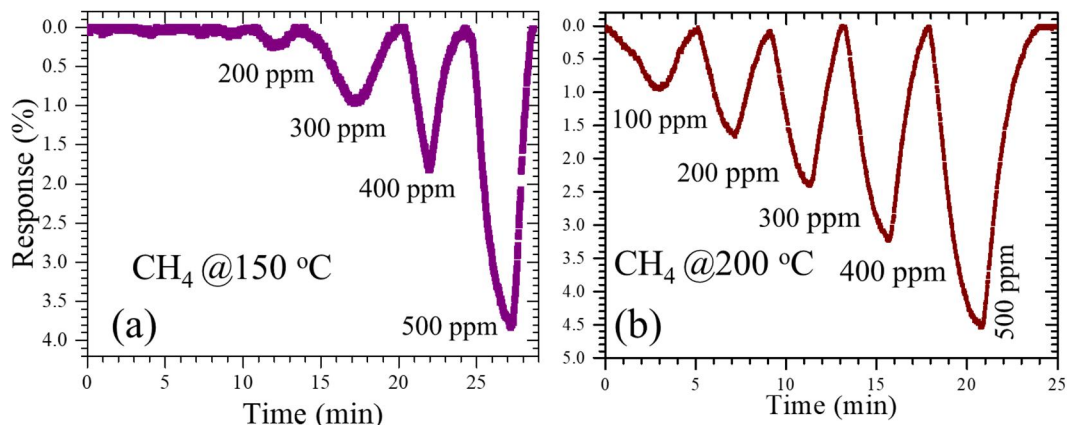
Figure 3.9. CH$_4$ gas sensing response of as-grown GaN NWs at (a) 150 and (b) 200 °C with different gas concentrations ranging from 100 to 500 ppm.

At 150 °C, the as-grown GaN sample does not show a significant response to the 100 ppm of CH$_4$ (Fig. 3.9a). However, it starts showing a measurable response for 200 ppm with a response of ~0.25 % and increases up to ~3.8 % on the exposure of 500 ppm of CH$_4$. With the increase in operating temperature to 200 °C, the GaN NWs even show the response for 100 ppm and the response of ~0.95 % at 100 ppm goes up to ~4.5 % by increasing the amount of exposure gas to 500 ppm (Fig. 3.9b).

The CH$_4$ gas sensing behaviour of Al$_{0.07}$Ga$_{0.93}$N, synthesized *via* IBM process, is shown in figures 3.10a-d. In contrast to GaN NWs, the sample starts responding at 50 °C even for the lowest amount of CH$_4$ exposure of 100 ppm (Fig. 3.10a). At 100 ppm the response is ~2.5 %, which increases up to ~6.0 % for the exposure of 500 ppm. The maximum response of ~20.0 % was recorded with an exposure of 500 ppm at the sample temperature of 150 °C (Fig. 3.10c) implying a ~4.5-fold increase in the response value over that of GaN NWs at 200 °C.
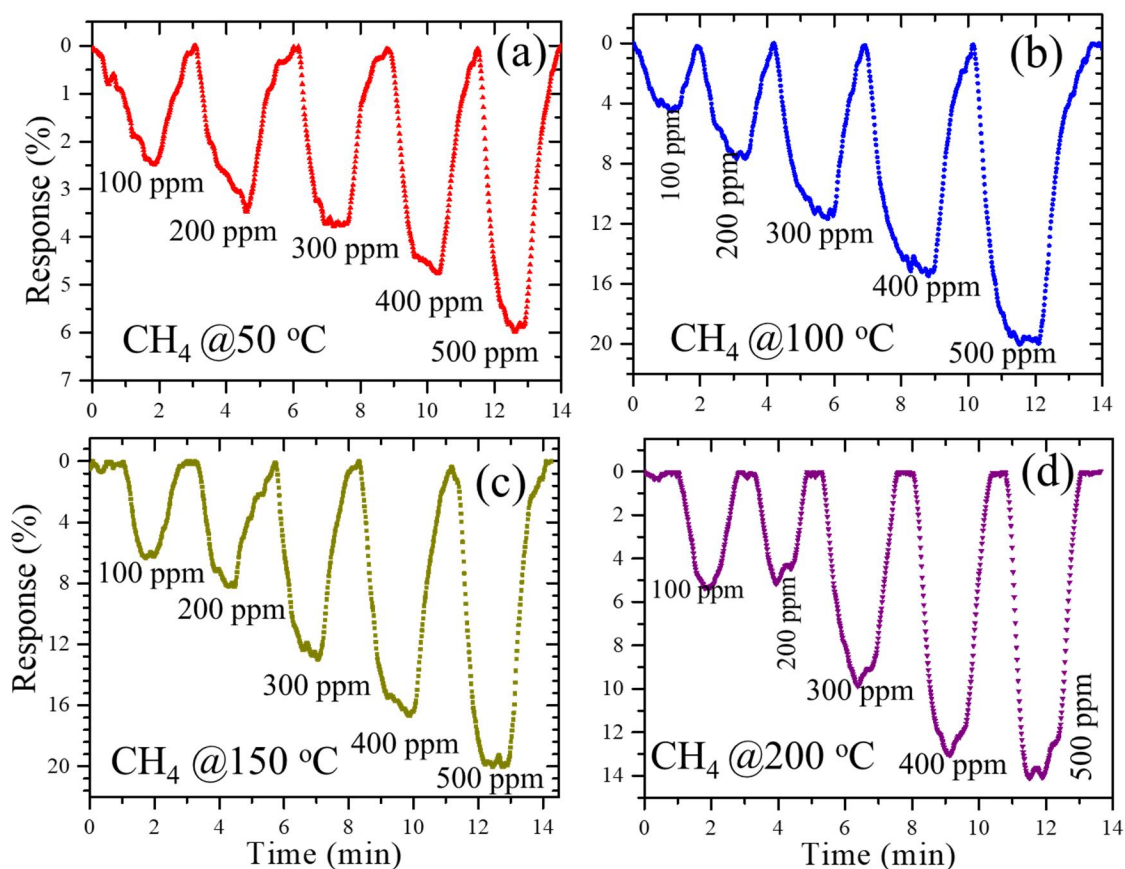
Figure 3.10. CH$_4$ gas sensing response of Al$_{0.07}$Ga$_{0.93}$N NWs at (a) 50, (b) 100, (c) 150 and (d) 200 °C with different gas concentrations ranging from 100 to 500 ppm.

The plots of variation in the CH$_4$ response at different operating temperatures and the analyte concentrations are presented (Fig. 3.11a) for Al$_{0.07}$Ga$_{0.93}$N NWs. The response increases with an increase in the operating temperature up to 150 °C and decreases by further raising the temperature to 200 °C (Fig. 3.11a). The decrease in response is attributed to the reaction kinetics and the adsorption-desorption process of CH$_4$ for the chemisorption based sensor response. Once the desorption process takes over, the sensor response also drops, and the changes of response at 200 ºC for different gas concentration also become random. These phenomena indicate conditions favoring CH$_4$ reaction in the temperature range of 100 to 150 °C, while desorption phenomena occur dominantly above 150 °C. However, the optimum response for GaN is observed at 200 °C. This difference in optimum response temperature can

be attributed to the presence of the additive in the system.[26] Incorporation of additive or dopant in the semiconductor can generate active sites which leads to an increase in surface energy.[26-28] Therefore, the kinetics of the reactions are affected leading to different adsorption and desorption rates at a particular temperature. In the present study, Al acts as a dopant in GaN for the modification of the optimum sensing temperature. Notably, $Al_{0.07}Ga_{0.93}N$ NWs showed stable sensor response with high repeatability over a period of few months.
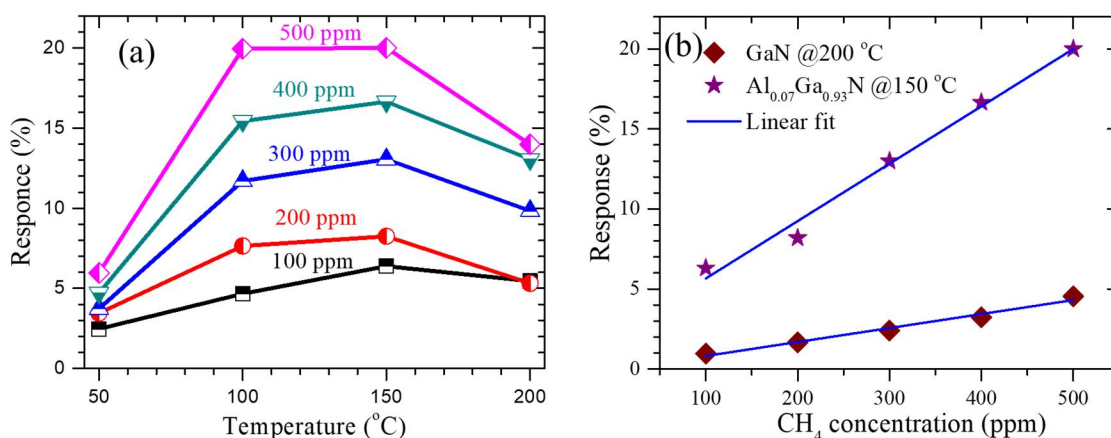
Figure 3.11. (a) Variation of CH_4 gas response towards $Al_{0.07}Ga_{0.93}N$ with respect to temperature and analyte concentration. Solid lines are guide to eye for the variation. (b) Comparative sensing response of GaN and $Al_{0.07}Ga_{0.93}N$ as a function of CH_4 concentration at operating temperatures of 150 and 200 °C, respectively. Solid lines are linear fit for the recorded response.

Further, as a comparative study, the variation of sensing response as a function of analyte concentration (Fig. 3.11b) is depicted at the optimum operating temperatures of 200 °C for as-grown GaN and 150 °C for $Al_{0.07}Ga_{0.93}N$ samples. Both the samples show nearly linear behaviour, signifying the sufficient number of available active sites even after the exposure of 500 ppm of CH_4. Interestingly, it can be easily inferred from figure 3.11b that in case of the $Al_{0.07}Ga_{0.93}N$, there is always a possibility of detecting a lower concentration (<100 ppm) of CH_4 than that for GaN with a significant response of ~4 %. In order to check the selectivity, we have also tested the response of $Al_{0.07}Ga_{0.93}N$ nanowires towards the oxidizing gas O_2, the

second most abundant gas in the atmosphere after the inert N_2. However, there is no measurable change in the resistance of the $Al_{0.07}Ga_{0.93}N$ nanowires with the exposure to O_2 (not shown in the figure). Our study with NO_x, NH_3, and H_2 are also failed in the absence of metallic catalyst nanoparticle for GaN nanostructures.[29,30] The obtained CH_4 sensing response of the present study is compared with the existed literature for other materials and is presented in table 3.2.[9,10,31-36]

Table 3.2. Comparison of CH_4 sensing response towards different materials.

Material	Morphology	Concentration (ppm)	Sensing Temperature ($^\circ$C)	CH_4 Response (%)	Reference
SnO_2	Nanoparticle	500	250	18	10
VO_2	Nanorod	500	50	3	11
SnO_2	Nanoparticle	400	225	6	22
In doped $CaZrO_3$ /MgO composite	Porous structure	1000	600	3	34
Ca- impregnated SnO_2	Micro structure	1000	400	80	35
ZnO	Nanoparticle	100	Room Temperature	80	36
Au decorated VO_2	Nanosheet	500	Room Temperature	70	37
VO_2	Nanorods	500	Room Temperature	26.5	38
GaN	**Nanowire**	**500**	**200**	**4.5**	**Present work**
$\mathbf{Al_{0.07}Ga_{0.93}N}$	**Nanowire**	**500**	**150**	**20**	**Present work**

The key parameters like response and recovery time are compared for the optimum operating temperature of 200 °C for as-grown GaN and 150 °C for $Al_{0.07}Ga_{0.93}N$ with the analyte concentration of 100 ppm. The response and recovery time of $Al_{0.07}Ga_{0.93}N$ is found to be ~33 and 42 s, respectively. Whereas, for GaN the response and recovery time are 126 and 132 s, respectively. Less response and recovery time in $Al_{0.07}Ga_{0.93}N$ NWs as compared to the GaN NWs prove the former as a better material of choice along with the significant sensor

response. The overall performance of $Al_{0.07}Ga_{0.93}N$ nanowires in CH_4 sensing is also found to be remarkable in regard to its low temperature operation with significant response in the optimized condition as compared to the oxide-based sensors (Table 3.2).

3.8 Sensing Mechanism

The CH_4 gas sensing mechanism of GaN was described in an earlier report.[37] GaN NWs were found to respond for the reducing gas CH_4 because of the presence of native defect complexes (V_{Ga}-O_N and $2O_N$), which were supported by both experiment and density functional theory based *ab initio* calculations. The O dopant in N atomic site (O_N) creates the Ga vacancy (V_{Ga}) leading to the creation of most stable defect complexes in the form of $2O_N$ and V_{Ga}-O_N.[37] It is well known that Al is more intended to react with O than Ga, driven by the respective free energy of formation.[38] Therefore, the probability of formation of O_N defect in $Al_{0.07}Ga_{0.93}N$ is enhanced as compared to that in GaN. Additionally, some absorbed oxygen on Al/GaN may diffuse inside the GaN along with Al in the process of ion beam irradiation. In this context, the trace amount of Al and O prefers to occupy the lattice sites of Ga and N, respectively, as a dopant for the overall energy minimization of the crystal.[39] This process can lead to the presence of a relatively large amount of charged O_N defects in $Al_{0.07}Ga_{0.93}N$ NWs. In consequence, it augments the observation of higher response for the $Al_{0.07}Ga_{0.93}N$ NWs at low temperature than that for GaN NWs. It is further discussed at the end of this section. The formation of the oxide phase of Ga or Al in the system is, however, discarded due to the absence of any signature in the Raman spectra (Fig. 3.4). Therefore, a significant majority of the oxygen present in the system belongs to the defects in the form of point defects like O_N and defect complexes of $2O_N$ and V_{Ga}-O_N. The O_N defect in $Al_xGaN_{1-x}N$ is reported to possess negative charge,[39] which may take part in the sensing process. In order to further enrich our

63

argument, the PL spectral study, a well-known characterization tool for defect analysis, was performed. The PL spectra were collected for both as-grown GaN and IBM $Al_{0.07}Ga_{0.93}N$ NWs at room temperature. We have also compared the PL data with those for the GaN sample irradiated and post-annealed without any Al coating to understand that presence of defects is unique to $Al_{0.07}Ga_{0.93}N$ phase and is not due to the irradiation effect on GaN alone (Fig. 3.12).

The luminescence from the as-grown GaN NWs shows broadband in the range of 3.0-3.6 eV (Fig. 3.12a). The peak at ~3.51 eV is assigned to free exciton (FE) corresponding to the emission due to the recombination of electron-hole (*e-h*) pairs.[21] The emission peak ~3.28 eV is also observed in the PL spectrum along with the FE emission. The peak at ~3.28 eV is attributed to the recombination of the donor-acceptor pair (DAP) for a transition of electrons from a shallow donor state (V_N, O_N) to a deep acceptor state of V_{Ga}.[21, 22] The phonon replica of DAP transition is also observed in the PL spectra. In the case of the GaN sample irradiated and post-annealed at 1000 °C, the PL spectrum (Fig. 3.12b) exactly follows the line shape and peak position as that of the as-grown GaN NWs. However, there is a decrease (~0.3 times) in the PL intensity for the irradiated sample, which can be attributed to the increase in the non-radiative centers by the process of irradiation.[17] The PL spectrum of the $Al_{0.07}Ga_{0.93}N$ sample is de-convoluted to 3 peaks centered ~3.25, 3.11 and 2.94 eV (Fig. 3.12c). The luminescence peaks at ~3.25 and 3.11 eV are attributed to the DAP and the phonon replica of the DAP transition, respectively.[17] These two peaks completely follow the line shape and nature of transition as observed in the former two samples of as-grown GaN and post-irradiation annealed GaN.
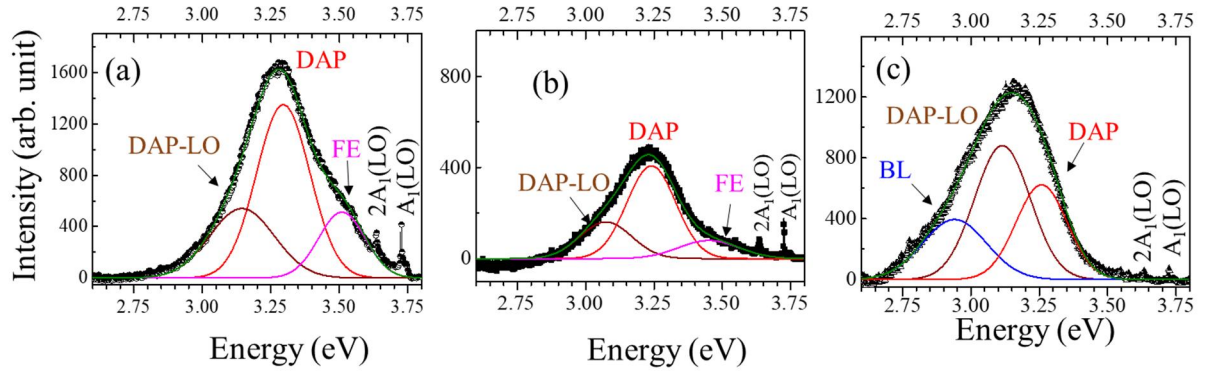
Figure 3.12. Typical PL spectra of (a) as-grown GaN, (b) post-irradiated annealed GaN and (c) $Al_{0.07}Ga_{0.93}N$ NWs.

The peak at ~2.94 eV, arising with significant intensity, can be attributed to the blue luminescence (BL) which is assigned to the transition between the defect states of deep donors (V_N) and shallow acceptors (V_{Ga}).[21] The schematic band diagram is shown (Fig. 3.13) for different defects states which are related to the observed luminescence (Fig. 3.12).
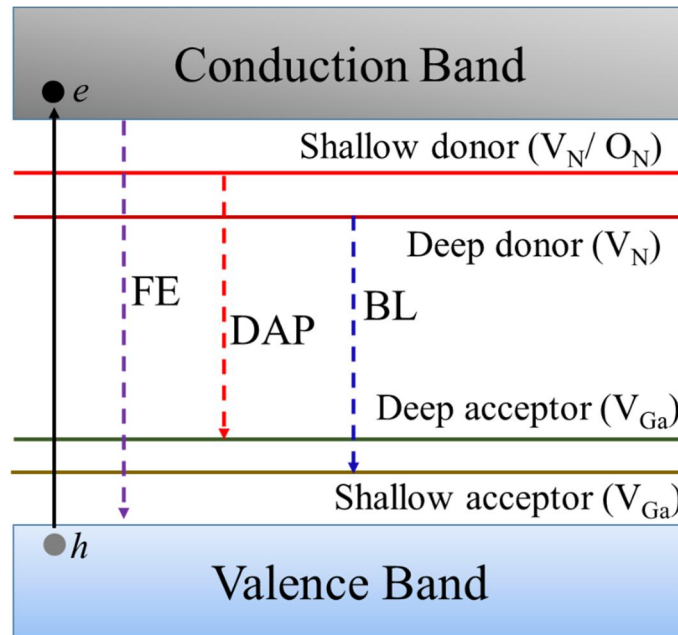
Figure 3.13. Schematic band diagram with different defect states and corresponding luminescence.

The BL band is observed only in the $Al_{0.07}Ga_{0.93}N$ NWs. Considering the above fact, it can be concluded that the number of shallow acceptor-like V_{Ga} defects are higher in $Al_{0.07}Ga_{0.93}N$ NWs than those in the as-grown GaN NWs. Since the post-irradiation annealed

GaN sample does not show any BL band, these defects are not created during irradiation. Generally, the shallow acceptor states are produced in two ways by V_{Ga} defect in GaN. Firstly, if V_N is created in the system, there will be a formation of V_{Ga} in order to maintain the net charge neutrality in the solid.[3] Similarly, V_{Ga} can also be produced in the system, if O_N defects are present, and renders a shallow acceptor state. Thus, the creation of V_{Ga} with the incorporation of O_N is due to the fact of maintaining the net charge neutrality in the system. The V_{Ga}, produced in the system because of the formation of the V_N, can be either a shallow or deep acceptor state.[23] Unlike the V_N, which can create deep or shallow donor states depending on the formation energy, O_N always creates a shallow donor state just below the conduction band.[39-41] Hence, the V_{Ga} formed in the system because of the anticipation of O_N will always form a shallow acceptor state.[3] In the present study for $Al_{0.07}Ga_{0.93}N$ NWs, the BL band in the PL spectra is observed indicating the presence of shallow acceptor level which is created by the V_{Ga}. This observation emphasizes that the excess V_{Ga} are created because of the abundance of O_N over V_N. Hence, the number of O_N defect is higher in $Al_{0.07}Ga_{0.93}N$ NWs as compared to the as-grown GaN NWs.

In the present study, there is a reaction involved in the sensing process of CH_4 with the adsorbed oxygen, present as a negatively charged oxygen defect (O_N) in the nanowires followed by possible reduction to CO_2 and transfer of electrons as charge carriers.

$$CH_4\,(gas) + 4O^- \rightarrow CO_2 + 2H_2O + 4e^- \ldots\ldots\ldots\ldots\ldots\ldots(3.2)$$
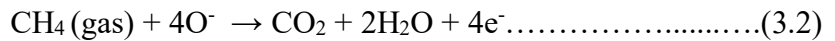
Since charge carriers (in the form of electrons) are generated by the process of above reaction, the resistance of the sample drops in the presence of CH_4. Once the flow of CH_4 is stopped into the sensing chamber, the sample retains back to its original resistance in the operating temperatures with a trace of oxygen available in the chamber. From the earlier discussion on

PL spectroscopic analysis (Fig. 3.12), we have clear evidence that the number of negatively charged O_N defect is higher in $Al_{0.07}Ga_{0.93}N$ NWs as compared to that in the as-grown GaN NWs. Therefore, $Al_{0.07}Ga_{0.93}N$ NWs help in the sensing of CH_4 with a higher response at a comparatively low temperature (50 ^{o}C) than that of GaN NWs.

3.9 Conclusion

AlGaN NWs were synthesized by the IBM and PID processes using GaN NWs grown by atmospheric pressure chemical vapor deposition technique. Vibrational studies with the help of resonance Raman spectroscopy for the post-irradiation annealed Al/GaN sample showed the one-mode phonon behavior corresponding to the A_1(LO) mode of the random alloy. The Al incorporation percentage was estimated from the RRS studies in the AlGaN random alloy and was found to increase with irradiation fluence and post irradiation annealing temperature. The sample synthesized *via* IBM process was utilized for the gas sensing. CH_4 sensing at a low operating temperature (50 ^{o}C) was realized for the AlGaN nanowires synthesized via the ion beam mixing. The maximum response of 20% at 500 ppm is obtained in the temperature range of 100 to 150 ^{o}C. An increase in response by about five times is recorded for AlGaN NWs as compared to that for the as-grown GaN nanowires in the optimum conditions of the respective systems. The gas sensing efficiency in AlGaN NWs is significantly influenced by the presence of the negatively charged native defects.

3.10 References

[1]   Y. Li, J. Xiang, F. Qian, S. Gradecak, Y. Wu, H. Yan, D. A. Blom, and C. M. Lieber, Nano Letters **6,** 1468 (2006).

[2]   O. Ambacher, J. Smart, J. Shealy, N. Weimann, K. Chu, M. Murphy, W. Schaff, L. Eastman, R. Dimitrov, and L. Wittmer, Journal of Applied Physics **85,** 3222 (1999).

3   H. Morkoç, *Handbook of Nitride Semiconductors and Devices, Materials Properties, Physics and Growth*, Vol. 1 (John Wiley & Sons, 2009).

4   S. C. Jain, M. Willander, J. Narayan, and R. V. Overstraeten, Journal of Applied Physics **87,** 965 (2000).

5   A. K. Sivadasan, A. Patsha, S. R. Polaki, S. Amirthapandian, S. Dhara, A. Bhattacharya, B. K. Panigrahi, and A. K. Tyagi, Crystal Growth & Design **15,** 1311 (2015).

6   S. Dhara, Critical Reviews in Solid State and Materials Sciences **32,** 1 (2007).

7   G. S. Was, Progress in Surface Science **32,** 211 (1989).

8   M. Nastasi and J. Mayer, Materials Science and Engineering: R: Reports **12,** 1 (1994).

9   V. Bonu, A. Das, A. K. Prasad, N. G. Krishna, S. Dhara, and A. Tyagi, Applied Physics Letters **105,** 243102 (2014).

10   A. K. Prasad, S. Amirthapandian, S. Dhara, S. Dash, N. Murali, and A. K. Tyagi, Sensors and Actuators B: Chemical **191,** 252 (2014).

11   S. Parida, A. Patsha, S. Bera, and S. Dhara, Journal of Physics D: Applied Physics **50,** 275103 (2017).

12   H. Harima, Journal of Physics: Condensed Matter **14,** R967 (2002).

13   V. Y. Davydov, I. Goncharuk, A. Smirnov, A. Nikolaev, W. Lundin, A. Usikov, A. Klochikhin, J. Aderhold, J. Graul, and O. Semchinova, Physical Review B **65,** 125203 (2002).

14   A. Patsha, S. Dhara, and A. Tyagi, Applied Physics Letters **107,** 123108 (2015).

15   C.-C. Chen, C.-C. Yeh, C.-H. Chen, M.-Y. Yu, H.-L. Liu, J.-J. Wu, K.-H. Chen, L.-C. Chen, J.-Y. Peng, and Y.-F. Chen, Journal of the American Chemical Society **123,** 2791 (2001).

16   S. O. Kucheyev, J. Williams, and S. J. Pearton, Materials Science and Engineering: R: Reports **33,** 51 (2001).

17   S. Parida, P. Magudapathy, A. K. Sivadasan, R. Pandian, and S. Dhara, Journal of Applied Physics **121,** 205901 (2017).

18   S. J. Pearton, *GaN and Related Materials II*, Vol. 7 (CRC Press, 2000).

19   S. Dhara, S. Chandra, G. Mangamma, S. Kalavathi, P. Shankar, K. G. M. Nair, A. K. Tyagi, C. W. Hsu, C. C. Kuo, L. C. Chen, K. H. Chen, and K. K. Sriram, Applied Physics Letters **90,** 213104 (2007).

20   A. K. Sivadasan, A. Patsha, and S. Dhara, Applied Physics Letters **106,** 173107 (2015).

21   M. A. Reshchikov and H. Morkoc, Journal of Applied Physics **97,** 061301 (2005).

22   A. Patsha, S. Amirthapandian, R. Pandian, and S. Dhara, Journal of Materials Chemistry C **1,** 8086 (2013).

23   D. C. Look, G. C. Farlow, P. Drevinsky, D. Bliss, and J. Sizelove, Applied Physics Letters **83,** 3525 (2003).

24   B. Balamurugan, B. Mehta, D. Avasthi, F. Singh, A. K. Arora, M. Rajalakshmi, G. Raghavan, A. Tyagi, and S. M. Shivaprasad, Journal of Applied Physics **92,** 3304 (2002).

25   S. Dhara, A. Datta, C. Wu, Z. Lan, K. Chen, Y. Wang, L. Chen, C. Hsu, H. Lin, and C. C. Chen, Applied Physics Letters **82,** 451 (2003).

26   N. Yamazoe, Y. Kurokawa, and T. Seiyama, Sensors and Actuators **4,** 283 (1983).

27   J. Kaur, R. Kumar, and M. Bhatnagar, Sensors and Actuators B: Chemical **126,** 478 (2007).

28   M. Kumar, B. Singh, P. Yadav, V. Bhatt, M. Kumar, K. Singh, A. Abhyankar, A. Kumar, and J.-H. Yun, Ceramics International **43,** 3562 (2017).

29   A. K. Prasad, P. K. Sahoo, S. Dhara, S. Dash, and A. K. Tyagi, Materials Chemistry and Physics **211,** 355 (2018).

30   P. Sahoo, S. Dhara, S. Dash, S. Amirthapandian, A. K. Prasad, and A. K. Tyagi, International Journal of Hydrogen Energy **38,** 3513 (2013).

31   A. Das, V. Bonu, A. K. Prasad, D. Panda, S. Dhara, and A. K. Tyagi, Journal of Materials Chemistry C **2,** 164 (2014).

32   Y. Suzuki, M. Awano, N. Kondo, and T. Ohji, Journal of the European Ceramic Society **22,** 1177 (2002).

33   S.-D. Choi and D.-D. Lee, Sensors and Actuators B: Chemical **77,** 335 (2001).

34   D. Motaung, G. Mhlongo, I. Kortidis, S. Nkosi, G. Malgas, B. Mwakikunga, S. S. Ray, and G. Kiriakidis, Applied Surface Science **279,** 142 (2013).

35   J. Liang, W. Li, J. Liu, and M. Hu, Materials Letters **184,** 92 (2016).

36   W. Li, J. Liang, J. Liu, L. Zhou, R. Yang, and M. Hu, Materials Letters **173,** 199 (2016).

37   A. Patsha, P. Sahoo, S. Amirthapandian, A. K. Prasad, A. Das, A. K. Tyagi, M. A. Cotta, and S. Dhara, The Journal of Physical Chemistry C **119,** 21251 (2015).

38   J. F. Da Silva and R. J. P. Williams, *The Biological Chemistry of the Elements: The Inorganic Chemistry of Life* (Oxford University Press, 2001).

39   T. Mattila and R. M. Nieminen, Physical Review B **54,** 16676 (1996).

40   M. Toth, K. Fleischer, and M. Phillips, Physical Review B **59,** 1575 (1999).

41   J. Oila, J. Kivioja, V. Ranki, K. Saarinen, D. C. Look, R. J. Molnar, S. Park, S. Lee, and J. Han, Applied Physics Letters **82,** 3433 (2003).

CHAPTER 4

LOCALIZED STUDY: PIEZORESPONSE AND KELVIN PROBE FORCE MICROSCOPY OF III-V NITRIDE NANOSTRUCTURES

4.1 Introduction

Group III nitrides attract remarkable attention because of their electronic and optical properties. III-nitride based 1D nanostructures have emerged as ideal candidates for the building blocks of nanoscale electronic and optoelectronic devices because of the extensive reduction of extended defects.[1] The fruitful application of these nanostructures can be realized through the complete understanding of the physical properties at the nanoscale since the materials at nanoscale change their properties drastically from their bulk counterpart.[2.] Therefore, the measurement of the physical properties with high spatial resolution possess its importance for the performance of nitride-based nanostructured devices.

In recent years, scanning probe microscopy (SPM) based techniques have proven to be an ideal tool for the investigation of physical properties of individual nanostructures. Recent advances in SPM provided an abundant wealth of information on the topography along with the physical properties at nanoscale.[3-6] SPM is extremely versatile and can operate in vacuum, air, and on both insulating as well as metallic samples. These characteristics of SPM enable the measurements of different quantitative and qualitative physico-chemical properties of nanostructures, such as mechanical, optical, or electrical properties. In the present chapter, we have studied the electrical properties of III-V nitride nanostructures using SPM techniques.

In the first part of this chapter, we demonstrate the piezoresponse force microscopy (PFM) imaging of $Al_{0.97}Ga_{0.03}N$ nanorods (NRs) with different crystallographic orientations,

grown *via* plasma-assisted molecular beam epitaxy (PA-MBE). The polarities of the different crystalline planes of *m* and *c* are imaged, and the corresponding piezoresponses are explained on the basis of spontaneous polarization in a unit cell of the crystal. The direction of polarization with respect to the applied electric field is determined and the information regarding the facets are also analyzed from the phase image in the nano-regime.

In the second part of the chapter, we describe the size dependent surface band bending (SBB) of GaN NWs measured by Kelvin probe force microscopy (KPFM). The KPFM measurements are carried out at high vacuum ($\sim 10^{-7}$ mbar) to avoid the effect of surface adsorbents. Single-pass imaging is adopted for the simultaneous measurement of topography, and the contact potential difference (CPD) with a Pt-Ir coated Si tip. Several measurements are carried out for the NWs with different diameter and the corresponding SBB values are correlated to surface states as calculated using *ab initio* density functional theory (DFT).

4.2 PFM Imaging of AlGaN Nanorods

4.2.1 Working principle and instrumental details

Piezoresponse force microscopy is one of the versatile and efficient member of the SPM family and is the best choice for the identification and imaging of ferroelectric domains in the nanostructure. The PFM works on the principle of inverse piezoelectric effect where the crystal deforms with the application of an electrical voltage between the tip and the sample. Unlike macroscopic measurements, the measurements at the nanoscale using direct measurement of the piezoelectric signal by utilizing SPM is extremely difficult.[7] In case of direct piezoelectric measurement, the electromechanical coupling requires detection of the charges of the order of several tens of electron charge, corresponding to ~fA current at ~1 MHz, which is well below

the detection limit. This limitation comes into picture owing to fundamental difficulties such as Johnson noise, and the presence of stray capacitances in the electronics circuit. However, in the case of the inverse piezoelectric effect, the electromechanical response of the surface to the applied bias between the probe and the sample can be detected easily with the well-established detection mechanism. Even small coupling coefficients ~1-5 pm/V can be measured over ~10 nm area, providing a functional basis for high-resolution imaging. Hence, only converse electromechanical measurement is possible on the nanoscale using SPM. Even the very small amount of deformation (~pm) can be detected with adequate accuracy, by measuring converse piezoelectric signal using SPM.[8]

In the present study, an electrically conductive tip was employed for measuring the piezoelectric response in the contact mode of PFM configuration (NT-MTD, NTEGRA). An alternating current, AC bias [$V_{ac}\cos(\omega t)$] was applied between the cantilever and the sample for activating the domains.
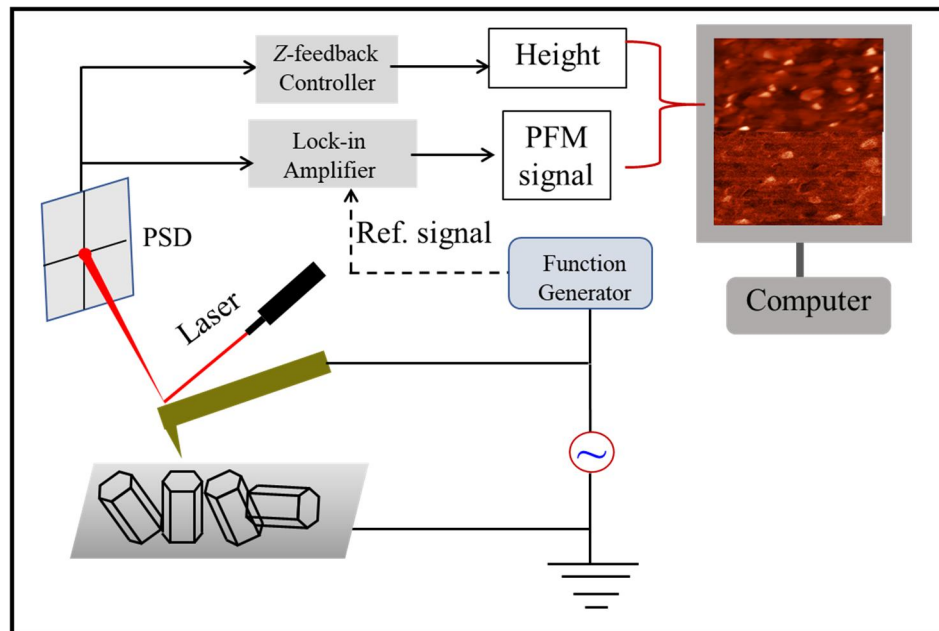
Figure 4.1. Schematic representation of the PFM measurement setup with the major components.

By the application of voltage, the domains locally elongate or contract according to the direction of the electric field, as an effect of inverse piezoelectricity resulting in the deflection in the cantilever. The magnitude of change in cantilever deflection is directly related to the amount of expansion or contraction and hence is proportional to the applied electric field. Thus, the amplitude of the PFM response is proportional to the strength of the piezoresponse, and the phase signal is the representative of the polarization direction of the sample. The schematic of the PFM setup is depicted in figure 4.1 with the major components. In the present study, 5×5 μm^2 area was selected for PFM imaging with the application of an external DC bias (ranging from -5V to +5 V) and AC bias of amplitude 0.3 V with a frequency of 255 kHz between the tip and the sample. A diamond-like carbon coated stiff cantilever (length = 100 μm, width= 35 μm, thickness = 2 μm) with a resonant frequency of 290 KHz, and the spring constant of 11 N/m was used as an AFM tip. The lock-in amplifier deconvolutes the induced signal on the cantilever to measure the amplitude and phase difference with respect to the input AC voltage and produced the respective images over the defined scanned area.

4.2.2 Morphological and vibrational studies of AlGaN nanorods

Morphological and vibrational studies are carried out as basic characterization of $Al_{0.97}Ga_{0.03}N$ NRs prior to the PFM study. The investigation of the surface morphology shows the presence of hexagonal nanostructures as shown for the top (Fig. 4.2a) and tilted (60° tilt angle) (Fig. 4.2b) views in the FESEM images. The typical micrograph of the sample, employed for the present study, shows NRs of ~100-200 nm with length varying in the range of hundreds of nm (Fig. 4.2a). The inset shows a high-resolution image of nanostructures oriented, in different crystalline planes (inset Fig. 4.2a). We observe that these NRs are mostly vertical (Fig. 4.2b) and well oriented, with hexagonal cross sections in the top view. Some of the NRs, however,

are observed horizontal (Fig. 4.2a) and it may be introspected that these structures are initially vertically oriented but have been misoriented from their original position either during the growth or subsequently.
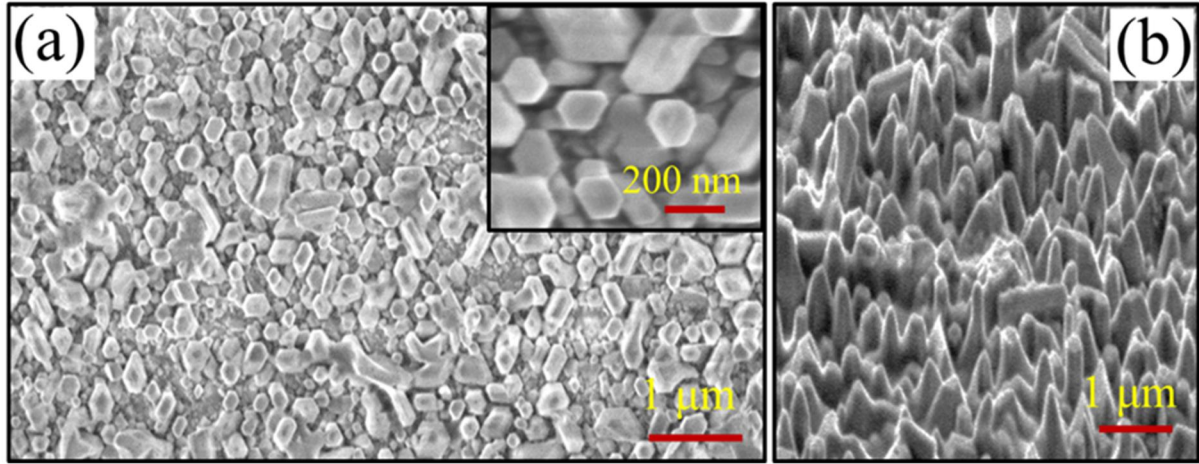
Figure 4.2. Typical FESEM micrograph of $Al_{0.97}Ga_{0.03}N$ NRs for (a) top and (b) tilted (60° tilt angle) views. The inset of (a) shows different crystallographic orientations in the high-resolution image.

The vibrational analysis is carried out with the help of Raman spectroscopy. Typical Raman spectrum of the sample is shown in figure 4.3. The peaks centered around 248, 612, 656 and 878 cm^{-1} belong to the symmetry allowed optical phonon modes corresponding to the E_2(low), A_1(TO), E_2(high) and A_1(LO) vibrations, respectively, confirming the wurtzite phase of $Al_{0.97}Ga_{0.03}N$ sample which is predominantly AlN in nature.[9,10] Apart from the Raman allowed modes, the peak centered ~510 cm^{-1} corresponds to the zone boundary phonon mode arising in the finite size crystallites. The peak ~417 cm^{-1} arises from the sapphire substrate used for the growth of the NRs.[10]
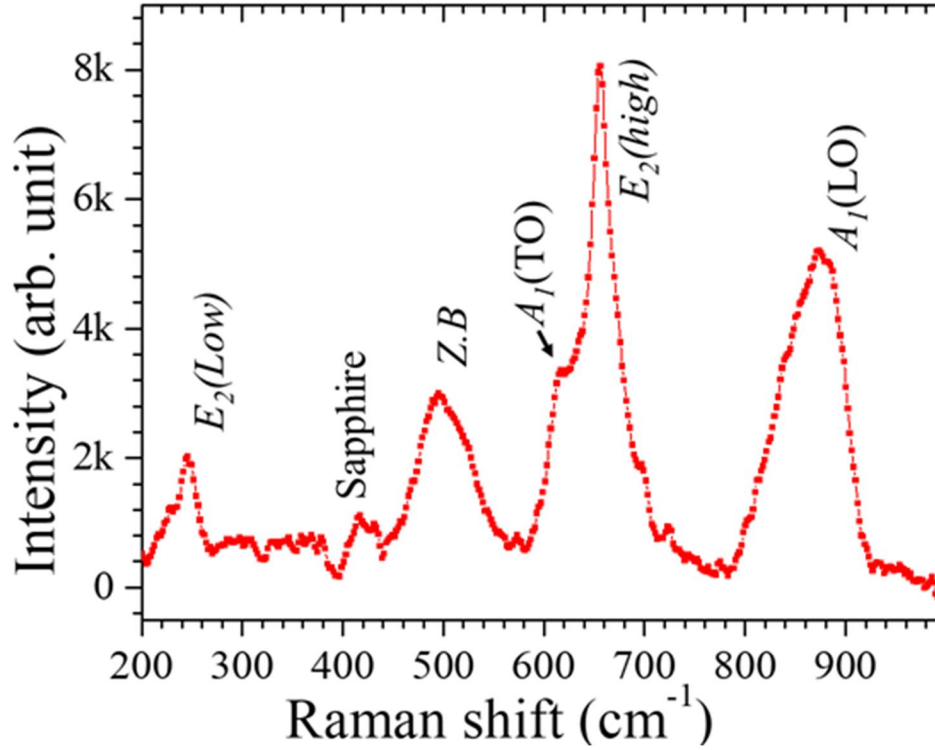
Figure 4.3. Typical Raman spectrum of $Al_{0.97}Ga_{0.03}N$ NRs.

4.2.3 Piezoresponse force microscopic imaging

The piezoresponse of the material is investigated with the help of the PFM imaging. Both topographic and piezoresponse imaging are carried out with the application of combined DC and AC voltage applied between the tip and the sample. One of the typical topography, magnitude and phase images collected over an area of 5×5 μm^2 is presented in the figures 4.4a-c. The corresponding three-dimensional (3D) images are also shown in figures 4.4d-f for better clarity. In typical PFM imaging, there are other sources of signals which can influence the PFM measurements.[11] Therefore, the PFM signal is always associated with some background signal and which is common in SPM based techniques. One of the most influencing phenomena is the electrostatic interaction between the tip and the sample.[11,12] The electrostatic interaction can be minimized by the application of small DC voltage and by using a stiff cantilever, since

the piezoresponse signal due to the electrostatic interaction is inversely proportional to the spring constant of the cantilever.[13] In the present measurement, we have used a DC voltage of 5 V and a stiff cantilever of spring constant 11 N/m. Apart from the electrostatic interaction, a non-local contribution due to capacitive interactions between the cantilever and sample surface can also influence the measured PFM signal. Since the cantilever length (~mm) is significantly higher than the domains (~nm) in the $Al_{0.97}Ga_{0.03}N$ NRs, the non-local interaction results in a small constant background that does not prevent piezoelectric imaging.
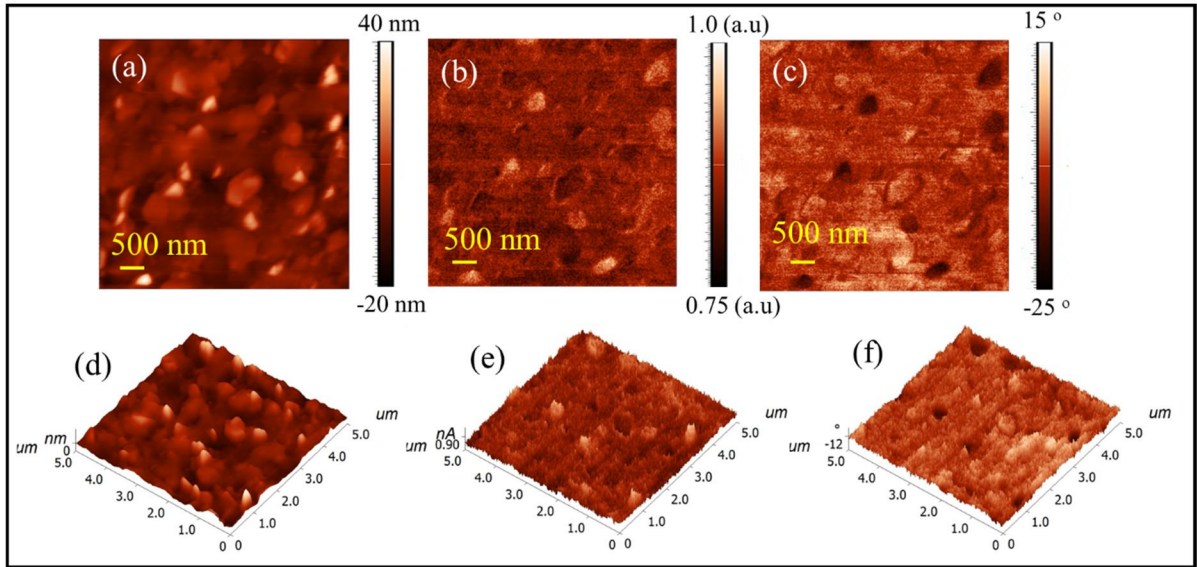
Figure 4.4. (a) The topographic image of $Al_{0.97}Ga_{0.03}N$ nanorods with the corresponding (b) magnitude and (c) phase image. (d)-(f) Corresponding 3D profiles of topography, magnitude and phase images, respectively.

In the height images (Figs. 4.4a and 4.4d), most of the NRs are vertically oriented and distributed over the area. Hexagonal geometry of the crystalline facets is an indication of the wurtzite crystal, which is vertically oriented along c-axis. From the magnitude image, we can clearly observe the piezoelectric response of the NRs with some of the NRs having bright and others having dark contrasts. The bright contrast signifies that the polarization direction (**P**) and the applied field (**E**) are parallel (**E↑↑P**) to each other. Whereas, in the case of the NRs

showing a dark contrast signifies that the applied field and the polarization direction are anti-parallel ($E\uparrow\downarrow P$) to each other. It may also imply that surface of the NRs with bright spots are group III atom (Al, Ga) terminated ($E\uparrow\uparrow P$) and other NRs with dark spot are group V atom (N) terminated ($E\uparrow\downarrow P$).[14,15] NRs with different elemental terminations for group III atom (Al or Ga) or group V atom (N) may occur because of local changes in the chemical environment during the growth process.
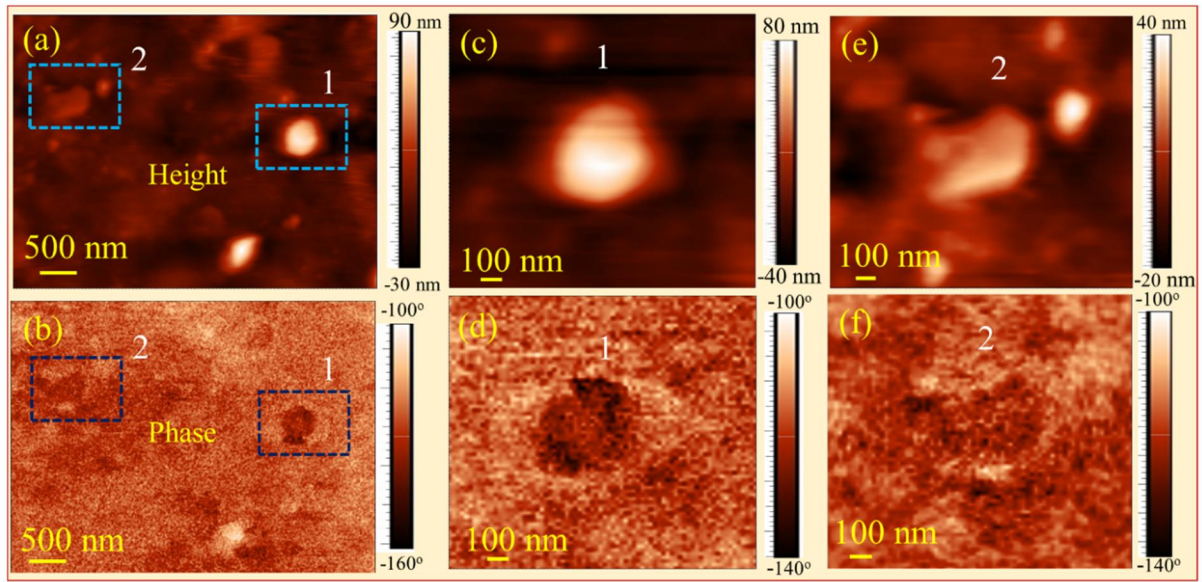
Figure 4.5. (a) The topographic image of $Al_{0.97}Ga_{0.03}N$ NRs with (b) the corresponding phase image; (c) and (e) the zoomed region of the position 1 and 2 marked in dotted boxes with (d), (f) corresponding phase images.

In order to understand the effect of orientation of the nanorods on the piezoresponse, we have carried out the PFM measurements on a sample area containing both vertically and horizontally aligned nanorods. Typical imaging of such area is shown in figure 4.5 for 2D and in figure 4.6 for 3D view.
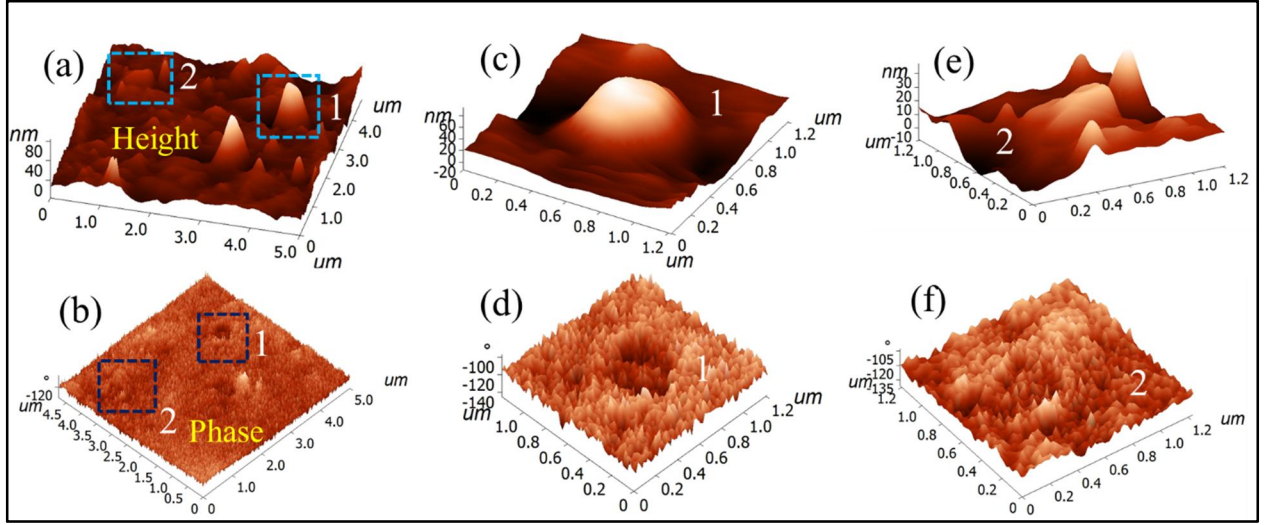
Figure 4.6. (a) The 3D view of the topographic image of $Al_{0.97}Ga_{0.03}N$ nanorods with (b) the corresponding phase image; (c) and (e) the zoomed region of the position 1 and 2 marked in dotted boxes with (d), (f) corresponding phase images.

The NRs are distributed all over the substrate with different size and orientations. Some of the NRs are vertically oriented (marked as 1 in Figs. 4.5a in 2D and 4.6a in 3D views), and some are horizontally laying on the substrate (marked as 2 in Figs. 4.5a in 2D and 4.6a in 3D views). The corresponding phase images are shown in the figures 4.5b in 2D and 4.6b in 3D views. The zoomed topographic and corresponding phase images of the marked position 1 and 2 of the topographic images (Figs. 4.5a in 2D and 4.6a in 3D views) are depicted in figures 4.5c, 4.5d and 4.5e, 4.5f in 2D and 4.6c, 4.6d and 4.6e, 4.6f in 3D views, respectively. In the topographic image (Figs. 4.5a, 4.5c and 4.5e in 2D view; 4.6a, 4.6c and 4.6e in 3D view) both the positions (position 1 and 2) appears to be bright with the height of ~100 and ~50 nm, respectively (Fig. 4.7). In the case of the phase image of marked position 1 (Figs. 4.5b in 2D and 4.6b in 3D views), and the zoomed image (Figs. 4.5d in 2D and 4.6d in 3D views) shows the dark contrast signifying the piezoelectric deformation in the probed direction. Whereas, the phase image of marked position 2 (Figs. 4.5b in 2D and 4.6b in 3D views), and the zoomed image (Figs. 4.5f in 2D and 4.6f in 3D views) does not show any variation in the contrast as

compared to the background, signifying no piezoresponse for the particular direction. The corresponding line profiles of position 1 and 2 for both topographic and phase images are depicted in figure 4.7.
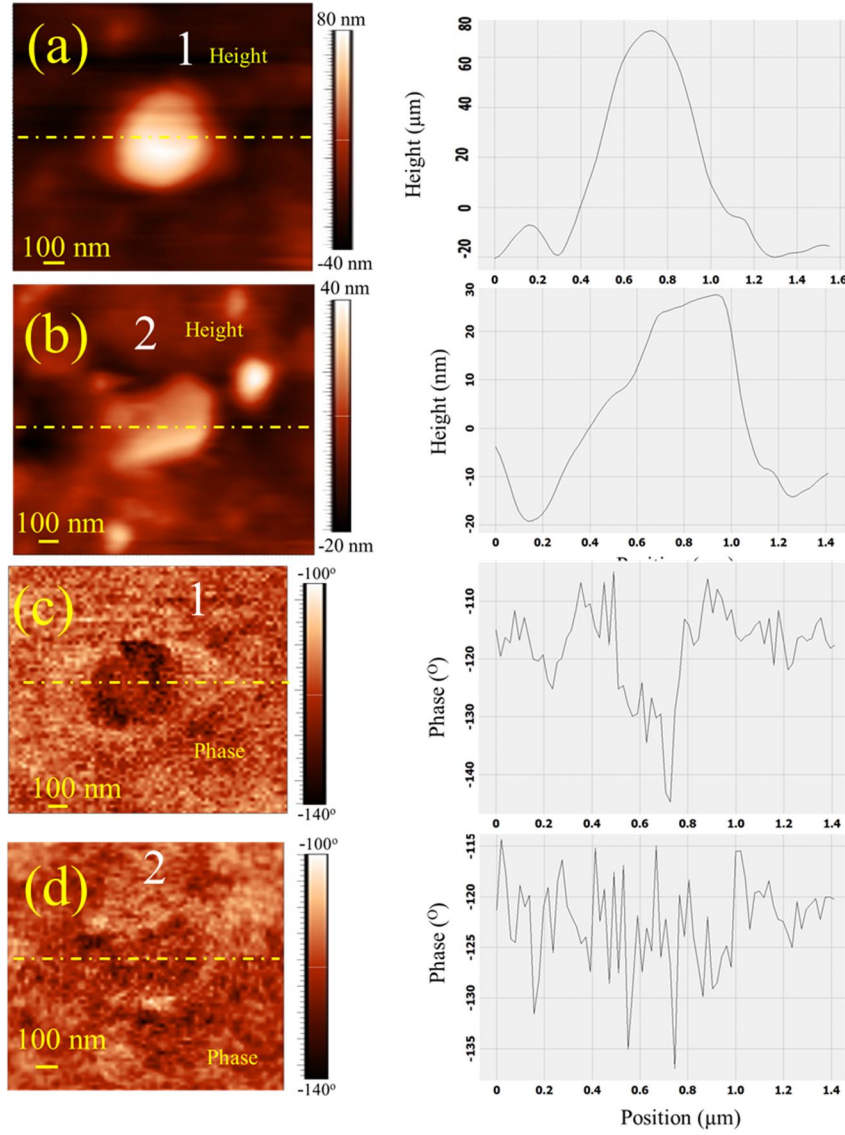
Figure 4.7. (a), (b) Topography of $Al_{0.97}Ga_{0.03}N$ NRs along with the (c), (d) corresponding phase images. Outset of each figure represents the respective line profiles.

4.2.4 Identification of polarity

$Al_{0.97}Ga_{0.03}N$ is a wurtzite crystal, belonging to the hexagonal family. In the case of the wurtzite crystal, there are four crystalline planes namely c-, m-, a- and r-plane (Fig. 4.8a). Along the c-

axis [0001], there are atoms corresponding to the group III and V elements alternatively (Fig. 4.8b). The group III elements show an electropositive character. Whereas, the group V elements yield electronegative character inside the wurtzite crystal. Therefore, the wurtzite crystals constitute an alternative positive and negative plane along the *c*-axis. Because of the alternate polarity, the crystal shows a spontaneous polarization along the *c*-axis. Hence, the *c*-plane of the crystal is called a polar plane. Unlike the *c*-axis, the wurtzite crystal constitutes both electropositive and electronegative atoms in the single crystal planes along the *a*-axis. Therefore, the *a*- or *m*-plane oriented crystal does not show any spontaneous polarization and hence is called as a non-polar plane. The *r*-plane is inclined with *c*- and *m*-plane and therefore shows the semi-polar nature.[16] Considering the above facts, one can expect piezoelectric deformation in the *c*-plane oriented crystals probed in a direction perpendicular to it.
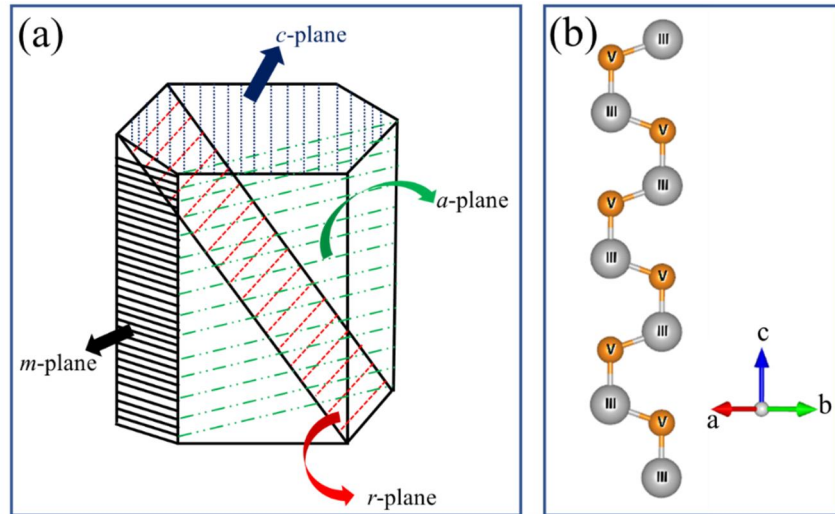
Figure 4.8. (a) Wurtzite crystal structure of III-V nitride indicating the different crystallographic plane and (b) view along the *c*-axis.

In the present study, the marked position 1 shows piezoelectric deformation (Figs. 4.5b and 4.5d in 2D and 4.6b and 4.6d in 3D views), which implies that the crystal is aligned in the *c*-axis, and the corresponding piezoresponse images signify the polar nature of the *c*-plane. The

absence of piezoelectric deformation in the marked position 2 (Figs. 4.5b and 4.5f in 2D and 4.6b and 4.6f in 3D views) signifies that the corresponding plane is non-polar nature. So, the only possibility is that the crystal is aligned either in *a*-plane or *m*-plane. Since most of the wurtzite crystals prefer to grow along *c*- or *m*-plane, the nanorod marked as position 2 (with non-polar nature) is a *m*-plane oriented crystal.
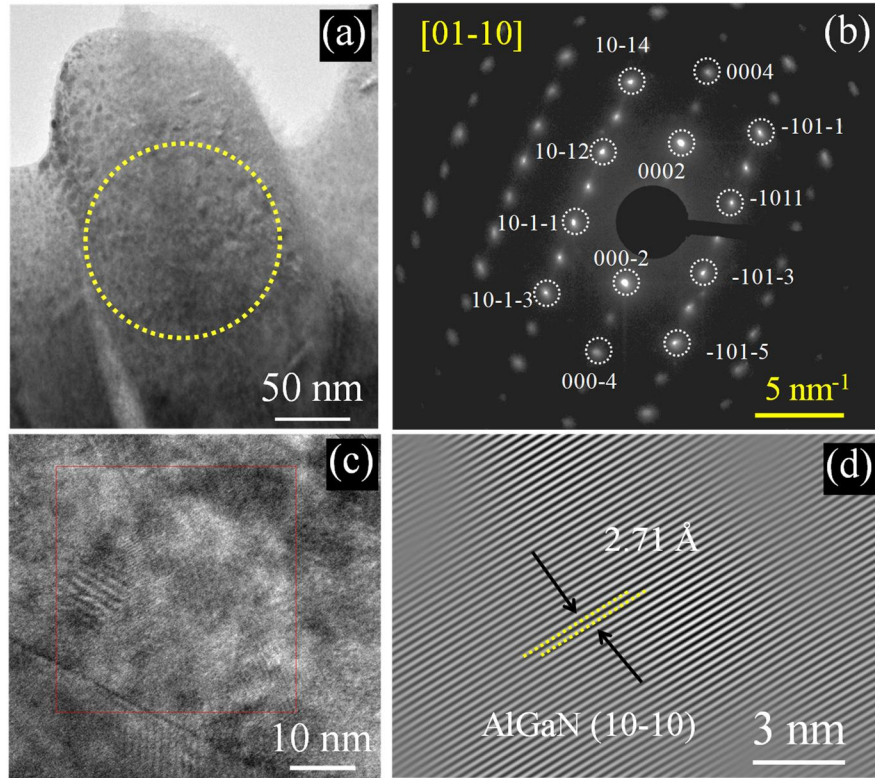
Figure 4.9. (a) The bright field TEM image of the nanorod and its encircled portion used for SAED. (b) The SAED pattern of the nanorod indexed to the wurtzite phase of AlGaN with a zone axis of [01-10]. (c) The HRTEM image of the nanorod and its marked square portion used for inverse Fourier transform. (d) The inverse Fourier transform image of nanostructure shows the (10-10) plane of AlGaN.

We performed a detailed structural analysis for further confirmation of crystalline orientation. A low magnification cross-sectional TEM micrograph is shown for a typical nanostructure (Fig. 4.9a). The selected area electron diffraction (SAED) pattern of the nanostructure (Fig. 4.9b) recorded from the encircled portion shown in the TEM image (Fig.

4.9a), is indexed to wurtzite phase of AlGaN with zone axis along [01-10]. The HRTEM image is shown for a typical nanostructure (Fig. 4.9c). The corresponding inverse Fourier transform image (Fig. 4.9d) for the selected area, marked in the figure 4.9c) shows an interplanar spacing of 2.71 Å corresponding to the m (10-10) planes of AlGaN.[10] Thus, the complete conclusions regarding the orientation of the $Al_{0.97}Ga_{0.03}N$ nanorods made out of the piezoresponse image are exactly matched with the structural analysis.

4.2.5 Piezoresponse point spectroscopy

Further to enrich our argument on the polarity of different planes, the PFM spectroscopy was carried out on both the NRs with facets along c- and m-plane in the applied voltage range of -10 to +10 V in forward and backward sweep and is depicted in figure 4.10. The topographies of NRs with facets along m- and c-plane are shown in figures 4.10a and 4.10d, respectively. In the case of both positive and negative sweep, the piezoresponse increases with increase in the magnitude of the applied voltage. In the case of the m-plane nanorod (Fig. 4.10a), both forward and reverse sweep follows the same path, without any hysteresis of the piezoresponse (Figs. 4.10b and 4.10c). However, the c-plane oriented nanorod (Fig. 4.10d) shows hysteresis towards the piezoresponse with the voltage sweep for both the cycles (Figs. 4.10e and 4.10f). In general, the total piezoresponse in a crystal is the sum of piezoresponse due to spontaneous polarization developed because of its crystal structure and induced polarization because of the applied electric field.[8,17] The absence of hysteresis in the piezoresponse versus applied voltage in case of the m-plane oriented NRs (Figs. 4.10b and 4.10c), clearly signifies that there is no spontaneous polarization in the probed direction (m-axis). Whereas, in the case of the c-plane oriented NRs (Figs. 4.10e and 4.10f) there is clear hysteresis behavior. This hysteresis signifies

that the observed piezoresponse is because of the induced polarization added up with the spontaneous polarization arising from the crystal asymmetry in case of the wurtzite crystal.[16]
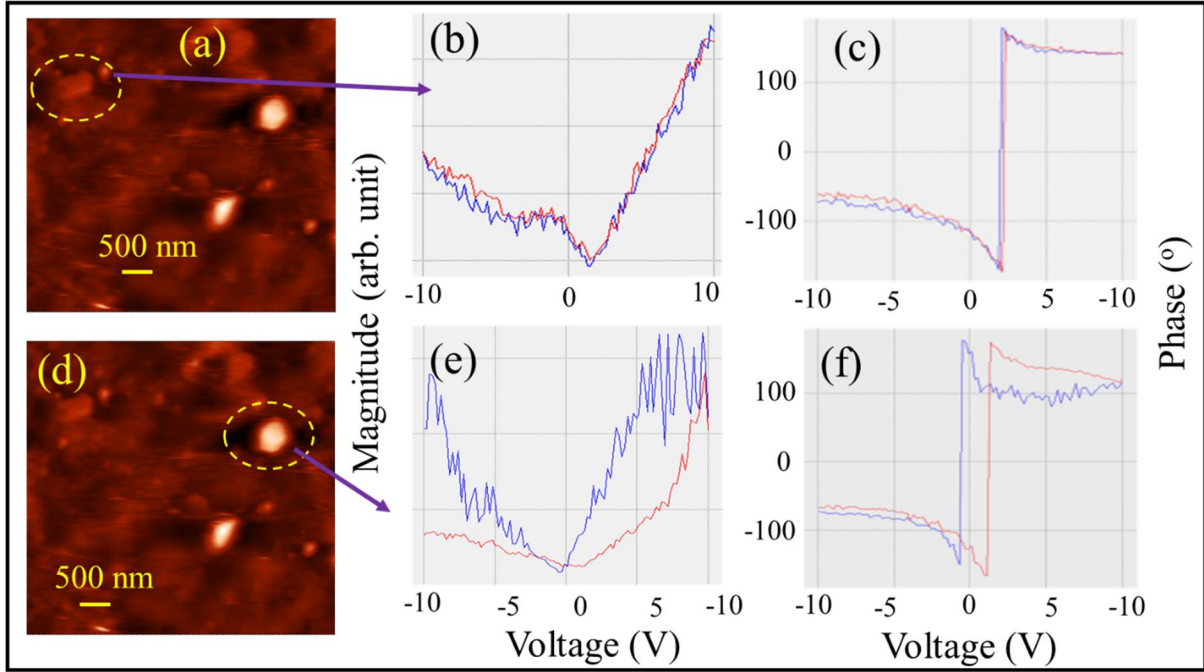
Figure 4.10. (a) The topographic image and (b) variation of magnitude and (c) phase with the applied voltage on m-plane oriented $Al_{0.97}Ga_{0.03}N$ NRs selected for point spectroscopy. (d) The topographic image and (e) variation of magnitude and (f) phase with an applied voltage on c-plane oriented $Al_{0.97}Ga_{0.03}N$ NR.

4.2.6. Calculation of piezoelectric coefficient (d_{33})

In order to quantify the observed piezoresponse, the d_{33} value was calculated using the point spectroscopy for V_{dc}=0 V. The accurate value of d_{33} can be measured with the help of a laser interferometer technique.[18,19] The interferometric technique can be employed successfully in case of bulk crystal or films. Nevertheless, this technique cannot be utilized to find the piezoelectric coefficient in nanostructures because of the constraint in the crystal size. Therefore, we have presented a maiden attempt to calculate the value of d_{33} from PFM measurements.

In a typical PFM, when a modulation voltage V is applied between the tip and the piezoelectric material, there is a vertical displacement of the tip. Since the tip is in mechanical contact with the sample, it accurately follows the piezoelectric motion of the sample surface. In the present study, the voltage applied across the nanorod of height h; generates an electric field E_3 along the c-axis, which elongates or contracts the nanorod by an amount Δh. Then the piezoelectric coefficient d_{33} is given as,[13,14]

$$d_{33} = \Delta S_3/E_3 \ldots\ldots\ldots\ldots\ldots\ldots\ldots\ldots\ldots\ldots\ldots (4.1)$$

where $E_3 = V/h$ and $\Delta S_3 = \Delta h/h$ is the change of strain along the c-axis. Putting the values of E_3 and ΔS_3 in the equation (4.1), d_{33} can be written as

$$d_{33} = \Delta h/V \ldots\ldots\ldots\ldots\ldots\ldots\ldots\ldots\ldots\ldots. (4.2)$$

Thus, the amplitude of the tip vibration measured by the lock-in technique provides information on the piezoelectric strain, and the piezoelectric coefficient, d_{33} can be determined using the equation (4.2). The average value of the d_{33} was calculated from the different NRs and was found to be 9.0 pm/V. We have listed d_{33} values in III-V nitride in its various forms measured with different techniques including the results of the present study (Table 4.1). Irrespective of measurement techniques, Table 4.1 shows that the d_{33} value obtained in the present study is generally higher as compared to the reported values for AlN and GaN either in the form of thin film or bulk.[17-20] However, a high value of piezoelectricity (~12 pm/V) was also reported for GaN NWs using PFM technique,[21] So the high value of d_{33} in $Al_{0.97}Ga_{0.03}N$ NRs, observed in the present study, is either pertaining to the nanostructure or to the PFM technique used for the measurement, as it is also observed in case of GaN NWs measured using the same technique. Nevertheless, the d_{33} values of thin film AlN and AlGaN microrods,

measured using PFM technique, are in the same range of the reported values for these materials in various forms including bulk using laser interferometer technique.[17,19,20] Thus, the PFM technique, adopted for the first time in the piezoelectricity measurement in $Al_{0.97}Ga_{0.03}N$ NRs, may not be primarily responsible for the observed increase in the d_{33} value.

Table 4.1. Comparison of the reported d_{33} value of GaN and AlN with the present study.

Material	Piezoelectric Co-efficient	Measurement Method
GaN bulk	3.7 [Ref. 20]	Laser interferometer
GaN thin film	3.1 [Ref. 18], 2.8 [Ref. 20]	
AlN bulk	5.6 [Ref. 20]	Laser interferometer
AlN thin film	4.0 [Ref. 20], 5.1 [Ref. 18]	
AlN thin film	5.1 [Ref. 19]	Laser interferometer and PFM
GaN nanowire	12.4 [Ref. 21]	PFM
AlGaN microrods	4.14 [Ref. 17]	PFM
$Al_{0.97}Ga_{0.03}N$ nanorod	**9.0 (present work)**	**PFM**

The enhanced piezoresponse in a material can be observed because of the several reasons like residual strain from the substrate,[18,19] elongated geometry of the crystallite, and reduction of crystal size in the nano regime.[21,22] Moreover, the effect of clamping also plays a vital role in determining d_{33} value. Nevertheless, in the PFM measurement, the crystal with clamping gives rise to a reduction in the estimation value as compared to the actual value.[18] In the present study, the strain may not play a significant role in the enhancement, since the one-dimensional nanorod grown on sapphire is expected to be free from the significant strain arising from the substrate.[16] Moreover, there is no significant shift in the peak position in the Raman spectroscopic analysis (Fig. 4.3) ruling out the presence strain in the sample. Therefore, the

enhancement of piezoresponse can be attributed to the size of the crystal in the nanometer scale, because of the availability of free boundary for volume expansion or contraction with the applied voltage.[21]

4.3 KPFM Study on Single GaN Nanowires

In the nanostructures, the surface states affect the band structure of the semiconductor. Therefore, the present study intends to investigate the effect of surface states on the band bending of the unintentionally doped *n*-GaN NW using Kelvin probe force microscopy with high spatial resolution.

4.3.1 Working principle and experimental details

The Kelvin probe force microscopy is a tool to measure the local contact potential difference (CPD) between a conducting AFM tip and the sample. Therefore, one can map the work function or surface potential (SP) of the sample with high spatial resolution. The CPD between the tip and sample is defined as $V_{CPD} = (\Phi_{tip} - \Phi_{sample})/e$, where Φ_{tip} and Φ_{sample} are the work functions of the tip and sample respectively, e is the electron charge.[6] In a KPFM setup, both topography and CPD maps can be obtained simultaneously by scanning the AFM tip on a sample in the single pass configuration. When an AFM tip is brought close to the sample surface, an electrical force is generated between the tip and the sample surface, due to the differences in their Fermi energy levels (Fig. 4.11).[23] This force can be nullified by applying external bias (V_{DC}) of the same magnitude of V_{CPD} with the opposite direction (Fig. 4.11). The electrical force between the probe and the sample exists in addition to the van-der-Waals force, and is given as *F= dE/dz*,
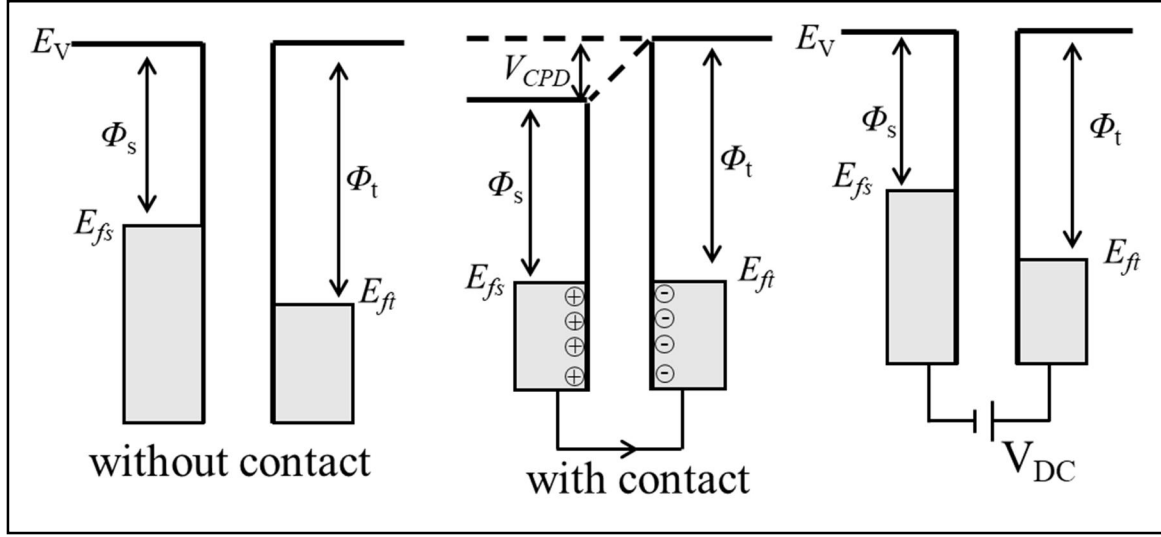
Figure 4.11. The schematic representation of the contact phenomena between the tip and the sample.

where E is the potential energy and z is the tip to the sample distance. The force due to applied DC voltage (F_{DC}) can be expressed as,[6]

$$F_{DC} = -\frac{dC(z)}{dz}\left[\frac{1}{2}\left(V_{DC} \pm V_{CPD}\right)^2\right] \dots\dots\dots\dots\dots\dots\dots\dots\dots\dots \text{(4.3)}$$

where C is the capacitance and V_{DC} applied DC voltages between the tip and the sample.

The schematic of the KPFM setup used in the present studies along with major components is shown (Fig. 4.12). The measurements were carried out at high vacuum (~10^{-7} mbar) to avoid the effect of surface adsorbents with the help of ion pump, backed with turbo molecular pump. Single-pass imaging was adopted for the simultaneous measurement of topography, and the CPD with the help of two lock-in amplifiers. The as-grown GaN NWs were mechanically transferred to an Au coated Si substrate for the KPFM measurements. Pt-Ir coated Si tip with the resonance frequency in the range of 36-98 kHz was used for the present measurements. The work function of the tip was calibrated with respect to the electron beam coated Au film prior to the measurement. Single-pass imaging was adopted for the

simultaneous measurement of topography, and the CPD with the help of two lock-in amplifiers.[24]
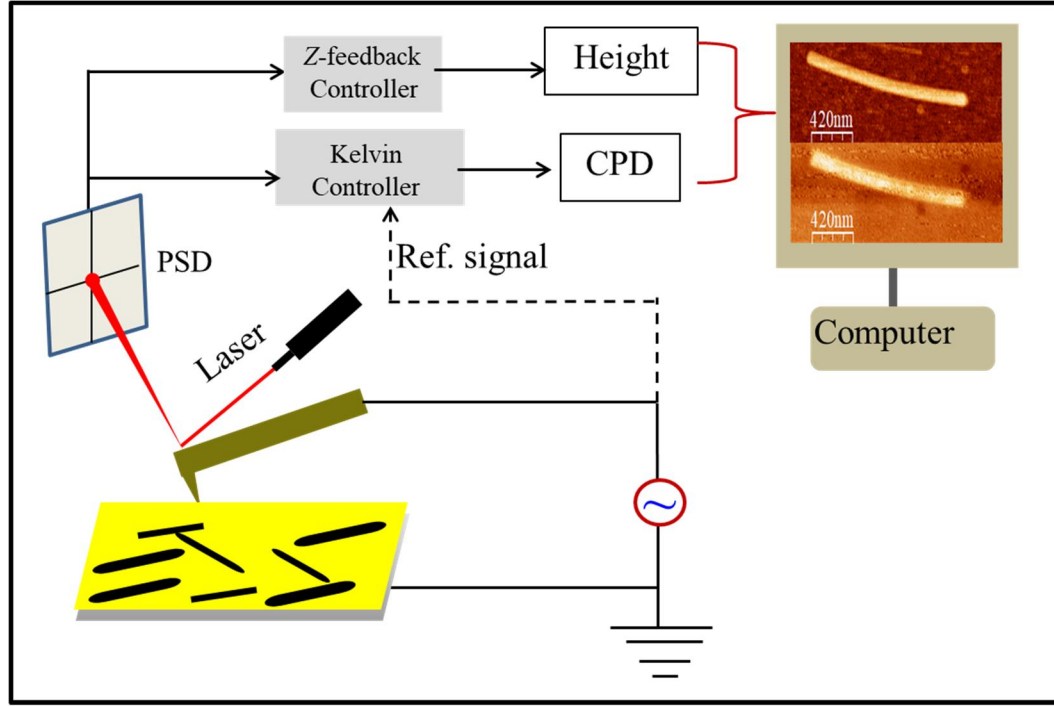
Figure 4.12. Schematic representation of the KPFM setup.

4.3.2 Size-dependent CPD and SBB in GaN NWs

The topographic and corresponding CPD map of a single GaN NW is depicted in figure 4.13. The diameter of the NW is ~80 nm (Fig. 4.13c) with a smooth and uniform surface. The corresponding line profile of the CPD map shows a difference of ~50-60 meV (Fig. 4.13d) between the tip and the NW. Several measurements were performed on NWs with different diameter, and a variation of CPD was observed. Since the NWs were taken from a single sample for the measurements, they are expected to show similar values of CPD with respect to the KPFM tip.
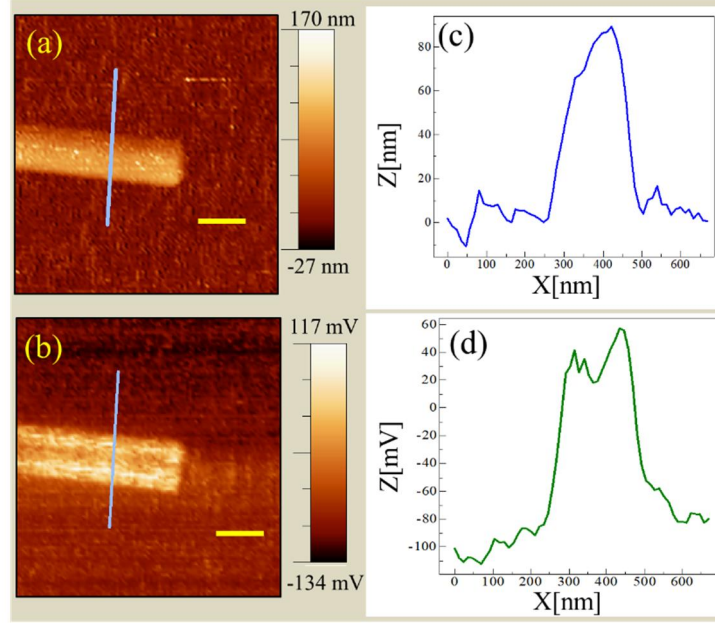
Figure 4.13. (a) Topographic and (b) CPD map of GaN NW with their corresponding (c) and (d) line profile. The scale in (a) and (b) corresponds to 220 nm.

On contrary, the measured CPD with significant variation as a function of NW size is depicted in figure 4.14. The variation of CPD can arise from the same material due to several reasons like the presence of absorbent, the difference in work function or electron affinity of the material and change in the SBB. Since the measurements were performed under UHV condition, the effect of absorbent on the measurement of CPD can be discarded. Similarly, the NWs will have equal value of electron affinity since the growth conditions are the same for all the NWs and have approximately similar carrier concentration. In the nanoscale regime, however, there may be a significant effect of surface states on the measured CPD of the NWs. As we have already discussed the effect of surface states on the SBB of the NWs (Chapter 1), which in turn modify the measured CPD value.
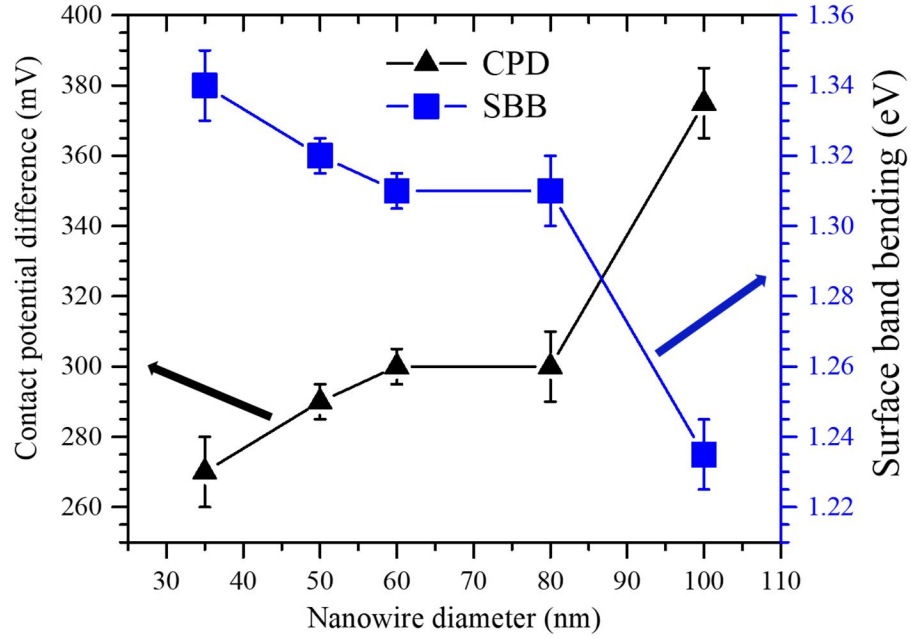
Figure 4.14. Variation of CPD and surface band bending with respect to NW diameter. Lines shown in the figure are guid to eye.

For the quantitative analysis we consider the metal (KPFM tip) and semiconductor (GaN NW) contact. When a semiconductor comes to contact with a metal, there is a SBB because of the Fermi level mismatch. The CPD between the semiconductor and the metal is the measure of band bending. In case of *n*-type semiconductor, the CPD between the metallic tip and the sample is given by,[25]

$$eV_{cpd} = \Phi_m - \chi_s - (E_c - E_f) \dots\dots\dots\dots\dots\dots\dots\dots \text{(4.4)}$$

where, Φ_m and χ_s are the work function of the metal the electron affinity of the semiconductor, respectively. E_c and E_f correspond to the conduction band minima and position of the Fermi level of the semiconductor at equilibrium, respectively. However, the CPD value gets modified in the presence of surface states at the semiconductor surface. Therefore the equation 4.4 gets

modified with an extra term, which accounts for the contribution from the band bending due to the surface states and is given by equation 4.5,[25-27]

$$eV_{cpd} = \Phi_m - \chi_s - eV_s - (E_c - E_f) \dots\dots\dots\dots\dots\dots\dots\dots\dots (4.5)$$

where V_s is the surface potential of the semiconductor which arises because of the presence of surface states. From the above relation in equation 4.5, the SBB is given by

$$SBB = eV_s = \Phi_t - \chi_s - eV_{cpd} - (E_c - E_f) \dots\dots\dots\dots\dots\dots\dots\dots\dots (4.6)$$

Using equation 4.6, corresponding SBB value of the NWs are calculated and plotted as a function of NW diameter in figure 4.14. The SBB is found to decrease with increase in the NWs diameter. In order to investigate the size dependent CPD and SBB we have performed the theoretical calculation. Electronic density of states for the surface atoms was calculated with the help of density functional theory (DFT), within the generalized gradient approximation of Perdew-Burke-Ernzerhof (PBE)[28] parametrization of the exchange-correlation potential, projector augmented-wave (PAW) method,[29,30] and a plane-wave basis set, as implemented in the Vienna Ab initio Simulation Package (VASP). [31]

As evident from Raman spectroscopic measurement, GaN NWs are in wurtzite phase. Therefore, the GaN NWs of different diameter ranging from 0.95 nm to 3.5 nm, with hexagonal cross-sectional geometry were made from supercells of optimized bulk GaN with wurtzite phase and having optimized lattice parameters. GaN NWs with [0001] growth direction and hexagonal cross-section were considered for the study. In the DFT based *ab initio* calculation, Brillouin zone is sampled by a 9×9×5 Monk-horst Pack,[32] *k*-point mesh and the energy cut-off is fixed at 520 eV for the bulk GaN. The optimized lattice parameters for bulk GaN are obtained

as a=b=3.24 Å, c=5.28 Å, which are in close agreement with experimental lattice parameter a=b=3.18 Å, c=5.16 Å, and other reported studies.[33] The band gap for bulk GaN is obtained as 1.63 eV compare to the experimental value of ~3.47 eV. This is well-known that LDA and GGA functional underestimate band gap for semiconductors.[34,35] The obtained band gap also agrees with other computationally calculated values. Nevertheless, underestimation of band gap can be overcome by using several correction schemes such as, hybrid functional,[36,37] simple interval calculation (SIC) method,[38] GW approximations.[39,40] However, these corrections are computationally expensive. Therefore, we have restricted to GGA functional for the rest of our all calculations, since, applying the correction schemes may not be computationally feasible.

GaN NWs with five different values of the diameter of the NWs are used in the study and they are of 0.95 nm with 48 atoms, 1.5 nm with 108 atoms, 2.2 nm consisting of 192 atoms, 2.8 nm with 300 and 3.5 nm with 432 atoms. A vacuum of 12 Å along X and Y-directions are used in the calculations to remove the unwanted interaction between periodic images of the NWs.

In the case of the NW with 0.95 nm diameter (Fig. 4.15a), the Ga-N bond length is 1.877 Å which is found to be reduced compared to that of the bulk value (1.99 Å). The reduction is due to the surface reconstruction of the NW in the optimized geometry, leading to a contraction of 5-6 % in the bond length. A similar contraction in the Ga-N bond length occurs for the other NWs with different diameters too. It is also found that there is no significant change in Ga-N bond length for the inner layers of the NWs (Fig. 4.15a). Hence the surface effect is confined predominantly to the outermost layer only. The contraction in bond length is found to alter the bond angle between Ga and N (Fig. 4.15a).
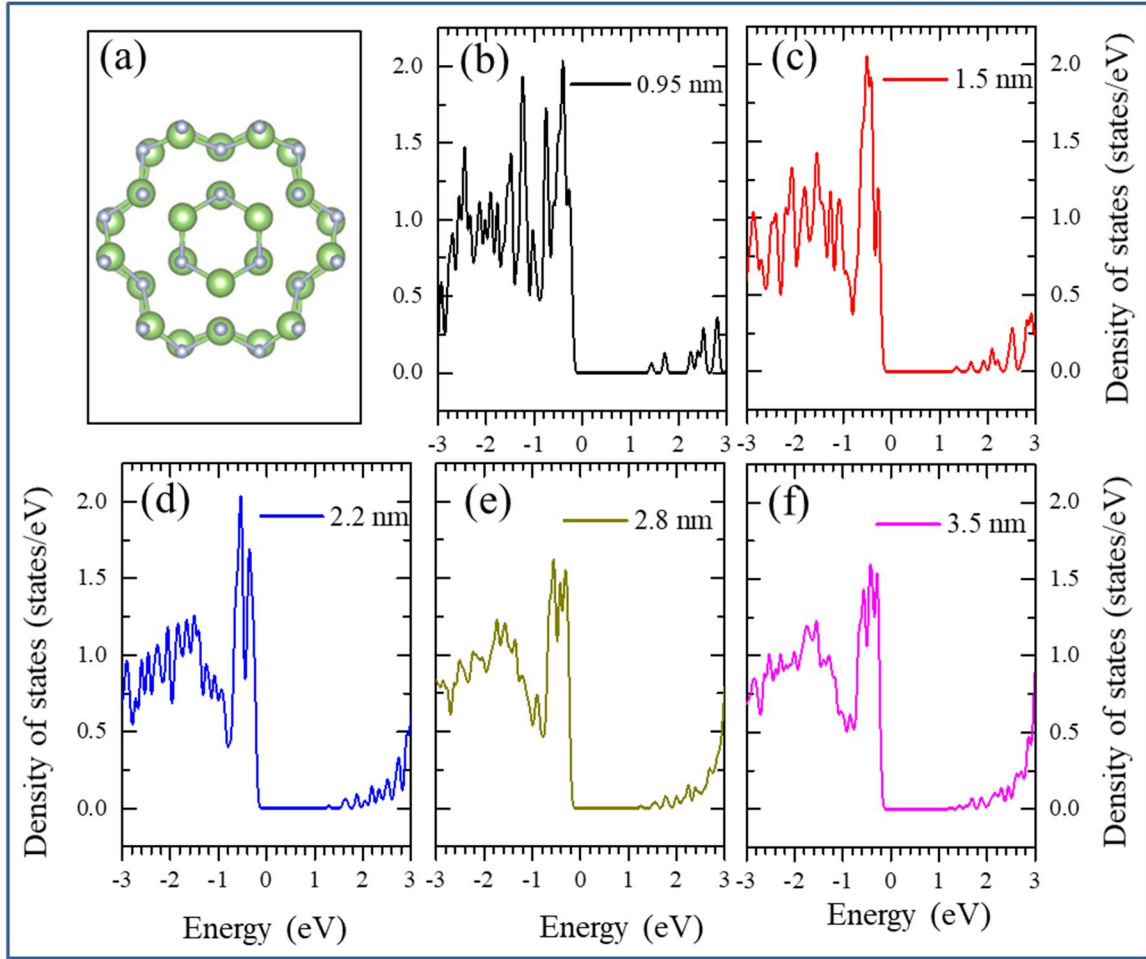
Figure 4.15 (a)The stick and ball representation of GaN NW of diameter 0.95 nm. (b)-(f) Surface density of states of GaN NW with different diameter.

The projected density of states of surface atoms of the GaN NWs with different diameters are plotted in figures 4b-f. It may be observed from the figure that the occupancy of the surface density of states increases with decrease in the diameter of the NW and the surface barrier height increases with decrease in NW diameter.

In order to inspect the variation of the surface barrier height with NW diameter, we have plotted the density of states in a narrow energy range of 1.1 to 1.5 eV (Fig. 4.16), that contains the conduction band edges of the NWs with different diameters. The conduction band

edges of the NWs with diameters of 0.95, 1.5, 2.2, 2.8, 3.5 nm are found to be at ~1.330, 1.260, 1.210, 1.175, 1.165 eV, respectively.
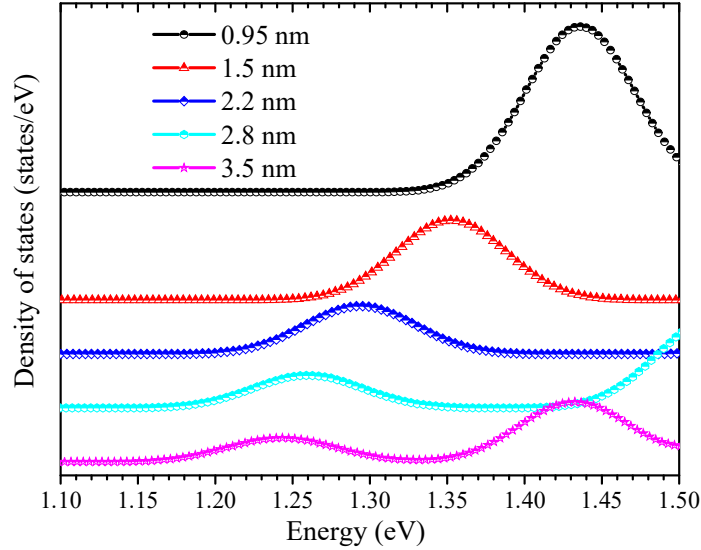
Figure 4.16. Surface density of states plotted in a narrow energy range of 1.1-1.5 eV to represent the conduction band edge of GaN NW with different diameter.

The conduction band edge shifts to higher energy (potential) with the decrease in NW diameter. Since we have fixed the E_F at 0 eV in our calculation, shift of the conduction band edge with respect to the NW diameter is because of their relative change in the E_F position for the NWs with different diameters. The SBB occurs when the NW is contacted with the metal tip in KPFM measurement and is related to the mismatch of E_F of the NW and the tip. So, when the NW is contacted by the metal tip, the value of SBB is determined from the position of the conduction band edge. As the density of states of the surface atoms are the ones those are important in this process, shift of the conduction band edge to higher energy with decreasing NW diameter indicates an increase in the SBB with decreasing NW diameter. Hence, the decrease in the CPD value with decreasing NW diameter is due to the increase in SBB arising from the increase in the surface of density of states with decreasing NW diameter.

4.4 Conclusion

In summary, the PFM imaging was carried on $Al_{0.97}Ga_{0.03}N$ NRs aligned in a different crystallographic plane. The c-plane oriented crystal showed piezoelectric deformation because of the spontaneous polarization along the crystallographic c-axis in the unit cell of the crystal. The piezoresponse confirms the polar nature of c-plane in the wurtzite crystals. Whereas, the m-plane oriented crystal does not show any piezoresponse to the applied field confirming non-polar nature and absence of spontaneous polarization along the probed direction. The c-axis oriented NRs with either group III atom (Al, Ga) or group V atom (N) terminations are also identified using PFM analysis. The piezoelectric coefficient, d_{33} was calculated to be ~ 9.0 pm/V for nanosized $Al_{0.97}Ga_{0.03}N$.

KPFM measurements are carried out on individual GaN NWs with different diameter. The contact potential difference between the KPFM tip and the GaN NW is found to be increased with the increase in the NW diameter. The corresponding SBB is calculated and found to be increasing with decrease in NW diameter. The density of states calculation with the help of DFT reveals the blue shift of conduction band edge position with decrease in NW diameter and indicate the relative variation in the E_F position. Since the density of surface states decides the position of E_F, the relative variation in the E_F is attributed to the change in electronic density of states with the NW diameter. Hence, the increase in SSB with the decrease in NW size is because of the increase in the occupancy of density of states of the surface atoms.

4.5 References

[1] R. Quay, *Gallium Nitride Electronics*, Vol. 96 (Springer Science & Business Media, 2008).

[2] C. P. Poole Jr and F. J. Owens, *Introduction to nanotechnology* (John Wiley & Sons, 2003).

[3] H. K. Wickramasinghe, Acta Materialia **48,** 347 (2000).

[4] S. V. Kalinin and A. Gruverman, *Scanning Probe Microscopy: Electrical and Electromechanical Phenomena at the Nanoscale*, Vol. 1 (Springer Science & Business Media, 2007).

[5] S. V. Kalinin and D. A. Bonnell, Physical Review B **65,** 125408 (2002).

[6] W. Melitz, J. Shen, A. C. Kummel, and S. Lee, Surface Science Reports **66,** 1 (2011).

[7] S. V. Kalinin, B. Mirman, and E. Karapetian, Physical Review B **76,** 212102 (2007).

[8] E. Soergel, Journal of Physics D: Applied Physics **44,** 464003 (2011).

[9] V. Y. Davydov, I. Goncharuk, A. Smirnov, A. Nikolaev, W. Lundin, A. Usikov, A. Klochikhin, J. Aderhold, J. Graul, and O. Semchinova, Physical Review B **65,** 125203 (2002).

[10] A. K. Sivadasan, C. Singha, K. G. Raghavendra, S. Amirthapandian, A. Bhattacharyya, A. Dasgupta, and S. Dhara, Applied Physics A **123,** 527 (2017).

[11] D. Seol, B. Kim, and Y. Kim, Current Applied Physics **17,** 661 (2017).

[12] S. V. Kalinin and D. A. Bonnell, Journal of Materials Research **17,** 936 (2002).

[13] A. Gruverman and S. V. Kalinin, Journal of Materials Science **41,** 107 (2006).

[14] B. J. Rodriguez, A. Gruverman, A. Kingon, and R. Nemanich, Journal of Crystal Growth **246,** 252 (2002).

[15] B. J. Rodriguez, A. Gruverman, A. Kingon, R. Nemanich, and O. Ambacher, Applied Physics Letters **80,** 4166 (2002).

[16] H. Morkoç, *Handbook of nitride semiconductors and devices, Materials Properties, Physics and Growth*, Vol. 1 (John Wiley & Sons, 2009).

[17] A. K. Sivadasan, G. Mangamma, S. Bera, M. Kamruddin, and S. Dhara, Journal of Applied Physics **119,** 174304 (2016).

[18] C. Lueng, H. L. Chan, C. Surya, and C. Choy, Journal of Applied Physics **88,** 5360 (2000).

[19] K. Tonisch, V. Cimalla, C. Foerster, H. Romanus, O. Ambacher, and D. Dontsov, Sensors and Actuators A: Physical **132,** 658 (2006).

[20] I. Guy, S. Muensit, and E. Goldys, Applied Physics Letters **75,** 4133 (1999).

[21] M. Minary-Jolandan, R. A. Bernal, I. Kuljanishvili, V. Parpoil, and H. D. Espinosa, Nano Letters **12,** 970 (2012).

[22] M.-H. Zhao, Z.-L. Wang, and S. X. Mao, Nano Letters **4,** 587 (2004).

[23] S. M. Sze and K. K. Ng, *Physics of semiconductor devices* (John wiley & sons, 2006).

[24] L. Collins, M. Okatan, Q. Li, I. Kravenchenko, N. Lavrik, S. Kalinin, B. Rodriguez, and S. Jesse, Nanotechnology **26,** 175707 (2015).

[25] Z. Zhang and J. T. Yates Jr, Chemical Reviews **112,** 5520 (2012).

[26] A. Cowley and S. Sze, Journal of Applied Physics **36,** 3212 (1965).

[27] S. M. Sze, *Semiconductor Devices: Physics and Technology* (John wiley & sons, 2008).

[28] J. P. Perdew, A. Ruzsinszky, G. I. Csonka, O. A. Vydrov, G. E. Scuseria, L. A. Constantin, X. Zhou, and K. Burke, Physical Review Letters **100,** 136406 (2008).

[29] G. Kresse, and D. Joubert, Physical Review B **59,** 1758 (1999).

[30] P. E. Blöchl, Physical Review B **50,** 17953 (1994).

[31] G. Kresse, and J. Furthmüller Physical Review B **54,** 1169 (1996).

[32] H. J. Monkhorst and J. D. Pack, Physical Review B **13,** 5188 (1976).

[33] D. J. Carter, M. Fuchs, and C. Stampfl, Journal of Physics: Condensed Matter **24,** 255801 (2012).

[34] J. P. Perdew and M. J. Levy, Physical Review Letters **51,** 1884 (1983).

[35] L. Sham and M. J. Schlüter, Physical Review Letters **51,** 1888 (1983).

[36] J. Heyd, G. E. Scuseria, and M. Ernzerhof, The Journal of Chemical Physics **118,** 8207 (2003).

[37] J. Heyd and G. E. Scuseria, The Journal of Chemical Physics **121,** 1187 (2004).

[38] J. P. Perdew and A. Zunger, Physical Review B **23,** 5048 (1981).

[39] M. S. Hybertsen and S. G. Louie, Physical Review B **34,** 5390 (1986).

[40] M. Shishkin and G. Kresse, Physical Review B **75,** 235102 (2007).

CHAPTER 5

LOCALIZED STUDY: NANO-SPECTROSCOPY AND NANOSCOPY OF III-V NITRIDE NANOSTRUCTURES

5.1 Introduction

In material science characterization techniques such as infrared (IR), and Raman spectroscopy provide chemical information of the materials.[1] However, the techniques lack in providing the spatial resolution for nanoscale characterization because of well-known phenomena of Abbe's diffraction limit. According to Abbe's criterion, the achievable spatial resolution in optical spectroscopy or microscopy is given as,[2,3]

$$\Delta x = 0.61\lambda/NA$$

where λ is the wavelength of the probing laser and NA is the numerical aperture of the optical system. For the best practical conditions, the experimental value of Δx turns out to be about half of the wavelength. Therefore, the spectroscopic techniques provide information of ensemble-averaged. However, scanning probe microscopy (SPM) techniques, such as scanning tunneling microscopy (STM) or atomic force microscopy (AFM), have a high spatial resolution down to the nanometer, but lack the chemical specificity for uniquely investigating the chemical information. In contrast, tip-enhanced Raman spectroscopy (TERS) has emerged as a powerful technique capable of performing such characterization as it combines the intrinsic spatial resolution of scanning probe techniques with the chemical information collected from the vibrational spectroscopy.[4,5] A metal coated tip or metal nanoparticle attached to the AFM tip allows for the nanoscale investigation because of an enhanced electromagnetic field and high spatial resolution.[5]

In the regime of visible to mid-infrared of the electromagnetic spectra, light covers the energies corresponding to the electronic transitions in atoms and molecular vibrations. Therefore, by using optical microscopes one can get information related to the intrinsic properties of the materials. Nevertheless, the resolution attainable with an optical microscope is restricted by the diffraction limit of light. The diffraction limit can be overcome by using the plasmonic metal overlayered dielectric aperture of subwavelength size. Evanescent field is produced in the nearfield of the subwavelength aperture and decreases exponentially with the aperture size. Therefore, the object has to be kept in the near-field of the aperture and can be easily achieved by employing the AFM.[2,6] In near-field optical microscopy (NSOM), the spatial resolution is dependent on the size of aperture rather than the wavelength of the illuminated light.

The present Chapter describes the nanoscopic and nano-spectroscopic imaging of single GaN NWs in the sub-diffraction limit. The spectroscopic investigation on a single GaN NW are carried out with the help of plasmonic (Au nanoparticle) assisted TERS. Similarly, the nanoscopic optical imaging of a single GaN NW is achieved with the help of plasmonic (Au thin film) assisted NSOM technique in the sub-diffraction limit.

5.2 Tip Enhanced Raman Spectroscopy

5.2.1 Principle and experimental details

Raman scattering cross section is very low because of the inelastic scattering, which prevents one to get sufficient scattering photon intensity from nanostructure. This problem is easily tackled by employing a TERS tip, which enhances the electric field in the sub-nanometer regime of the sample and can probe the properties of the nanostructure. The SPM tip coated

with noble (Au, Ag) metal film enhances the electric field locally around the tip apex and can improve the spatial resolution down to 10 nm.[3] The schematic representation of the process is depicted in figure 5.1.
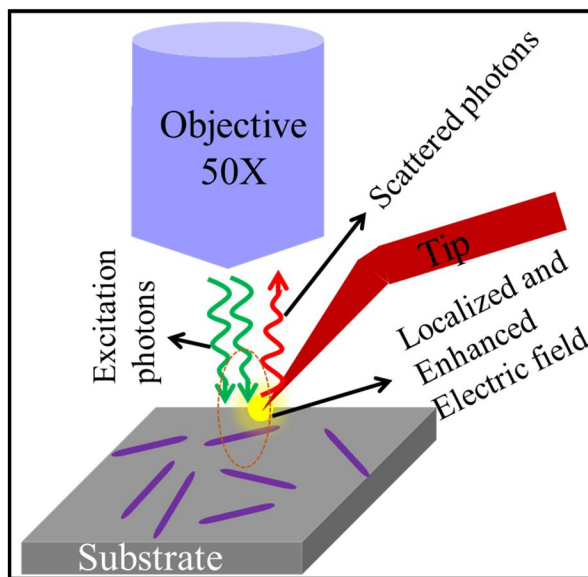
Figure 5.1. Schematic representation of TERS process.

The enhancement factor for TERS is mostly controlled by the shape and size of the tip apex. Moreover, the tip-sample distance decides the enhancement of the Raman signal.[3] The gap between the tip and the sample must be controlled accurately with a piezo scanner and feedback mechanism. The ability to move the sample and the tip with independent piezoelectric elements enables the precise positioning of the laser beam with respect to the tip apex and the raster scanning of the sample for imaging. The SPM setup coupled with a Raman spectrometer and laser light can be used to perform the TERS measurements.

In the present Thesis, TERS measurements were carried out using the SPM setup (Nanonics, MultiView 4000; Multiprobe imaging system) coupled with a laser Raman spectrometer (inVia, Renishaw) in the backscattering configuration. For the TERS study, the

as-grown NWs were detached from the substrate and dispersed on single crystal Al (001) substrate to get monodispersed NWs. The tip is AFM bent glass probe attached with Au particle (< 100 nm) and operated under normal force feedback. The Raman signals are collected by exiting the samples with 514.5 nm laser using 50X objective with NA of 0.42. The simultaneous topographic and TERS images of a single NW were recorded by scanning the NW in the near-field, with a 256×256 pixel size and high spatial resolution in the sub-wavelength regime. The spectral maps were created by integrating the peak intensity of a particular Raman mode collected over all pixels of the image. The Raman spectra were collected for several single NWs. However, the NW with diameter ~225 nm could give measurable Raman signal and was considered for further measurements.

5.2.2 Spectroscopic analysis

The Raman spectra are collected for the selected single NW (diameter ~225 nm as shown later from the AFM image) in the presence (with) and absence (without) of the TERS tip. In the Raman spectra (Fig. 5.2), the prominent peaks ~568 and 560 cm^{-1} correspond to E_2(high) and E_1(TO) phonon modes, respectively.[7,8] In the presence of TERS tip, the overall strength of the Raman spectra is increased. In the presence of TERS tip, the incident light can be three-dimensionally confined to the vicinity of the metallic nanoparticle and is utilized for the enhancement of the Raman scattering efficiency in the near-field region.[3,9] Therefore, we could get prominent Raman modes in the presence of TERS tip as compared to the that of the far-field measurement.
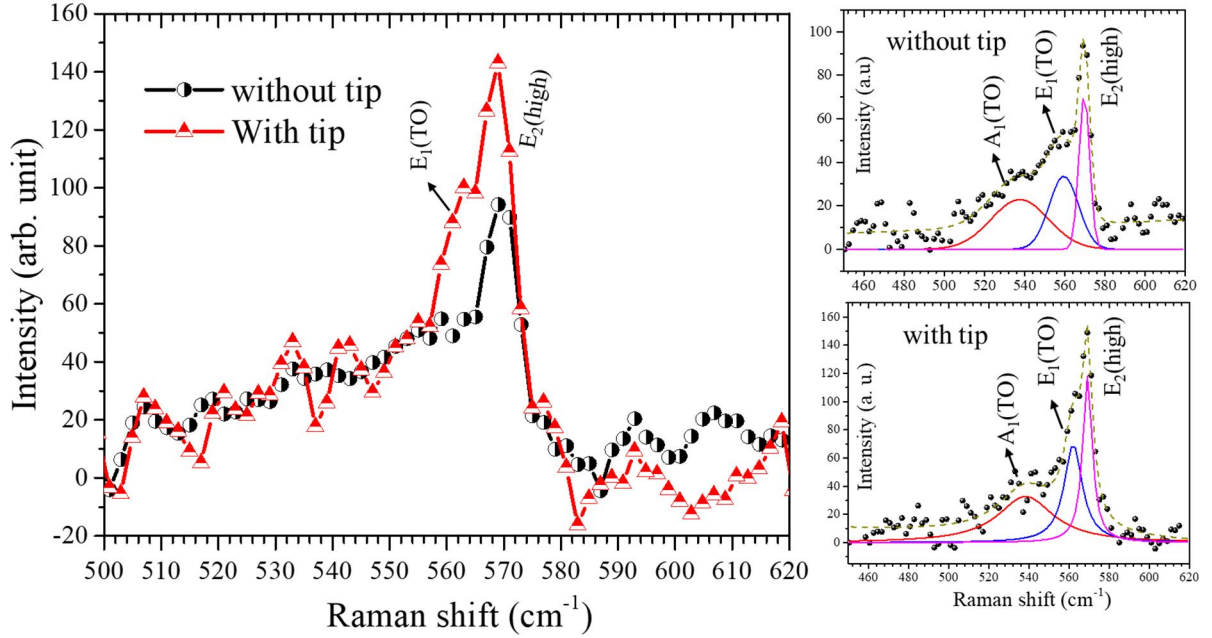
Figure 5.2. Raman spectrum of a single NW with and without tip. Outsets showing deconvoluted Raman spectra collected at a single scan area on the GaN NW without and with the assistance of TERS tip.

The enhancement in the Raman signal for the E_1(TO) mode appears to be higher as compared to E_2(high) mode (Fig. 5.2). To investigate it further, the Raman spectra collected in the presence and absence of TERS tip at a single scan area on the NW were deconvoluted as shown in the outsets. After the deconvolution of the Raman spectra a broad peak ~540 cm^{-1} was observed in both the cases and is assigned to the A_1(TO) vibrational mode.[7,8] Further the intensity ratio of all the three modes of A_1(TO), E_1(TO) and E_2(high) were calculated with the presence and absence of the TERS tip and was found to be 1.43, 2.08 and 1.65, respectively.

5.2.3 Tip enhanced Raman spectroscopic imaging

With the enhanced Raman signal, we have spectroscopically imaged a single GaN in the sub-diffraction limit. The spectroscopic imaging of a single NW was performed by considering the peak intensity of E_2(high) mode along with the corresponding topographic information (Fig. 5.3a).
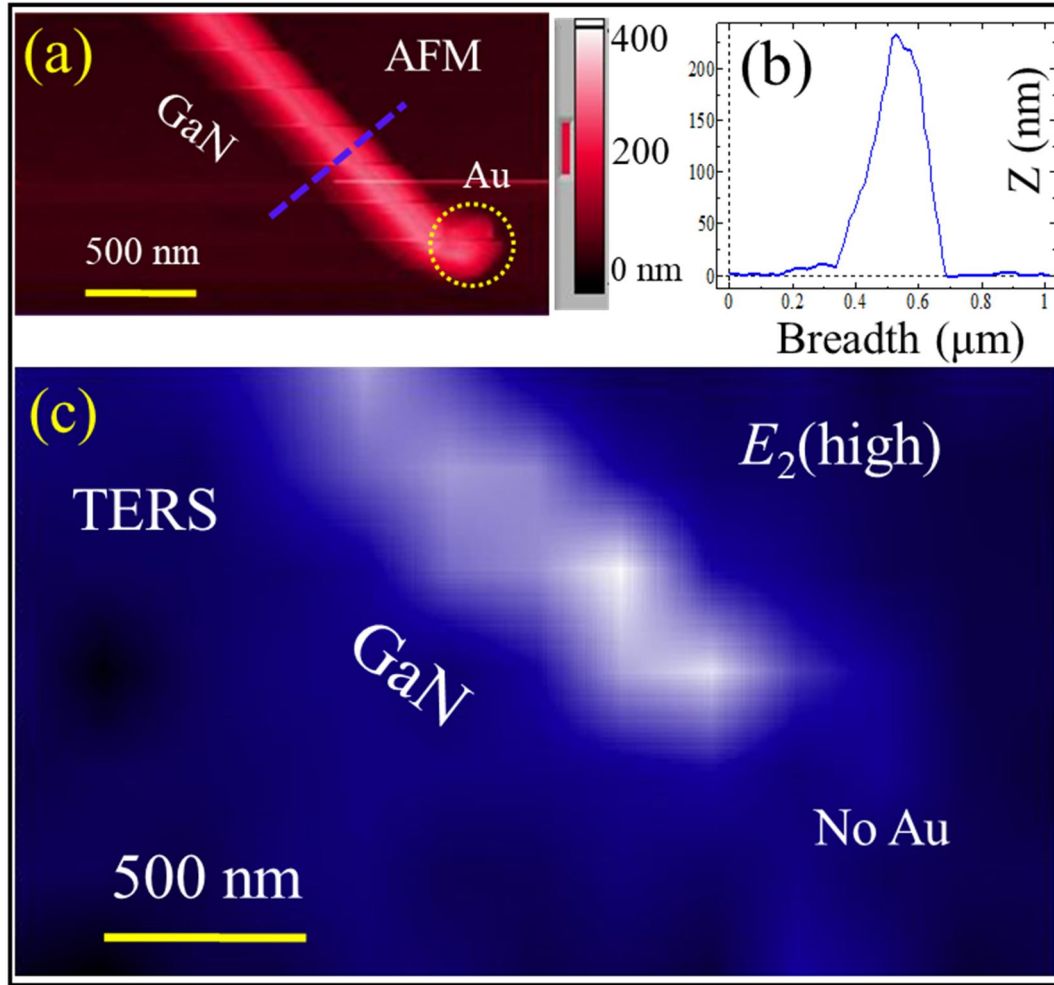
Figure 5.3. (a) AFM image of a single GaN NW with the corresponding (b) line profile and (c) TERS image.

The diameter of the NW was measured as 225 nm as shown in the line profile of the height map of the AFM image (Fig. 5.3b). Since the NWs are grown via Au catalyst assisted VLS process,[10] the AFM image (Fig. 5.3a) of the NW contains the Au nanoparticle at the tip of the NW. Whereas, in the case of the TERS imaging (Fig. 5.3c), the figure represents the intensity distribution of E_2(high) phonon mode of GaN along the NW. Therefore, the portion corresponding to the AFM image of Au NP (Fig. 5.3a) is missing in the TERS image (Fig. 5.3c). In the present configuration, the spatial resolution is restricted up to 750 nm using 514.5 nm excitation objective of 0.42 NA. However, with the help of TERS, we could study the

spectroscopic property of a single NW with a size (~225 nm) far below the diffraction limit. In this regard, it may be noted that in one of our earlier studies, TERS imaging was not possible for AlN nanotip of diameter ranging from 70-250 nm.[11] The higher value of fractional ionic character; (FIC) value 0.72 in AlN than that compared to 0.51 for GaN might be the reason for which it was difficult for the TERS imaging of the former in the sub-diffraction limit.[12] The magnitude of the change of the polarizability, which matters in enhancing the Raman scattering efficiency, decreases with increasing FIC value and it is higher by 50% for AlN with respect to that for the GaN.

5.2.4 Enhancement factor

Further to examine the influence of nearfield spectroscopy on the Raman modes, we have calculated the enhancement factor corresponding to each vibrational mode. The enhancement factor in TERS is given by the relation,[11,13,14]

$$EF = (\frac{I_{NF}}{I_{FF}} - 1)\frac{V_{FF}}{V_{NF}} \dots\dots\dots\dots\dots\dots\dots\dots\dots\dots\dots\dots\dots (5.1)$$

where I_{NF} and I_{FF} are the Raman peak intensities recorded with the presence and absence of TERS tip in the near- and far-field respectively. V_{FF} is the interaction volume of the far-field laser probe, and V_{NF} is the effective interaction volume of near-field TERS probe with the sample. A cylindrical interaction volume was considered and is given as $V = \pi(d/2)^2 \times \delta$, where d is the diameter of the NW and δ is the depth of penetration of the laser. The enhancement factor for E_1(TO), E_2(high), and A_1(TO) modes are found to be around 31, 20 and 13, respectively. A Nominally improved enhancement factor was found for E_1(TO) modes. In the present case, the c-axis oriented wurtzite GaN NW is laying on the substrate (*XY*-plane), and the bent TERS tip makes an angle (60º) with the sample. In the backscattering configuration,

A_1(TO) and E_1(TO) modes are excited by X polarized light and are expected to be selectively enhanced under the influence of the localized electric field (parallel to the sample surface, XY-plane) in the presence of a tip parallel to Z-axis.[15] However, in the present configuration, the tip axis is not exactly parallel to the Z-axis. Therefore, we could see the similar enhancement of all the Raman modes, instead of the selective enhancement of a particular mode. In order to understand the distribution of localized electric field in the coupled system of GaN NW and the TERS tip, the finite-difference time-domain (FDTD) simulation was carried out.

5.2.5 Finite-difference time-domain simulation

In order to study the localized field enhancement due to the TERS tip on GaN NW the near-field electrical field intensity maps were simulated and extracted using commercial FDTD numerical simulation (Lumerical FDTD Solutions, Canada). A X polarized light was used for the excitation of the coupled Au tip and GaN NW system. The NW was kept along X-direction in the XY-plane with the tip in the XZ-plane with a bent angle of 60°. Further, the tip was positioned 10 nm above the sample surface to simulate the approximate gap expected during a typical scan. The schematic of the simulated structures projected in XZ-plane is shown in figure 5.4a. The simulation time was tuned to 1000 fs to allow the energy field to decay completely. During all the numerical simulations, the mesh size was kept as $3 \times 3 \times 2$ nm. We consider the near-field distribution of electric field at the tip and NW interface only where the projected electric field distributions are shown for XY- (Fig. 5.4b) and XZ- (Fig. 5.4c) planes. The strength of electric field distribution seems to be equivalent in both the planes at the tip and NW interface and hence, the EFs for the phonon modes are observed in the same order.
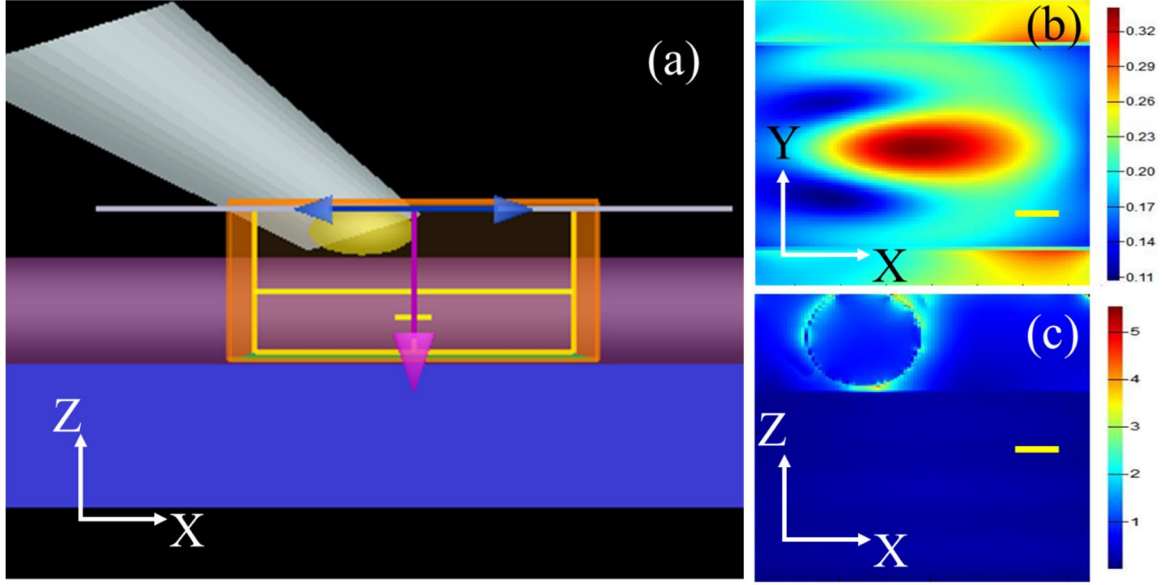
Figure 5.4. (a) The schematic view of the simulated structure along with *XZ*-plane. The near-field electric field intensity distribution images in (b) *XY*- and (c) *XZ*-planes. Scale bars in (b) and (c) are 40 nm. The color bars indicate the relative strength of the field.

5.3 Near-field Scanning Optical Imaging of Single GaN Nanowire

5.3.1 Experimental details

NSOM is an SPM based microscopic technique that exceeds the classical diffraction limit of the light to attain a spatial resolution significantly below the diffraction limit. The detailed schematic of the experimental set up used for the present study is shown in figure 5.5. In the present study, NSOM imaging was carried out using the aperture probe in the reflection mode with 532 nm laser excitation. An Au/Cr metal overlayered aperture tip (~150 nm) was used in the near-field. The light from the laser source and aperture probe were coupled through an optical fiber. The tip-sample distance was controlled using normal force feedback mechanism with the help of a tuning fork of high Q value. The scattered light was collected with confocal detection using 50X objective lens of the NA ~0.42. The collected light was directed towards the avalanche photodiode (APD) single photon counter. The scanning was carried in

intermittent (tapping) mode with the raster scanning. The simultaneous topographic image was also acquired along with the intensity mapping of scattered photon detection.
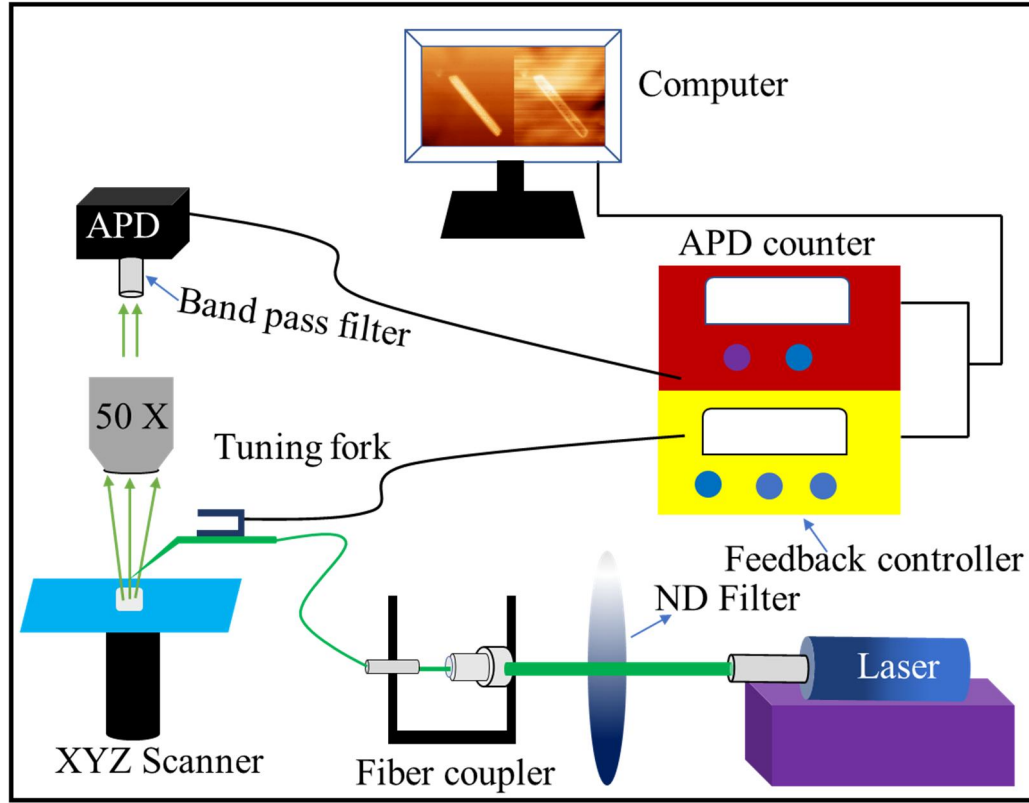
Figure 5.5. Schematic representation of the set up for NSOM study

5.3.2 Nanoscopic imaging
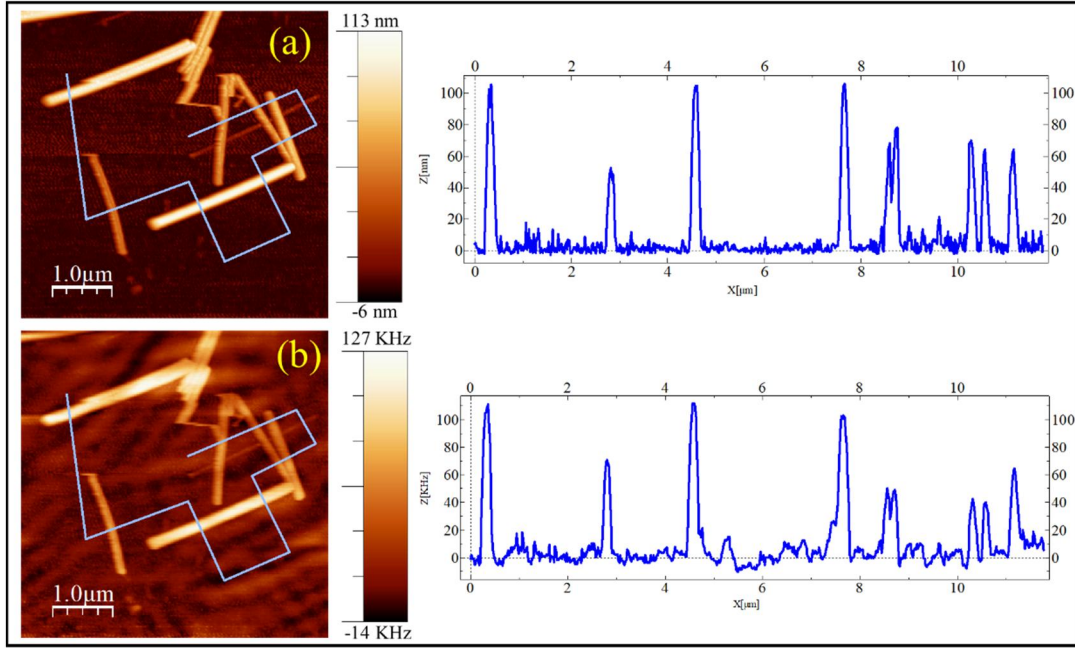
The nanoscopic near-field optical imaging of GaN NWs is carried out with the simultaneous AFM imaging. The AFM image with the corresponding NSOM image is depicted in figure 5.6. The topographic AFM image shows NWs of smooth and cylindrical shape, with a diameter varying ~10-60 nm (Fig. 5.6a). As one can see there is one to one correspondence between the AFM and NSOM image (Fig. 5.6b).
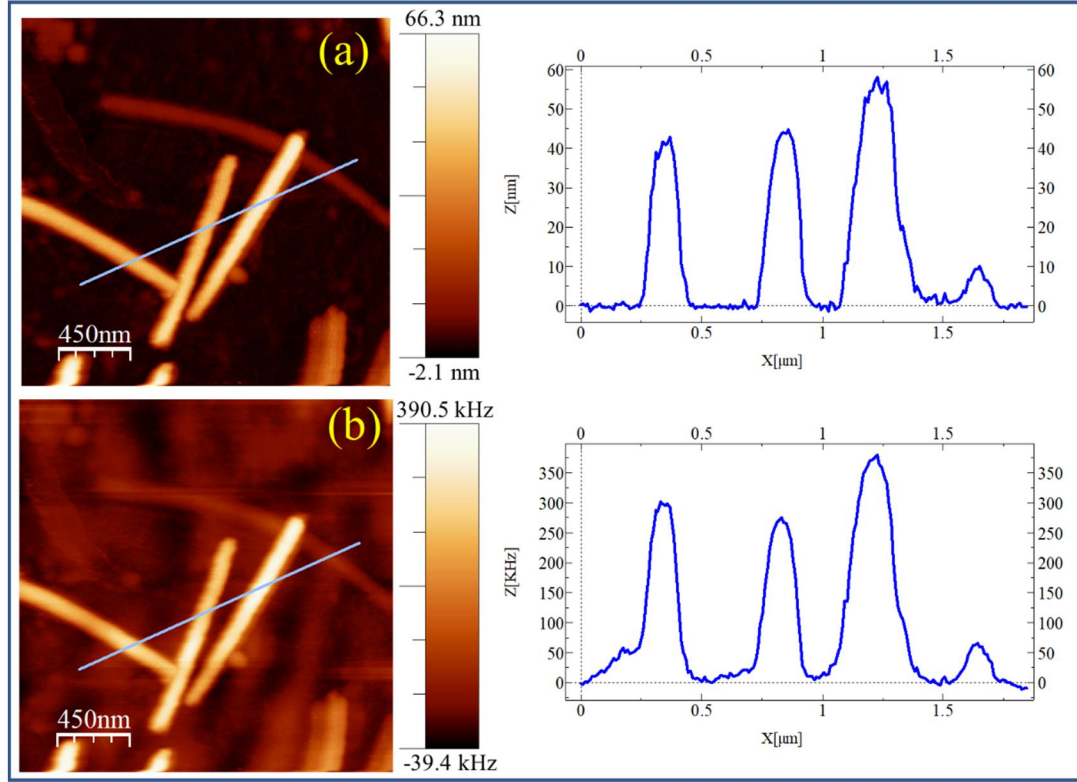
Figure. 5.6. (a) Topographic and (b) NSOM image of GaN NW with their corresponding line profile at the outsets.

All the NWs are clearly resolved by both AFM and NSOM imaging with an aperture probe of ~150 nm. The NWs imaged in the present study are far below the diffraction limit for the excitation wavelength (532 nm). Here we intend to mention that even the smallest GaN NW (~10 nm) is also well resolved in the optical image, for the first-time. Several measurements are carried for the NWs of different size. A typical NSOM image of NWs (~20-100 nm) with the corresponding topographic image is also depicted in figure 5.7. In order to achieve such highly resolved optical images (Figs. 5.6 and 5.7) one needs to shorten the wavelength of probing light down to the sub-diffraction regime.[2,16] This can be achieved by using metal coated NSOM probe,[17] which produce an evanescent wave of momentum higher than that of the original excitation wavelength.[2] The evanescent waves originating from the NSOM probe aperture possess a group of wave vectors higher than the original excitation laser with different

velocities (*v*), which is slower than the excitation wave velocity. Moreover, it preserves the frequency of the excitation wave. Hence, one can achieve super-resolution as well as spectroscopic information from the nanostructure bellow the sub-diffraction limit.

Figure. 5.7. (a) Topographic and (b) NSOM image of GaN NW with their corresponding line profile at the outsets.

5.4 Conclusion

With the help of tip enhanced Raman spectroscopy (TERS) and nanoscopic near-field scanning optical microscopy (NSOM), we could study the properties of GaN NWs far below the diffraction limit of light. Spectroscopic image of a single GaN NW with diameter ~225 nm is recorded, for the first time, using TERS measurements. The TERS study shows similar enhancement factors for observed Raman modes and is attributed to comparable electric field distribution at the tip and NW interface, as shown by finite-difference time-dependent (FDTD) calculations. In a nanoscopic measurement, GaN NWs of diameter ~ few 10s of nm were imaged with excellent clarity, for the first time, using NSOM measurements.

5.5 References

1   J. R. Ferraro, *Introductory Raman spectroscopy* (Elsevier, 2003).

2   S. Kawata, Y. Inouye, and P. Verma, Nature Photonics **3,** 388 (2009).

3   P. Verma, Chemical Reviews **117,** 6447 (2017).

4   M. Lucas and E. Riedo, Review of Scientific Instruments **83,** 061101 (2012).

5   P. Verma, T. Ichimura, T. A. Yano, Y. Saito, and S. Kawata, Laser & Photonics Reviews **4,** 548 (2010).

6   L. Novotny and B. Hecht, *Principles of Nano-optics* (Cambridge university press, 2012).

7   H. Harima, Journal of Physics: Condensed Matter **14,** R967 (2002).

8   S. Parida, A. Patsha, S. Bera, and S. Dhara, Journal of Physics D: Applied Physics **50,** 275103 (2017).

9   Z. Zhang, S. Sheng, R. Wang, and M. Sun, Analytical Chemistry **88**, 9328 (2016).

10   A. Patsha, S. Amirthapandian, R. Pandian, and S. Dhara, Journal of Materials Chemistry C **1,** 8086 (2013).

11   A. K. Sivadasan, A. Patsha, A. Maity, T. K. Chini, and S. Dhara, The Journal of Physical Chemistry C **121,** 26967 (2017).

12   S. J. Pearton, *GaN and Related Materials II*, Vol. 7 (CRC Press, 2000).

13   B. Pettinger, P. Schambach, C. J. Villagomez, and N. Scott, Annual Review of Physical Chemistry **63**, 379 (2012)

14   N. Kumar, A. Rae, and D. Roy, Applied Physics Letters **104,** 123106 (2014).

15   R. Matsui, P. Verma, T. Ichimura, Y. Inouye, and S. Kawata, Applied Physics Letters **90,** 061906 (2007).

16   J. A. Schuller, E. S. Barnard, W. Cai, Y. C. Jun, J. S. White, and M. L. Brongersma, Nature Materials **9,** 193 (2010).

17   W. L. Barnes, A. Dereux, and T. W. Ebbesen, Nature **424,** 824 (2003).

CHAPTER 6

SUMMARY AND FUTURE SCOPE

The Thesis primarily described the localized optical and electrical properties of III-V nitride nanostructures. In the beginning, the growth of GaN nanowires (NWs) using the atmospheric pressure chemical vapor deposition (APCVD) and AlGaN NWs by ion beam techniques were discussed. Presence of native defects in GaN NWs and their effect on electron-phonon couplings was investigated. Subsequently, the role of native defects in the gas sensing behavior of AlGaN NWs was also explored. In the localized measurements, the properties at the nanoscale were studied with the help of scanning probe microscopy (SPM) based techniques along with the light coupled system. The summary of individual chapters is discussed below.

6.1 Summary of the Thesis

In Chapter 1, the physical properties of III-V nitrides are discussed briefly. Role of native defects on vibrational, luminescence and gas sensing properties of III-V nitride nanostructures are described in detail. Further, the advantages of ion beam technique in the alloy formation and its utilization for the synthesis of AlGaN NWs is detailed. The importance and utilization of SPM based techniques as localized probe for studying the electrical and optical properties at the nanoscale are described as the prime focus of the present Thesis.

The major findings of the present Thesis are briefed as follows

Chapter-2

1. Different Ga/N ratios were achieved in GaN NWs by changing partial pressure of NH_3 in the APCVD technique.

2. Sample grown under N rich condition was found to be close to the stoichiometry.

3. The influence of native defect induced carriers on Raman spectra were confirmed from the observed blue shift of A_1(LO) mode with decreasing Ga/N ratio.

4. The carrier concentration and mobility of the GaN NWs were calculated from the line shape analysis of the plasmon coupled phonon mode of A_1(LO). The sample with least value of Ga/N ratio showed the highest carrier concentration of 6.8×10^{17} cm^{-3} and the lowest carrier mobility of 57 cm^2.V^{-1}. s^{-1}.

5. Strong electron-phonon coupling was revealed with the observation of phonon replica in the photoluminescence spectra of samples grown under N reduced conditions.

Chapter-3

1. AlGaN NWs were synthesized by the ion beam techniques of ion beam mixing (IBM) and post irradiation diffusion (PID) processes, for the first time.

2. Vibrational studies with the help of Raman spectroscopy revealed the one-mode phonon behavior corresponding to the A_1(LO) phonon mode in the random alloy of AlGaN.

3. The Al incorporation percentage was estimated from the Raman spectroscopic analysis and was found to increase with irradiation fluence and post irradiation annealing temperature in both the processes of IBM and PID.

4. The highest Al atomic percentage of ~6.3%–6.7% was achieved in AlGaN at a fluence of 5E16 ions·cm^{-2} with the post irradiation annealing of 1000 °C.

5. Methane (CH$_4$) sensing at a low operating temperature (50 °C) was realized for the AlGaN NWs for the first time.

6. The gas sensing efficiency in AlGaN NWs was significantly influenced by the presence of the native defects. The sensing mechanism was described with the insight from the detailed defect analysis by PL spectroscopy.

7. An increase in sensing response by ~5 times was recorded for AlGaN NWs as compared to that for the as-grown GaN NWs.

Chapter-4

1. The piezo force microscopy (PFM) imaging was carried on epitaxially grown $Al_{0.97}Ga_{0.03}N$ nanorods (NRs) aligned in different crystallographic plane.

2. The c-plane oriented NRs showed piezoresponse because of the spontaneous polarization along the crystallographic c-axis confirming the polar nature.

3. The absence of piezoresponse in the m-plane oriented NRs confirmed the non-polar nature of m-plane.

4. The piezoelectric coefficient, d_{33} was calculated to be ~9.0±1 pm/V for nanosize $Al_{0.97}Ga_{0.03}N$.

5. The surface band bending (SBB) was calculated from the measurement of the contact potential difference between the Kelvin probe force microscope (KPFM) tip and the GaN NWs and was found to increase with decrease in the NW diameter.

6. The size dependence of SBB was attributed to the increase in the density of states of the surface atoms, as supported by the density functional theory calculation.

Chapter-5

1. Spectroscopic image of a single GaN NW with diameter ~225 nm was recorded, for the first time, using tip enhanced Raman spectroscopic (TERS) measurements.

2. In nanoscopic measurements, GaN NWs of diameter ~ few 10s of nm were imaged with excellent clarity, for the first time, using near-field scanning optical microscopic (NSOM) measurements.

6.2 Future Scope

1. Synthesis of InGaN NWs by ion beam technique with the proper choice of irradiation ion and energy.

2. Fabrication of single III-nitride NW device using focused ion beam (FIB) metallization and gate formation.

    (i) Study the photo response in the single NW.

    (ii) Study the gas sensing response of the single NW device.

3. Conductance mapping in single NW with the help of conductive SPM technique.

4. High vacuum TERS measurement for further improvement of enhancement factor and spatial resolution.